

University of Alberta

Comparative Analysis, Modeling and Simulation of
Nanocrystal Synthesis by Physical Vapor Deposition
Methods

By

Abuhanif K. Bhuiyan

A thesis submitted to the Faculty of Graduate Studies and Research in partial
fulfillment of the requirements for the degree of

Doctor of Philosophy

Specialization: Micro-Electro-Mechanical Systems (MEMS) and Nanosystems

Department of Electrical and Computer Engineering

©Abuhanif K. Bhuiyan

Fall 2011

Edmonton, Alberta

Permission is hereby granted to the University of Alberta Libraries to reproduce single copies of this thesis and to lend or sell such copies for private, scholarly or scientific research purposes only. Where the thesis converted to, or otherwise made available in digital form, the University of Alberta will advise potential users of the thesis of these terms.

The author reserves all other publication and other rights in association with the copyright in the thesis and, except as herein before provided, neither the thesis nor any substantial portion thereof may be printed or otherwise reproduced in any material form whatsoever without the author's prior written permission.

Abstract

Nanotechnology is rapidly becoming one of the most influential frontiers of technology. Nanocrystal (NC) synthesis is potentially one of the central processes in nanoelectronics due to its ability to improve performance of electronics devices. Physical vapor deposition (PVD) is one of the most flexible techniques to fabricate self-assembled arrangements of nanoclusters. Controllable fabrication of such assemblies can improve reliability of nanocapacitors, enhance performance of magnetic memories, and has many applications in optoelectronics devices, etc. However, size, shape and density of NC's are highly sensitive to the process conditions such as time, rate, temperature, substrate material, etc. To efficiently synthesize nanocrystalline arrays by PVD, the process control factors should be understood in greater detail. A systematic functional modeling tool for simulating NC synthesis will have significant value in industry as well as in academia. In this work, I compare different modeling techniques and present lattice based and off-lattice Kinetic Monte Carlo (KMC) simulation models of both 2d and 3D structures. I developed the models and report simulations that explicitly represent the PVD synthesis of NCs on substrates. I also studied how by varying the parameters a process engineer can have control on the self assembled synthesis of NCs. The results are compared with experimentally observed surface morphologies generated by PVD and demonstrate that KMC models like this are an efficient tool for computer-aided design of PVD processes for synthesis of NCs.

Acknowledgements

First of all I would like to express my heartfelt gratitude to Allah, the Almighty creator, for His blessings in each and every step of my life.

I would like to express my sincere gratitude to my supervisors, Dr. Maria Stepanova and Dr. Steven Dew, for their guidance, motivation and support while pursuing my Ph.D. degree. I am lucky to have two such wonderful persons as my supervisors, who could be the role models to follow to become successful in life. They inspired me to think like a researcher as well as to formulate, present, and defend my views in a comprehensible manner. The thousands of hours they devoted to my education and research to uplift my understanding of the subject matter and beyond cannot be expressed in a few complementary words and will always be respected and remembered.

I would also like to sincerely thank the supervisory committee members of my Ph.D. thesis, Dr. Jie Chen and Dr. Michael Brett for their valuable comments to improve the quality of this thesis. It is my pleasure to thank Dr. Taras Fityo of NINT for his cooperation and valuable discussion. I also thank PhD candidate Francisco J. Jimenez for assistance to carry out experiments using the sputtering system.

I am forever indebted to my parents and siblings for all their motivation, love and support in my entire life. I owe my earnest gratitude to my beloved wife and

source of motivation, my son. Without their support, patience and love, this long journey of Ph.D. study would never have been possible.

This thesis was supported by funds from NSERC, NINT and the University of Alberta. I thank them all for the wonderful support.

*To my parents and family:
My wife and my son.*

Table of Contents

<i>CHAPTER: ONE</i>	1
1 INTRODUCTION	1
1.1 Background and Motivation	2
1.2 Common PVD Methods	4
1.2.1 Evaporation.....	5
1.2.2 Sputter deposition.....	6
1.2.3 Comparison of evaporation and sputtering.....	7
1.2.4 Epitaxy.....	7
1.3 Fabrication of Self-Assembled Arrays of Nanocrystals	8
1.4 Properties and Applications of Nanocrystals.....	13
<i>CHAPTER: TWO</i>	17
2 THEORY AND MODELING	17
2.1 Molecular Mechanisms of PVD Synthesis of Nanocrystals.....	17
2.2 Thermodynamics of Nucleation	21
2.3 The Kinetics of Island Nucleation and Growth.....	23
2.4 Modeling and Simulation	29
2.4.1 MD modeling.....	29
2.4.2 KMC modeling.....	30
2.4.3 Continuum kinetic modeling	32
2.4.4 The integrated multiscale scheme.....	33
<i>CHAPTER: THREE</i>	36
3 LATTICE BASED 2D MODEL.....	36
3.1 The Model Description	36

3.2 Simulation Process	40
3.3 Results and Discussion	41
3.3.1 Time evolution of the surface morphology for two model substrates	41
3.3.2 Effect of deposition rate	49
3.3.3 Effect of the kinetic factor K	56
3.3.4. Effect of diffusivity and temperature.....	58
3.3.5 Random Number Generation and Its Effect on Results	65
3.4 Summary.....	68
<i>CHAPTER: FOUR</i>	72
4 LATTICE BASED 3D MODEL.....	72
4.1 The Model Description.....	72
4.2 Results and Discussion	79
4.2.1 Evolution of surface morphology during deposition of nanocrystals.	79
4.2.2 Control of NC synthesis by varying the deposition rate.....	84
4.2.3 Effect of temperature and surface binding energy.....	92
4.2.4 Rotation of crystals.....	102
4.3 Summary.....	103
<i>CHAPTER: FIVE</i>	104
5 DEFECTS ANALYSIS	104
5.1 Point Defects	104
5.2 Line Defects	109
5.3 Area Defects	112
5.4 Comparative Analysis of Defects' Influence.....	115
5.5 Summary	119
<i>CHAPTER: SIX</i>	120

6	OFF-LATTICE MODEL.....	120
6.1	The Model Description.....	121
6.1.1	Inter atomic potential.....	122
6.1.2	Minimization method.....	124
6.2	Simulation Process.....	127
6.2.1	Boundary conditions.....	128
6.2.2	Substrate potential treatment.....	129
6.3	Monolayer Off-lattice Model (2D Mode).....	129
6.3.1	Evolution of surface morphology due to constant deposition.....	130
6.3.2	Effect of deposition rate.....	131
6.3.3	Effect of Temperature.....	133
6.4	Multilayer Off-lattice Model (3D Mode).....	134
6.4.1	3D off-lattice model results.....	136
6.5	Comparison between On-Lattice and Off-Lattice Models.....	138
6.6	Summary.....	139
	<i>CHAPTER: SEVEN</i>	140
7	SUMMARY AND CONCLUSIONS.....	140
7.1	Thesis Contribution.....	140
7.2	Outlook for Future Work.....	145

List of Figures

- Figure 1.1. (a) Schematic diagram of a PVD process; (b) thin film growth..... 5
- Figure 1.2. (a) ZnO tips on Si from thermal evaporation [27]. (b) GaAs tips on Si from sputter deposition [26]. (c) NCs of CoCr_2O_4 from sputter deposition [30]. (d) Gold nanoparticle grown on graphite by evaporation [25]. (Reprinted with the permission of Elsevier, American Physical Society and American Chemical Society.)..... 9
- Figure 1.3. TEM images (200 nm x 200 nm) of nanopatterns on glass (SiO_2) at ambient temperature for (a) Cu deposition times of 10, 30 and 60 seconds, and (b) Ag deposition times of 5, 30 and 120 seconds[15]. (Reprinted with the permission of Springer Science & Business Media.) 10
- Figure 1.4. (a) STM images (25 nm x 25 nm) of $\theta = 0.1$ Ag/Ag(100) deposited at 0.006 ML/s at temperatures of 225, 250 and 300 K. [16](b) STM image of Fe growing on Fe (100) at temperatures of 293, 453 and 523 K [32]. (Reprinted with the permission of American Physical Society.)..... 11
- Figure 1.5. STM images (a-c) of Cu on Cu (001) for 100 x 100nm at T=296 K with coverage θ , (a) 0.08 ML, (b) 1.0 ML at R=0.16 ML/s and (c) 8 ML at R=0.2 ML/s [33]. STM images (d-f) of Cu on Cu (100) at R=0.0208ML/s and T=299 K. (d) and (e) show an area of 100 x 100 nm while (f) is 500 x 500 nm [34]. (Reprinted with the permissions from Springer Science & Business Media B.V. and American Physical Society.)..... 12
- Figure 1.6. Nanocrystals based memory device fabrication process [29]. (Reprint with the permission of IEEE) 15
- Figure 1.7. (a) Sketch of two new surfaces being created by breaking a rectangular solid into two pieces. (b) The percentage of surface atoms changes with the Pd cluster diameter [42]..... 16
- Figure 2.1. Physical process behind nanoparticle growth: (1) deposition, (2) diffusion, (3) nucleation, (4) attachment, (5) detachment, (6) edge diffusion,

(7) diffusion down step, (8) nucleation on top of islands, (9) dimer diffusion [45].....	18
Figure 2.2. Modes of crystal growth [43].	19
Figure 2.3. Basic atomistic nucleation process on the substrate surface during vapour deposition [4].....	20
Figure 2.4. Free energy change (ΔG) as a function of nucleus radius (r) [4].	22
Figure 2.5. Schematic dependence of $N(t)$ with time and substrate temperature $T_1 > T_2 > T_3 > T_4$ [4].....	24
Figure 2.6. Arrhenius plot of saturation island densities measured at $R=0.12$ ML for Ag/Pt (111) [53]. The values i indicate the anticipated critical nucleation size. (Reprinted with the permission of American Physical Society.)	27
Figure 2.7. Scaling of N_{av} with R at 295 K. Open and solid symbols are experimental data taken on two different Ag(100) substrates [31]. (Reprinted with the permission of Elsevier).....	27
Figure 3.1. Two models for the lateral interaction of adatoms: (a) Model 1, primitive square lattice and (b) Model 2, FCC lattice. The black rectangles indicate the adatom and the numbers indicate the allowed positions to which it can jump.	37
Figure 3.2. Percentage of substrate coverage (a) and island size (b) as functions of time. Simulations correspond to Ag deposition at $T= 300$ K and $R=0.0093$ ML/sec.	42
Figure 3.3. Simulated surface morphologies demonstrating Ag islands' growth for deposition times of (i) 5 sec, (ii) 30 sec, (iii) 1 minute and (iv) 2 minutes for Model-1 at $T= 300$ K and $R=0.0093$ ML/sec.	44
Figure 3.4. Simulated surface morphologies demonstrating Ag islands' growth for deposition times of (i) 5 sec, (ii) 30 sec, (iii) 1 minute and (iv) 2 minutes for Model-2 at $T= 300$ K and $R=0.0093$ ML/sec.	45
Figure 3.5. The average size (a) and density (b) of islands as functions of the deposition rate, with constant 1 min duration of deposition for Ag deposition using Model 1 at $T=300$ K.....	50

Figure 3.6. The average size (a) and density (b) of islands as functions of the deposition rate, with constant 23% coverage, for Ag deposition using Model 1 at T=300 K. Also in (b) is a power law relationship for comparison.	51
Figure 3.7. Simulated surface morphologies for Ag deposited at T= 300K with varying deposition rates at constant duration of 1 min.....	53
Figure 3.8. Simulated surface morphologies for Ag deposited at T= 300K with varying deposition rates at constant coverage of 23%.	54
Figure 3.9. Average size of islands as a function of the kinetic parameter K, obtained by varying the number of diffusion steps at a constant 50% coverage (triangles), and by varying the number of deposition steps at a constant 23% coverage (squares), for 300 K deposition of Ag with Model 1.	57
Figure 3.10. Average size of islands as a function of the number of diffusion steps N_{diff} (see Eq.3.3) at a constant 50% surface coverage for Ag deposition with Model 1.....	59
Figure 3.11. Average size of islands as a function of temperature at a constant 50% coverage for (a) two metals Cu and Ag with Model 2 (b), and Cu with Model 1 and Model 2.....	60
Figure 3.12. Simulated surface morphologies for Ag deposition on Model 2 at temperatures of (i) 250K, (ii) 300K, (iii) 350K and (iv) 400K for 1 min deposition at R=0.0093ML/sec.....	62
Figure 3.13. Simulated surface morphologies for Cu deposition on Model 2 at temperatures of (i) 250K, (ii) 300K, (iii) 350K and (iv) 400K for 1 min deposition at R=0.0093ML/sec.....	63
Figure 3.14. Average density of islands as a function of temperature for Cu and Ag with Model 1.....	64
Figure 3.15. The dependence of island size on the deposition rate for the conditions from Fig. 3.5(a). Solid line represents the result of seed 1 and the dotted line is the average of the 6 runs (Table 3.2) to show the effect of the random number variation.....	68

Figure 4.1. Model for FCC lattice. The white rectangles indicate the allowed positions for occupancy. (a) Odd layer (b) Even layer (c) Cross sectional view and (d) 3D structural view.	74
Figure 4.2 (a). Flowchart of 3D KMC lattice simulation process.	77
Figure 4.2 (b). Diffusion steps simulation flowchart.	78
Figure 4.3. Simulated surface morphologies demonstrating Cu islands' growth for deposition times of 5 sec, 30 sec and 60 sec at $T= 300$ K and $R=0.086$ ML/sec or 0.2 nm/sec. (a) The 3D view of the substrate, (b) the 2D view of the same images, (c) the 2D height-height correlation function, and (d) the 1D height-height correlation function of the above substrates.	79
Figure 4.4. Average island size (S) and inter-island distance (δ) as functions of time (t) at the deposition rate $R=0.086$ ML/sec and $T=300$ K.	82
Figure 4.5 (a). Effect of deposition rate and time on the 3D surface morphology. Gradual changes of NC size and shape observed due to changes in parameter R (ML/sec) and t (sec) at $T=300$ K, $y_s=y=0.39$ eV; 3D view.....	85
Figure 4.5 (b). Effect of deposition rate and time on the surface morphology. Gradual changes of NC's' size and shape observed due to change in parameter R (ML/sec) and t (sec) at $T=300$ K, $y_s=y=0.39$ eV; 2D view.....	86
Figure 4.6. Effect of deposition rate at fixed time 30 sec, for (a) deposited substrate and (b) 1D H-H correlation. Effect fixed coverage 2.6ML for (c) deposited substrate and (d) 1D H-H correlation. All sim	88
Figure 4.7. (a) The average island density and (b) average inter-island distance, as functions of the deposition rate R , for fixed time $t=30$ sec and for fixed coverage of $\theta=2.6$ ML , at $T=300$ K.....	89
Figure 4.8 (a). Effect of temperature and the adatom-substrate binding on the surface morphology. Gradual changes of NC's size and orientation observed due to change in temperature T and parameter y_s/y at $t=30$ sec, $R=0.086$ ML/sec, $y=0.39$ eV; 3D view.....	93
Figure 4.8 (b). Effect of temperature and the adatom-substrate binding on the surface morphology. Gradual changes of NC's' size and orientation observed	

due to change in temperature T and parameter y_s/y at t=30 sec, R=0.086 ML/sec, $y=0.39$ eV; 2D view.....	94
Figure 4.9. Effect of temperature (T=250 to 350K) (a) substrate, (b) the respective correlation function. Effect of substrate binding energy ($y_s=0$ to $2y$), (c) substrate, (d) the respective correlation function at T=300K, R=0.086ML/Sec.	96
Figure 4.10. Average inter-island distance (a) and average island height (b) as a functions of the binding energy ratio (y_s/y) at T=300 K, for t=30 sec, R=0.086 ML/sec, $y=0.39$ eV.	98
Figure 4.11. Average island size and inter-island distance (a) and average island height (b) as functions of temperature (T), at t=30 sec, R=0.86 ML/sec, $y_s=y=0.39$ eV.	99
Figure 4.12. Average density of islands as a function of temperature ($1000/T$) for t=30 sec, R=0.86 ML/sec, and three different values of y_s . Symbols represent the numerical results and lines show the approximate slops.	101
Figure 4.13. Rotation of crystal due to change in temperature. (Correlation function results are presented in inverse way for better visibility).....	102
Figure 5.1. Examples of the hypothetical vacancy defects on the substrate: (a) perfect crystal without defects, (b) vacancy point defects, (c) vacancy line defects, and (d) vacancy area defects.	105
Figure 5.2. Vacancy point defects in 2D model of a NC array: (a) nanocrystalline array on the original substrate without defects, (b) nanocrystalline array on a substrate with 1% defects, (c) nanocrystalline array on a substrate with 4% defects, and (d) nanocrystalline array with 8% defects.	107
Figure 5.3. Vacancy point defects in the 3D model of a NC array. The 2D view, 3D view and the height-height correlation functions of (a) original substrate without defects, (b) substrate with 5% defects, and (d) with 10% defects..	108
Figure 5.4. Vacancy line defects in the 2D model; (a) original substrate without defects, (b) substrate with 8 line [010] defects, (c) with 16 line defects, (d) with 32 line defects, (e) with [001] line defects and (f) with [011] line defects.....	110

Figure 5.5. Vacancy line defects in the 3D model. The 2D view, 3D view, and the height-height correlation functions for: (a) original substrate without defects, (b) line defects in [010] direction, (c) [001] direction, and (d) [011] direction.	111
Figure 5.6. Vacancy area defects in the 2D model: (a) original substrate without defects, (b) substrate with 1% defects, (c) substrate with 4% defects, and (d) with 8% defects. The defects are indicated as white areas.	113
Figure 5.7. Vacancy area defects in 3D model: The 2D view, 3D view and the height-height correlation functions of (a) original substrate without defects, (b) substrate with 2.5% defects and (d) with 5% defects.	114
Figure 5.8. Comparison of the effect of various defects on NC size with increasing defects in the 2D model.	115
Figure 5.9. Effect of point defects on the temperature dependence of NC size in the 2D model.	116
Figure 5.10. Effect of temperature on the 3D morphology: (a) original substrate, and (b) in the presence of 5% point defects.	117
Figure 5.11. Effect of temperature on the 3D morphology (a) with line defects and (b) with area defects.	118
Figure 6.1. (a) Lattice based model structure and (b) off-lattice model structure.	121
Figure 6.2. A graph of strength versus distance for the Lennard-Jones potential.	123
Figure 6.3. (a) Finding the minimum; (b) multiple minima within a cell; (c) selecting the appropriate minimum point and based on jump probabilities using the metropolis algorithm (eq.3.4).	126
Figure 6.4. Process flow diagram of the off-lattice model.	128
Figure 6.5. 2D off-lattice simulation results for 12.5 nm x 12.5 nm area. (a) With corresponding search grids and potential minima location and (b) without the grid or minima position shown.	129
Figure 6.6. Simulation of 12.55 nm x 12.5 nm area at various times (5-180 sec) at R=0.006 ML/sec and T=300 K.	130

Figure 6.7. Simulation for constant time of 30 sec at various deposition rate R=0.0004 ML/sec to R=0.024 ML/sec, at T=300 K.....	131
Figure 6.8. Simulation for constant coverage $\theta=0.375$ ML at various deposition rates R=0.0025ML/sec to R=0.375ML/sec, at T=300 K.....	132
Figure 6.9. Effect of temperature on the 2D off-lattice model for R=0.006ML/sec for t=30 sec.	133
Figure 6.10. Diffusion steps as a function of temperature with R=0.006ML/sec.	134
Figure 6.11. (a) Lattice based 3D model; (b) 3D off-lattice model; (c) simulated area of $3.5nm \times 3.5nm$. The substrate atoms are blue and the deposited atoms are red.	135
Figure 6.12. Change in surface morphology at R=0.051 ML/sec and T=300K.	136
Figure 6.13. Effect of temperature on the morphology in the 3D off-lattice model with R=0.051 ML/sec, t= 30 sec.	137
Figure 7.1. A prospective integrated multiscale simulation approach including the developed KMC models.	146
Figure 7.2. Proposed integrated system for accelerating the self-assembled nanosynthesis process development.	147

List of Tables

Table 1-1. Comparison of PVD method evaporation and sputtering.....	7
Table 2-1. Comparison of modeling techniques. (Reprinted with the permission of Elsevier and Springer)	33
Table 3-1. Geometries and numbers of neighbor atoms for 6 characteristic adatom locations in Model 1 and Model 2. Solid arrows show the bonds. Dashed lines indicate boundaries of hypothetical islands.	47
Table 3-2. Island size of different sets of simulation at a given deposition rate, their average and standard deviation, for the conditions from Fig. 3.5(a). ...	67
Table 6-1. Comparison between lattice based model and off-lattice model size and time of operation with similar R , T and θ . Execution using INRF computing facility system of AMD six core Opteron 2.6GHz processor and the 64GB RAM.	139

CHAPTER: ONE

1 INTRODUCTION

Nanotechnology is rapidly becoming one of the most influential drivers of technical development. Currently transistors sized $32nm$ are used in industrial production and $22nm$ size is on the way [1]. Nanocrystal (NC) synthesis is an important process due to its ability to improve performance of electronic and photonic devices [2]. Thin film technology including nanocrystalline synthesis is the underlying basis of a wide range of applications. Many of these applications require fine control of film structure at the nanometer scale. Such control is enabled by an insight from comprehensive and systematic theoretical and numerical research. In particular, detailed numerical modeling of self-assembled synthesis of NC's is a subject of constantly growing interest [3]. A comprehensive software tool for modeling NC synthesis will have significant value for industry as well as in academia. In this work, I present a technique I have developed to model and optimize a process of NC synthesis. My research focuses on NC synthesis by Physical Vapor Deposition (PVD) methods. PVD is one of the most flexible, efficient, and clean techniques to fabricate nanopatterns [4]. However size, shape and density of self-assembled NC are highly sensitive to the process conditions such as duration of deposition, temperature, substrate material, etc [2]. To efficiently synthesize NC arrays by PVD, the process control factors should be understood in detail. With the increase of computing power numerical modeling of self-assembled synthesis of NC has grown lot of attraction

[3]. Popular approaches to simulate nanocrystalline film growth include Molecular Dynamics (MD) simulation [5-7], Kinetic Monte Carlo (KMC) simulation [8-14], and analytic continuum theories [15, 16]. The performance of these simulation techniques depends on the size, time scale, and other details of the process to be studied. Among the existing numerical methodologies, KMC favorably combines flexibility, predictive power, and numerical efficiency, and as such is very well suited for both basic understanding of NC growth and applications for in-silico aided design of nanofabrication processes. KMC simulation of film deposition is an important tool for understanding the mechanisms of this process. I developed a realistic KMC model that explicitly represents PVD synthesis of self-assembled NCs, showing how varying critical process parameters such as deposition rate, duration, and temperature affect the morphologies of self-assembled metallic islands on substrates, and comparing the results with experimentally observed surface morphologies generated by PVD from the literature.

1.1 Background and Motivation

The Nobel-prize winning physicist, Richard Feynman, in his visionary lecture at the American Physical Society meeting at Cal Tech in 1959 said that “There is plenty of room at the bottom” [17]. He also mentioned that the problems of chemistry and biology can be greatly helped if our ability to see what we are doing, and to do things on an atomic level. Typical sizes considered in nanotechnology range from 1 to 100nm corresponding to objects comprising from

a few atoms to a few tens of thousands of atoms. Structures on this size scale exhibit unique and novel properties, vastly different from the bulk material. These properties originate either from spatial confinement of a physical entity inside a specified volume or from the significant volume fraction of material located near surfaces, interfaces or domain walls. Fabrication and manipulation of these nanostructures is therefore a fundamentally exciting and technologically important area of research.

Self-assembly of nanoscale metallic islands on various crystalline or amorphous substrates presents a strong interest for nanotechnology applications. However, synthesis of functional crystalline nanostructures requires control over the nanocrystalline morphology for which, in turn, the dependence of the morphology on the deposition process conditions should be well understood.

The basic physical mechanisms behind the nucleation and growth of deposited films have been extensively addressed in the literature. At the early stages of deposition, incident atoms randomly impinge on the substrate at a given rate, chemically or physically adsorb and then re-evaporate, aggregate, or diffuse [18]. Coalescence of adatoms results in nucleation of tiny nanoislands on the substrate. Islands containing more adatoms than a critical nucleation number [19, 20] give rise to relatively stable NCs, whose size increases due to the arrival of new adatoms at the surface [21].

Presently, there is a strong need for an ability to synthesise nanostructures with a well-defined size and shape in order to exploit the unique properties presented on this scale which can ultimately result in industrial and commercial applications. This requires a detailed understanding of the NCs growth process beyond the basic elementary mechanisms. Even though valuable information can be extracted from experiment, this can be a very time consuming and costly process. However, one can exploit modelling and perform "computer experiments" to aid in elucidating the mechanisms responsible for nanostructure growth and to provide guidelines for tailoring nanostructure size and shape. This is the approach followed in this work, where the growth of nanostructures via physical vapour deposition is studied.

The primary objectives for this work were to establish a model for the simulation of nanostructure growth on a substrate by PVD. It must be emphasised that the focus of this work was to study the processes involved in nanostructure growth and to develop a model to perform simulations on a nanometre scale. It was also endeavoured that this model should be sophisticated enough so that further development and enhancement can easily follow.

1.2 Common PVD Methods

Our modeling technique focuses on PVD methods, which involve vaporising the material and then depositing it by condensation on various surfaces. The method employs purely physical processes such as high temperature vacuum evaporation,

plasma sputter bombardment, epitaxial growth etc. Common PVD methods are described below. Fig. 1.1 shows a generic schematic diagram of a PVD system and the film growth process.

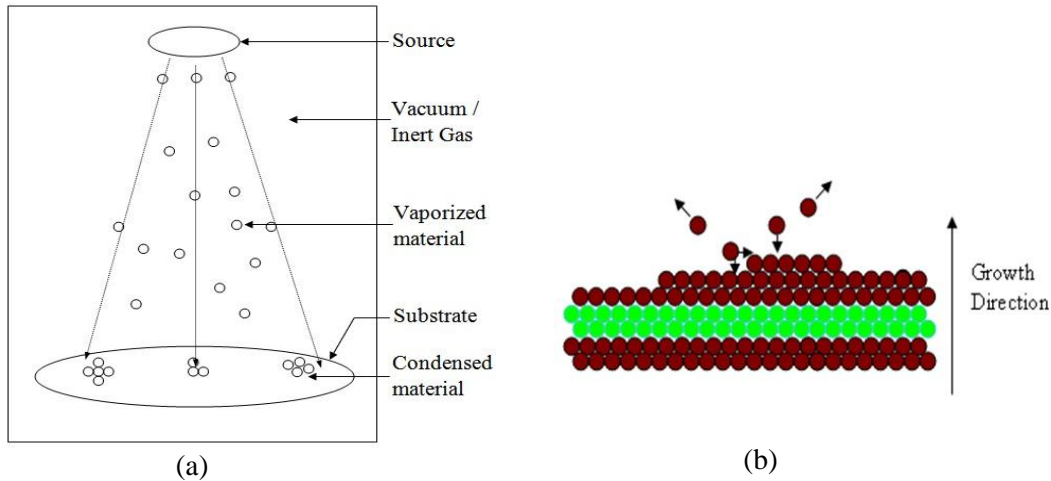


Figure 1.1. (a) Schematic diagram of a PVD process; (b) thin film growth.

1.2.1 Evaporation

Thermal evaporation is a widely used PVD method. The idea of this process is to transfer atoms from a heated source to a substrate where film formation and growth occur. This method uses heating to transform the source material into the vapour state within a vacuum chamber. Vacuum is required to allow the molecules to move freely in the chamber. The vapour subsequently condenses on the cooler substrate surfaces. Depending on substrate conditions, this can form nanostructured coatings. The techniques used to evaporate the target differ. The simplest evaporation technique is the resistive heating technique, whereas electron beam evaporation is used for greater control and for refractory metals [22, 23].

The advantage of evaporation is simplicity. However, due to challenge in achieving good stoichiometry consistency and coverage, other PVD methods such as sputtering can provide a higher quality film deposition.

1.2.2 Sputter deposition

Another popular PVD method is sputtering. In this method, an atom is ejected from a liquid or solid target at room temperature by bombarding its surface with energetic ions. Then the atoms traverse a reduced pressure ambient and are deposited on the substrate.

The sputtering process is widely used in the semiconductor industry mainly for metal film formation for various purposes. This method is very well established. In a classical sputtering system, a vacuum chamber is filled with argon gas. Plasma is created by applying a high voltage and the resulting accelerated argon ions (Ar^+) hit the target to produce vaporised material by ballistic sputtering. The sputtered target atoms travel to the substrate surface to form a nanostructured coating. Direct Current (DC) sputtering is the simplest sputtering method using the target as cathode and substrate as anode. It is however not possible to sputter dielectric material targets. Radio frequency excitation overcomes this limitation by creating a net DC bias on the target surface due to the plasma diode effect. Applying a magnetic field in the system strongly increases the ionization density by trapping electron close to the target. Such a process is known as magnetron

sputtering. There are several other types of sputtering systems. However, the basic principles are similar for all of them. Some specific systems might possess advantages over others in specific application [4]. A comparison between two common PVD methods, evaporation and sputtering, is given below in the Tab. 1.1.

1.2.3 Comparison of evaporation and sputtering

Table 1-1. Comparison of PVD method evaporation and sputtering.

	EVAPORATION	SPUTTERING
1	Low energy atoms	Higher energy atoms
	High vacuum, long free path <ul style="list-style-type: none"> • few collisions • line of sight deposition • little gas in film 	Low vacuum, short free path <ul style="list-style-type: none"> • few to many collisions • less line of sight deposition • gas in film
2	Generally, larger grain size	Generally, smaller grain size
3	Fewer grain orientations	Many grain orientations
4	Poorer adhesion	Better adhesion

1.2.4 Epitaxy

Molecular beam epitaxy (MBE) can also be classified as a PVD. The MBE method can produce layers of materials with atomic control. This is done by creating a 'molecular beam' of a material which impinges on to the substrate. MBE was developed in the early 1970s as a means of growing high-purity epitaxial layers of compound semiconductors, and is routinely used for growing III-V compound semiconductor heterostructures. MBE can produce high-quality

layers with very smooth interfaces and good control of thickness, doping, and composition. Because of the high degree of control possible with MBE, it is a valuable tool in the development of sophisticated electronic and optoelectronic devices. It is, however, slow and expensive.

1.3 Fabrication of Self-Assembled Arrays of Nanocrystals

Nanoscale crystalline materials, nanostructures and nanowires are tiny particles with properties different from related bulk materials. These properties can be useful for enhanced functionality of electronic and optoelectronic devices. Synthesis of NCs by various methods is one of the most popular topics in the literature of nanotechnology [2, 24-29]. A large number of publications on PVD synthesis of functional nanostructures indicate the high potential of the method. The most popular PVD methods found in many studies of NC formation are sputtering and evaporation followed by annealing. Fig. 1.2 shows the images of several examples of fabricated nanocrystalline arrays.

Metallic NCs have great potential in nanotechnology and the present study targets the deposition of NCs of metals such as Cu and Ag. The experimentally observed morphologies shown in Figs. 1.3 and 1.4 demonstrate that the shape of deposited metallic islands depends on the substrate and condition.

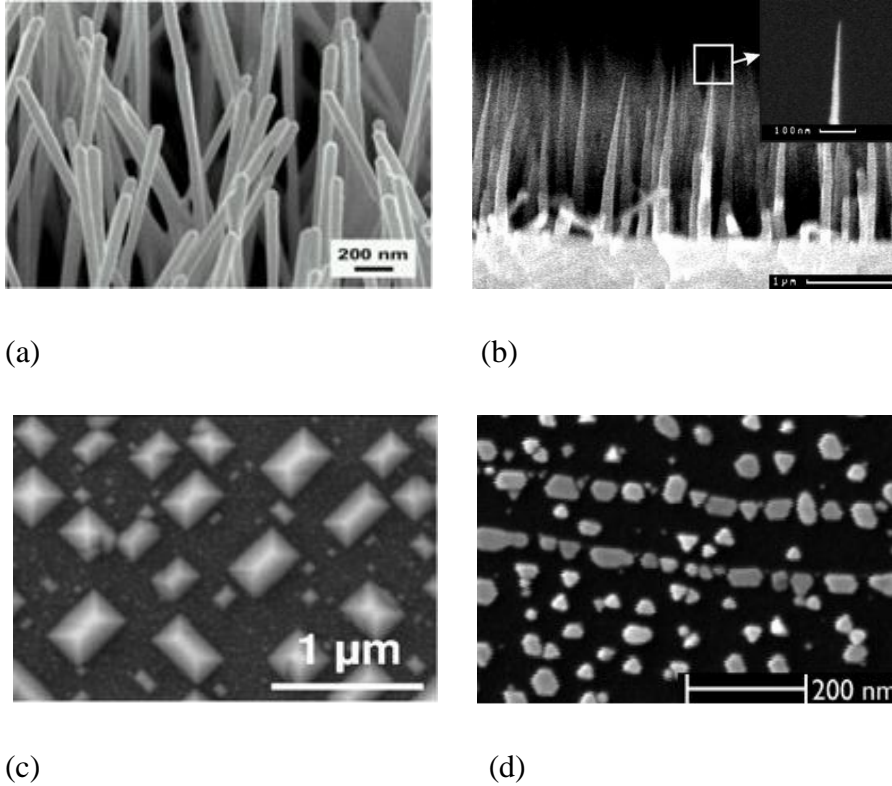
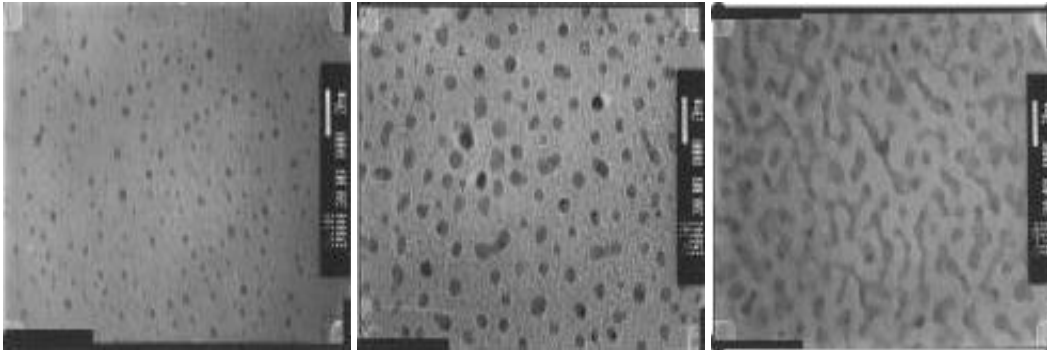


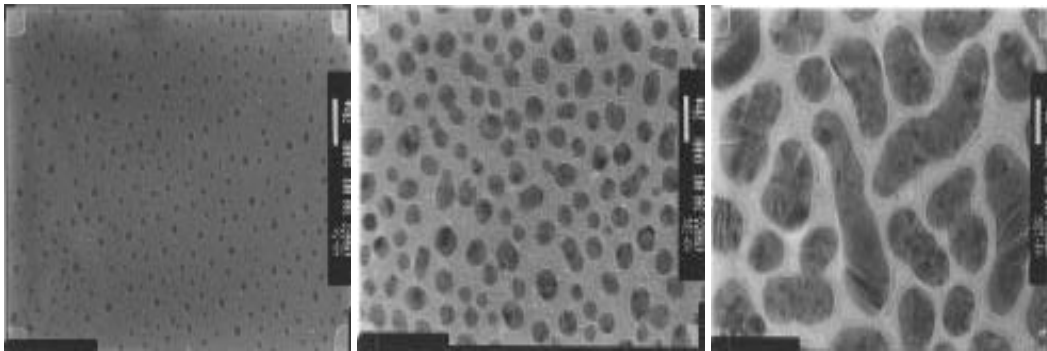
Figure 1.2. (a) ZnO tips on Si from thermal evaporation [27]. (b) GaAs tips on Si from sputter deposition [26]. (c) NCs of CoCr_2O_4 from sputter deposition [30]. (d) Gold nanoparticle grown on graphite by evaporation [25]. (Reprinted with the permission of Elsevier, American Physical Society and American Chemical Society.)

As can be seen in Fig. 1.3, under typical conditions, metal islands deposited by PVD techniques on amorphous substrates such as amorphous SiO_2 often undertake smooth droplet-like shapes [15]. At a later stage of deposition, some of these patterns resemble percolation networks (see the last picture of Fig. 1.3 (a)).

In contrast, when a metal is deposited on a crystalline substrate [16, 31, 32], the islands adopt more regular “crystal-like” shapes, as shown in Fig. 1.4.



(a)



(b)

Figure 1.3. TEM images (200 nm x 200 nm) of nanopatterns on glass (SiO₂) at ambient temperature for (a) Cu deposition times of 10, 30 and 60 seconds, and (b) Ag deposition times of 5, 30 and 120 seconds[15]. (Reprinted with the permission of Springer Science & Business Media.)

The crystalline morphology persists when temperature increases, which is evident from the images in the figure. With continuing deposition, the islands start merging and the pattern evolves into a continuous thin film. These late stages of

nanocrystalline synthesis also require appropriate simulation approaches capable of accounting for the changing surface morphology.

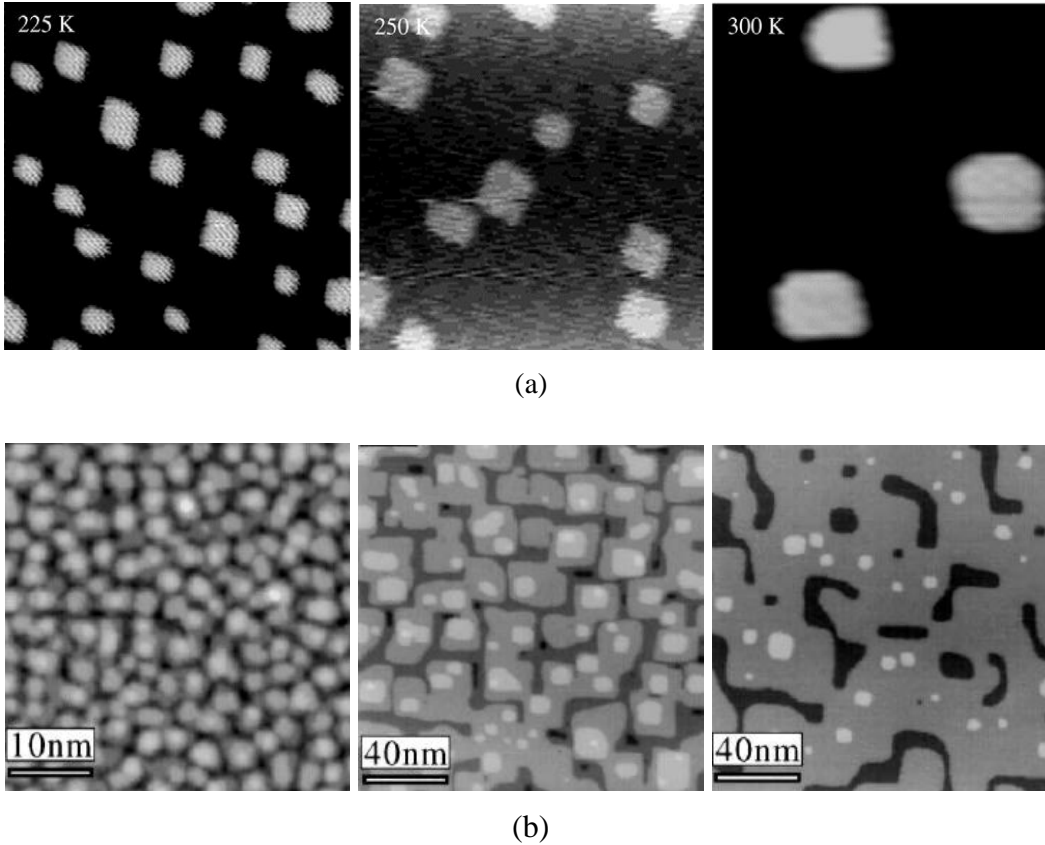


Figure 1.4. (a) STM images (25 nm x 25 nm) of $\theta = 0.1$ Ag/Ag(100) deposited at 0.006 ML/s at temperatures of 225, 250 and 300 K. [16](b) STM image of Fe growing on Fe (100) at temperatures of 293, 453 and 523 K [32]. (Reprinted with the permission of American Physical Society.)

Fig.1.5 illustrates the growth of Cu islands on a crystalline Cu substrate during a PVD process [33, 34]. Metal deposition on crystalline surfaces starts producing arrays of islands, which grow in size over the time and evolve into 3D

nanocrystalline morphologies. The evolution of deposited metal from tiny nano-island into pyramid like NC's is shown in the figures below.

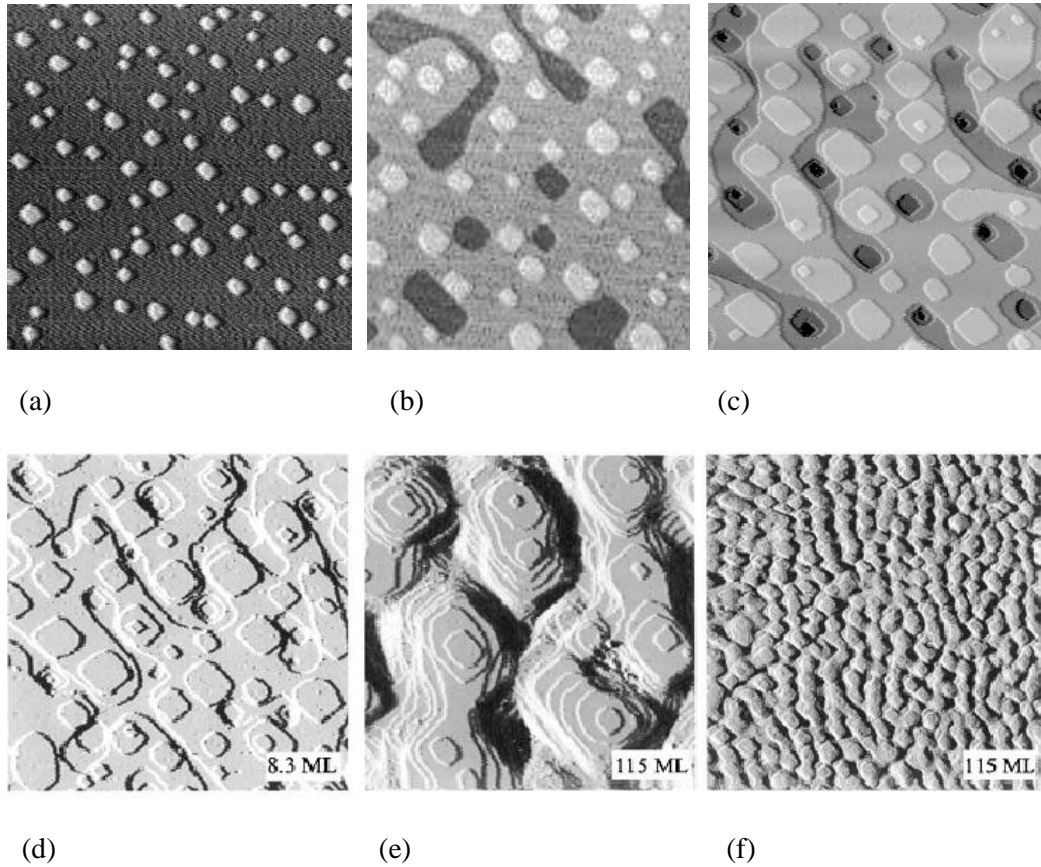


Figure 1.5. STM images (a-c) of Cu on Cu (001) for 100 x 100nm at T=296 K with coverage θ , (a) 0.08 ML, (b) 1.0 ML at R=0.16 ML/s and (c) 8 ML at R=0.2 ML/s [33]. STM images (d-f) of Cu on Cu (100) at R=0.0208ML/s and T=299 K. (d) and (e) show an area of 100 x 100 nm while (f) is 500 x 500 nm [34]. (Reprinted with the permissions from Springer Science & Business Media B.V. and American Physical Society.)

Fig.1.5 (a) shows an early post-nucleation stage when tiny metallic islands have just arisen and Figs.1.5 (b) and (c) demonstrate how the morphology evolves. It can be seen that multilayer structures arise even before the first monolayer is complete and some of the new nucleation events take place on top of previously deposited layers. It is possible to identify a characteristic rectangular shape that is observed both at the stage of island nucleation (Fig. 1.5(a)) and during the subsequent morphology evolution (Fig.1.5 (b,c)) The mounded structure and the square or rectangular symmetry of the morphology are apparent also in Figs.1.5(d-f) illustrating later stages of the deposition. The evolution of the mounded morphology, comprising the coarsening of the mounds as well as merging of their bases, is evident in the images.

1.4 Properties and Applications of Nanocrystals

Optical properties such as the scattering and absorption of light by arrays of nanoparticles differ significantly in comparison with bulk solids. It is observed that absorption of light by fine-grained metal films in the visible part of the spectrum shows absorption peaks which are absent in the spectra of bulk metals. Also, the dependence of the absorption of light on the wavelength from the visible to infrared part of the spectrum is different in nanostructured materials [2]. The differences in the absorption spectra of nanoparticles and bulk metals are caused by the differences of their dielectric permittivity. The size dependence of the optical properties is important at the nanoscale, when particle size is considerably

smaller than the light wavelength. Optically active NCs have various applications. Thus, their non-linear optical behaviors are useful for various sensors applications and optical MEMS. In optoelectronic applications, ZnO NCs have potential for UV lasers and light emitting diodes [27, 35, 36]. NCs have applications in anti reflection coatings, gas sensors [37], and photo-luminescent devices. Nanostructures are also advantageous in photoelectric cell devices for highly efficient conversion of light to electrical power due to their large surface area [38, 39].

Furthermore, magnetic NCs synthesized on substrates or embedded into non-magnetic matrices have important application in ultra high density magnetic storage devices [40]. Nanomagnets can also be used for medical imaging, and sensing technology [41].

The charge storing property of NCs can also be useful in flash memory devices. Compared to conventional flash memory, NC based memory offers several advantages [22, 28, 29]. NC based memory can reduce tunnel oxides thickness which can lower operating voltages and increase the speed. Improved scalability results in robust and fault-tolerant devices. NC memories also suffer less from drain-induced-barrier-lowering (DIBL) and also have intrinsically better punch-through characteristics and excellent immunity to leakage current [29]. Fig. 1.6 shows a typical process sequence of a NC based memory device fabrication

process. Although the process demonstrated here was by atomic layer CVD (ALCVD), NC based flash memory can also be fabricated by PVD.

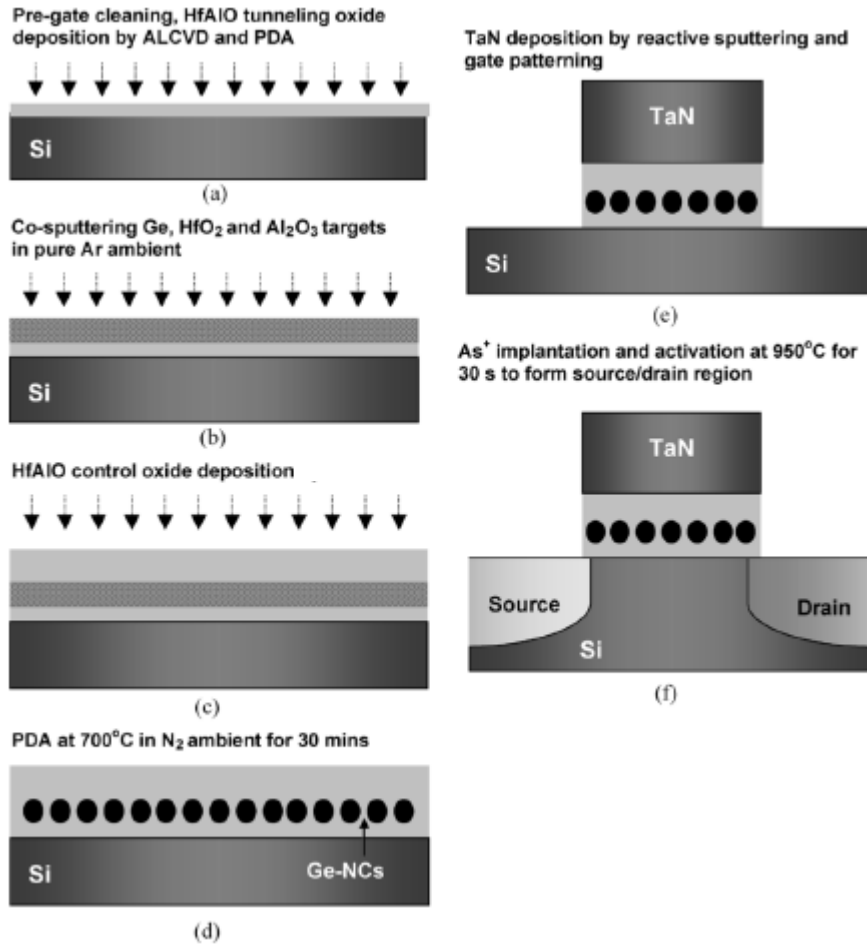


Figure 1.6. Nanocrystals based memory device fabrication process [29]. (Reprint with the permission of IEEE)

Due to the high surface area, many nanostructured materials are characterized by a very high surface energy, and thus, some of them are thermodynamically unstable or metastable. Fig. 1.7 shows how dramatically the surface to volume ratio increases for nano sized objects. In order to produce and stabilize

nanostructures and NCs, it is essential to have a good understanding of their properties.

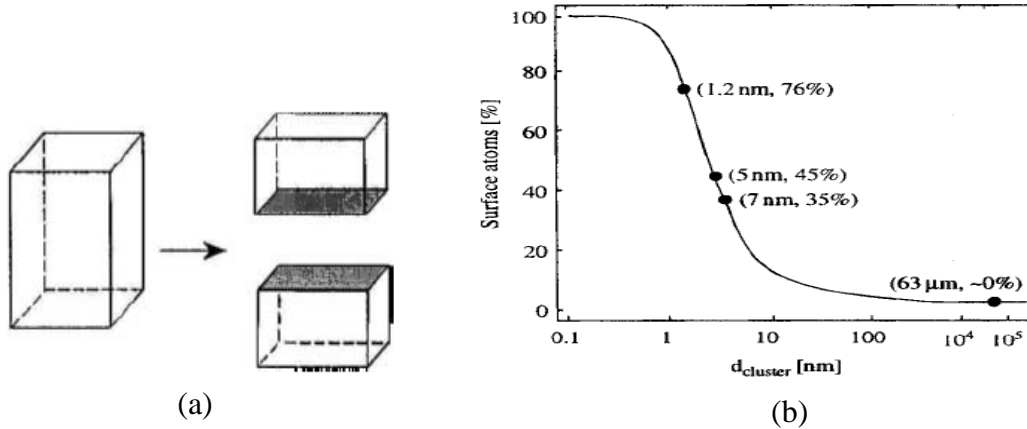


Figure 1.7. (a) Sketch of two new surfaces being created by breaking a rectangular solid into two pieces. (b) The percentage of surface atoms changes with the Pd cluster diameter [42].

Understanding of the complex interplay of the described kinetic, thermodynamic, and structural properties of NC is currently at an early stage. A detailed numerical research of these impacts is required to rationally select the optimal regimes of synthesis of NCs. While formulating a numerical model for NC growth, one needs to consider both the nanoscale structure of the film and the atomic-level detail of these structures [43, 44].

CHAPTER: TWO

2 THEORY AND MODELING

Understanding molecular mechanisms behind the PVD self-assembled growth of NCs is very important to efficiently synthesize NC arrays. Here I outline selected mechanisms of NC self-assembly and approaches to simulate nanocrystalline film growth.

2.1 Molecular Mechanisms of PVD Synthesis of Nanocrystals

During the early stages of film formation, vapour atoms or molecules are deposited on the substrate in a discontinuous manner. This stage of film growth is known as the nucleation stage. Many studies have been reported addressing both basic and applied aspects of the nucleation theory and modeling. At the early stage of PVD, atoms arriving on the substrate are adsorbed and start diffusing over surface, occasionally binding with other adatoms and forming tiny islands. Some atoms will also detach from the existing clusters due to thermal activation. Various mechanisms of the surface adatom mobility are shown in Fig. 2.1.

Because of the atom's mobility, some of the islands are unstable or metastable. A condition when stabilized clusters of atoms can be formed is called critical nucleation [19, 20, 42]. In the course of subsequent deposition, the stable clusters'

size increases due to arrival of new material, as well as by coarsening processes [8]. At later stages, the growing clusters start merging developing networks. If deposition continues, the structure evolves into a continuous thin film. The morphology is strongly dependent on the substrate type. Crystallographic symmetry and orientation are frequently replicated in the arrays of growing islands [4].

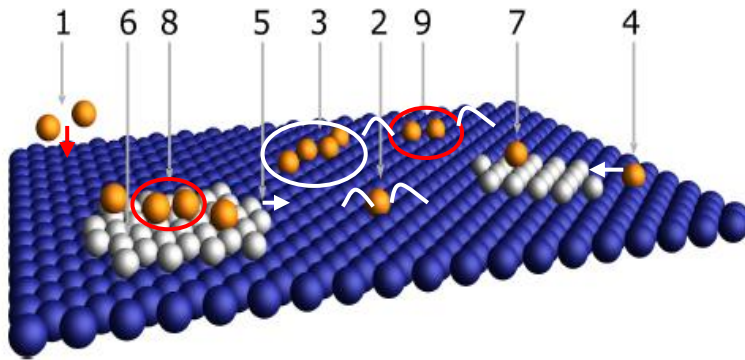


Figure 2.1. Physical process behind nanoparticle growth: (1) deposition, (2) diffusion, (3) nucleation, (4) attachment, (5) detachment, (6) edge diffusion, (7) diffusion down step, (8) nucleation on top of islands, (9) dimer diffusion [45].

The transitory regimes from individual stable nuclei to a developed continuous film can be classified in 3 major categories: (a) the Frank–van der Merwe (FM) mode, (b) the Volmer-Weber (VW) mode and (c) the Stranski-Krastanow (SK) mode, as shown in Fig. 2.2. The growth mode is determined by the relation between the surface and interface energies involved.

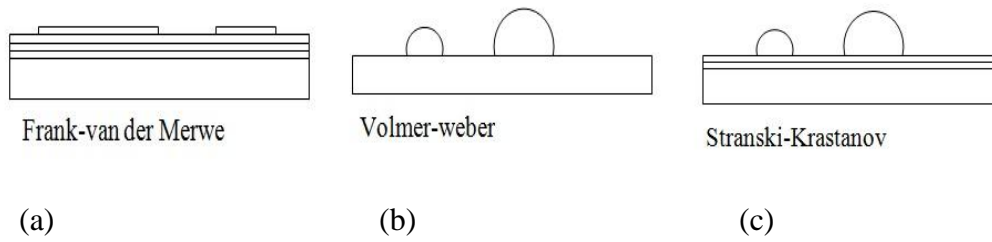


Figure 2.2. Modes of crystal growth [43].

In the FM mode, a single crystal or amorphous film covers the substrate and its thickness increase uniformly as additional material is deposited. This occurs when there is a good wetting between the film and the substrate. In the VM mode, the wetting is insufficient and as a result, the deposited material aggregates into individual nanoclusters on the substrate. The SK mode can be considered as an intermediate of the FM and VW modes, where a very thin single crystal film is formed first and on top of these individual NC's are formed. Young's model [4, 46] provides a way to distinguish and better understand the 3 modes of the film growth [47]. In this model it is easier to consider surface energy (J/m^2) as a surface tension (N/m) pulling on the surface to reduce its extent. Fig 2.3 shows the effective interfacial tension forces and the wetting angle θ defining the particle radius (ρ). The forces involved are the tension force between substrate and vapour (γ_{sv}), the tension force between film and substrate (γ_{fs}), and the tension force between film and vapour (γ_{fv}). In equilibrium their relationship is:

$$\gamma_{sv} = \gamma_{fs} + \gamma_{fv} \cos \theta . \quad 2.1$$

In the case of strong wetting when $\gamma_{sv} > \gamma_{fs} + \gamma_{fv}$, the equilibrium is broken and the wetting angle turns out to be $\theta=0$. In this case the deposition occurs in FM mode (layer by layer deposition) and individual islands are not formed. The condition for islands formation is $\gamma_{sv} < \gamma_{fs} + \gamma_{fv}$ meaning that $\theta > 0$. This corresponds to the VW mode of island growth. In the intermediate case when $\gamma_{sv} \geq \gamma_{fs} + \gamma_{fv}$, and $\theta \cong 0$, the deposited material wets the substrate, after which island can form as observed is SK mode. In this case, the strain in the growing film restores the balance of surface tensions, permitting stable nuclei to form above the initially deposited layers. In general, materials with low surface energy will wet substrates with a higher surface energy. Out of the three classical growth modes, the VW and SK modes of growth present the central interest for self-assembled synthesis of arrays of NCs.

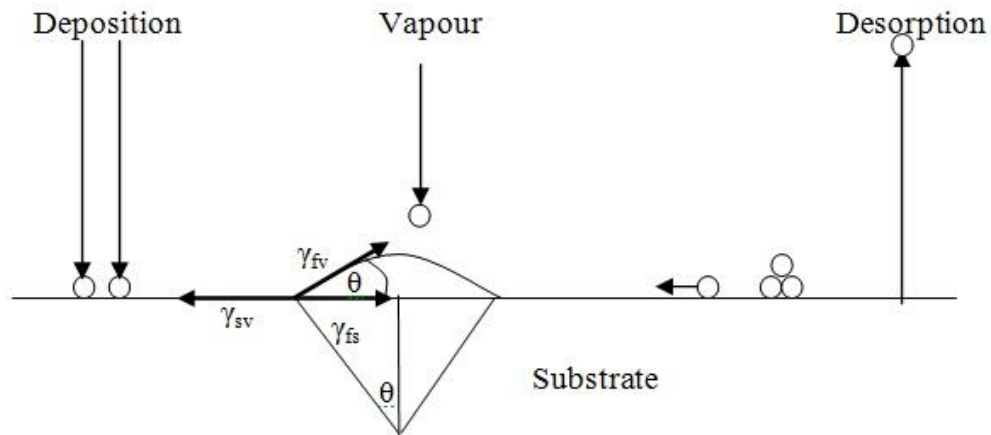


Figure 2.3. Basic atomistic nucleation process on the substrate surface during vapour deposition [4].

Later stages can also be classified as separate growth modes, such as the polycrystalline mode and the columnar mode [44]. The structure of the film at these later stages of deposition is determined by a sequence of morphological changes which occur as the film grows in thickness from discrete initial crystallites, and grain boundary migration, self-shadowing, diffusion and recrystallization start to contribute. The growth process is dependent on parameters such as the grain boundary energies, flux, atom adsorption probabilities, atom density and mobility. Beside these, atom energy, angle of incidence, the exposed crystallographic surfaces, the presence of foreign atoms and substrate temperature determine the structure of the crystalline film [44].

2.2 Thermodynamics of Nucleation

The early stages of NC synthesis by PVD methods are similar to the thin film formation by PVD process. Thermodynamical arguments applicable to thin films also clarify the trends relevant to NC synthesis. In brief, atoms at surfaces have an excessive energy in comparison with atoms within the bulk because they make fewer attractive bonds with surrounding atoms. The corresponding difference in the free energy is known as the surface energy. The relationship between the free energy and the critical diameter of the islands is shown in the Fig. 2.4. In the figure, ΔG is the Gibbs free energy change as a result of adatoms forming islands, r is the radius of the island, r^* is the critical nucleus size, and ΔG^* is the corresponding critical free energy barrier for nucleation [4]. Stability conditions

for nuclei are achieved when $\frac{d\Delta G}{dr} = 0$, which occurs at a critical nucleus radius $r=r^*$. Below this size, incipient nuclei will tend to break up back into diffusing adatoms.

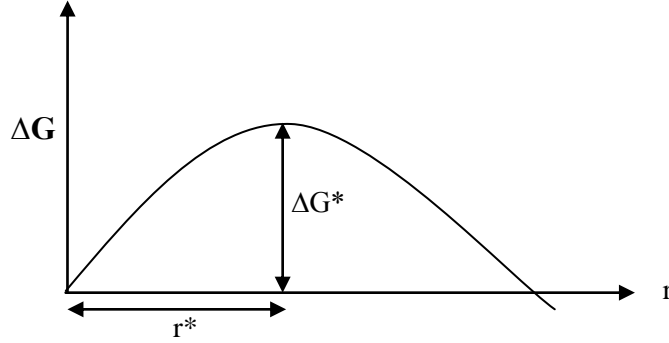


Figure 2.4. Free energy change (ΔG) as a function of nucleus radius (r) [4].

The distribution of the island density N over size can be expressed as follows [4],

$$N(r) = n_s \exp\left[\frac{-\Delta G(r)}{kT}\right], \quad 2.2$$

where n_s is the total nucleation site density, k is Boltzmann's constant and T is the temperature. It should be noted that thermodynamic quantities such as ΔG , γ or θ usually are not known precisely, nor are they easily measurable. While providing a valuable insight for interpretation of the wetting phenomena, the thermodynamical treatment should be complemented by other approaches in order to make specific numerical predictions.

2.3 The Kinetics of Island Nucleation and Growth

Nucleation rate can be described as the number of nuclei of critical size that form on a substrate per unit area, per unit time. The rate at which the nuclei arise depends on the rate at which adatoms are deposited on the substrate. The rate of nucleation also depends on the surface processes illustrated in Fig. 2.1. The statistical model of the nucleation, which is considered as the first order phase transition “vapour-solid”, has been described in detail in refs [4, 48, 49]. At early stages of deposition, the resulting nucleation rate \dot{N} is given by [4]:

$$\dot{N}_i = R a_o^2 n_o \left(\frac{R}{n_o v} \right)^i \exp \frac{(i+1)E_i - E}{kT}, \quad 2.3$$

where i is the critical nucleus size in atoms; R is the deposition rate at which atoms impinge at the surface; a_o is the distance covered by an adatom in a single diffusion jump; n_o is the number of adsorption sites per unit surface; v is the fundamental frequency of atomic vibration; E_i is a bond energy of a single atom, and E is the activation energy for surface diffusion. The nucleation rate represents the rate of formation of the smallest stable clusters. There are several other energies that may affect the nucleation rate such as the desorption energy, which are ignored in this discussion for simplicity. For the minimum stable island of two atoms, the critical nuclei size can be determined as: $i = 1$ [4] and the nucleation rate becomes,

$$\dot{N}_i = \frac{R^2 a_o^2}{v} \exp \frac{2E_i - E}{kT}. \quad 2.4$$

A more comprehensive representation of the evolution of growing islands is given by kinetic rate equations [21, 50], which describe the process in terms of the time dependent density functions. For example, the rate of change of the surface density of adatoms can be expressed by [4]:

$$\dot{N}_1 = R - \frac{N_1}{\tau_s} - K_1 N_1^2 - N_1 \sum_{i=2}^{i_{\max}} K_i N_i \quad , \quad 2.5$$

where K_i are temperature-dependent kinetic constants and terms with K_i describe the decrease of the number of adatoms by forming clusters; N_1/τ_s is the rate of adatom desorption. For clusters consisting of i atoms, a rate equation is:

$$\dot{N}_i = K_{1-i} N_1 N_{i-1} - K_i N_1 N_i \quad , \quad 2.6$$

The solution predicts that the number of clusters $N(t)$ increases almost linearly with time at the early stage, after which it saturates at a certain time depending on deposition rate and substrate temperature. $N(t)$ decreases with further deposition due to coarsening and coalescence. Fig. 2.5 illustrates this.

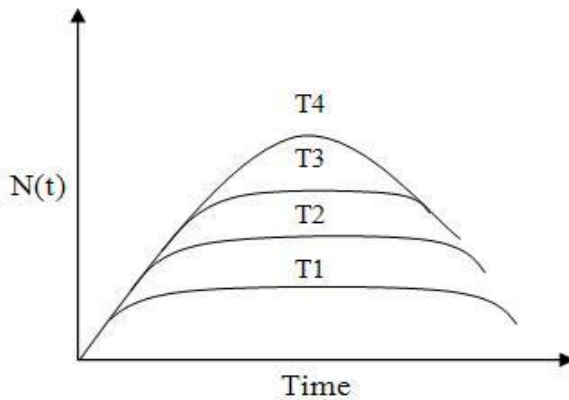


Figure 2.5. Schematic dependence of $N(t)$ with time and substrate temperature $T_1 > T_2 > T_3 > T_4$ [4].

At steady state conditions when $\frac{dN}{dt} \approx 0$, the rate equations can be solved analytically. The corresponding solutions, known as the scaling laws, relate the number density of stable nuclei with the various process and material parameters, as has been addressed in detail by Venables and coworkers [8, 21, 50, 51]. Thus, the density of stable islands N in a steady state condition can be expressed by [21, 50-52]:

$$N = An_0 \left(\frac{R}{\nu} \right)^p \exp \left(- \frac{E_{tot}}{kT} \right), \quad 2.7$$

A is a dimensionless constant, n_0 is the density of adsorption sites at the surface, R is the deposition rate, ν is the fundamental frequency, T is temperature, E_{tot} is the activation energy, and the power p is a parameter depending on the critical nuclei size i . Under steady state conditions, the generic expression for the value of “ p ” in 2D islands is [50, 51]:

$$p = \left(\frac{i}{i+2} \right), \quad 2.8$$

and for 3D islands [50, 51],

$$p = \left(\frac{i}{i+2.5} \right). \quad 2.9$$

Experiments for Ag deposition on Pt (111) showed that $p=0.32 \pm 0.05$ at $T=90^\circ K$ and $4 \times 10^{-5} \leq R < 8 \times 10^{-3}$ ML/s. The results are consistent with the theoretical predictions for p value of 0.33 [53].

An estimate for the average distance between the islands (δ) derived from the scaling law indicates that the average distance and deposition rate are related by

$$\delta \propto 1/R^{p/2}, \quad 2.10$$

whereas the density of clusters a power law related to the deposition flux i.e.

$$N \propto R^p. \quad 2.11$$

When island coarsening takes place, the average distance δ increases with time t .

In general, the average distance follows a power law with the exponent m depending on the coarsening mechanism [54-60]:

$$\delta(t) \propto t^m. \quad 2.12$$

In several papers, the power $m = 1/4$ was derived by solving a continuity equation describing a capillary-force induced island coalescence [59, 60]. The powers p and m in Eqs.(2.7-2.12) may, however, depend on critical nucleation size and temperature.

A widely used approach is to apply the rate equation in the form of the Arrhenius plot of N as a function of the inverse of T . In Fig. 2.6, the example of Ag/Pt (111) deposition characteristic is shown. A linear fit in the anticipated $i = 1$ regime and the dashed line for $i=2$ show different slopes indicating the existence of two activation energies [53]. At very low temperature, thermally activated bond dissociation is infrequent; all adatom clusters including dimers are stable and a single adatom can be considered as a critical nuclei, which corresponds to the estimate $i=1$. Higher temperature regimes are represented by $i=2$, and the transition between the two occurs at $T=110\text{K}$. The island density is low and subject to large statistical errors; however the Arrhenius dependence is expected to be followed.

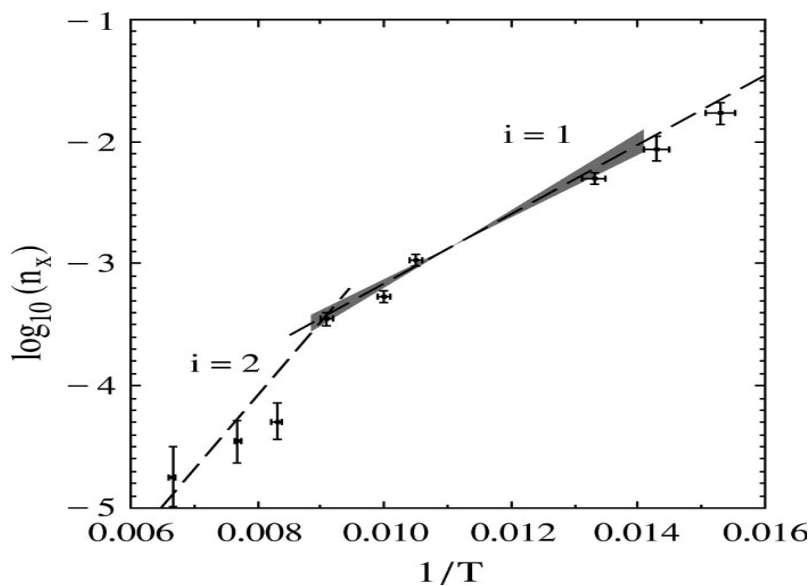


Figure 2.6. Arrhenius plot of saturation island densities measured at $R=0.12$ ML for Ag/Pt (111) [53]. The values i indicate the anticipated critical nucleation size. (Reprinted with the permission of American Physical Society.)

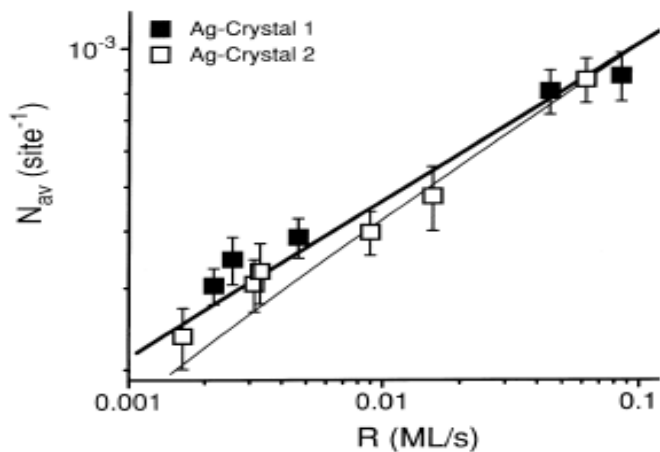


Figure 2.7. Scaling of N_{av} with R at 295 K. Open and solid symbols are experimental data taken on two different Ag(100) substrates [31]. (Reprinted with the permission of Elsevier)

Fig 2.7 shows the relationship of deposition rate to the cluster density. At low deposition rate, atoms can diffuse farther before they are trapped in stable positions. An increase in deposition rate results in more numerous, smaller islands, and the number of islands per unit area increases accordingly. To produce large crystallites or even monocrystals with fewer islands per unit area, the substrate temperature should be high and deposition rate should be low. Conversely, low substrate temperature and high deposition rates yield a large number of smaller islands [4] which is more relevant for NC production.

To conclude, scaling laws are used extensively to interpret experimental data and guide process development. Keeping all other conditions constant, the effect of one process parameter such as the deposition time (t), deposition rate (R) or temperature (T) can be observed. Such simple dependencies have proven to work well at relatively early stages of deposition. However, the detailed morphologies that develop at later stages of the process, when the nuclei grow into nanocrystalline islands, cannot be described by the density and/or the average distance of nuclei of alone, and demand a more thorough investigation of the morphologies as functions of multiple process parameters such as the deposition time [34, 61][34, 61] and deposition rate [31, 55, 62, 63], crystalline orientation [64], material [31, 54, 65] and temperature [32, 57, 64, 66-68] of the substrate. Understanding of the synergy of these factors and their impact on the morphology is still incomplete and beyond the capabilities of simple kinetic theories and scaling laws. The scaling laws have proven to describe well the density of stable

nuclei at early stages of deposition. Of major interest for applications, however, are detailed morphologies that develop at later stages of the process, when the nuclei grow into nanocrystalline islands still not complete. More comprehensive simulation methods are required to realize rational in-silico aided design of nanofabrication processes.

2.4 Modeling and Simulation

Many applications require fine control of film structure at the nanometer scale. Such control is enabled by insight from more comprehensive theoretical tools. In particular, detailed numerical modeling of self-assembled synthesis of NCs is a subject of constantly growing interest. Theoretical and simulation studies of film growth employ a broad variety of approaches. The popular approaches include Molecular Dynamics (MD) simulation [5, 7], Kinetic Monte Carlo (KMC) simulation [8-14, 61, 69, 70], and analytic coarse-grained theories[71, 72]. The performance of these simulation techniques depends on the size, time scale, and details of the process to be studied.

2.4.1 MD modeling

In the Molecular Dynamics method [5-7, 73-75], one begins with defining the interaction potentials between the individual particles for which the detailed dynamics will be followed. The geometry and boundary conditions are specified and initial coordinates and velocities are assigned to each atom or molecule. Then,

the equations of motion for the particles are integrated numerically, stepping forward in time by discrete steps of size Δt . Quantities such as forces, velocities, and positions are calculated as a function of time to determine their evolving values and dynamic fluctuations. When designing a simulation tool, care must be taken to choose interaction potentials and ensembles that capture the essential physics that is to be addressed. The amount of computational effort typically grows linearly with both the number of particles, and the number of time-steps. At least 20-30 parameters need to be handled to describe the motion of a particle. With current computers, typical size of box length is less than 100 nm, time is in nanosecond regimes and the number of atoms that can be handled is up to 10^5 . Although, extremely useful conventional MD is only possible on time-scales many orders of magnitude shorter than that of the deposition. Use of artificially large deposition rates could be a solution but those corrupt the description of the deposition process

2.4.2 KMC modeling

Molecular dynamics simulations provide a superb detailed description of elementary atomic processes at surfaces; however, the length and time regimes at which MD is efficient are still very limited. For this reason, KMC simulations are often considered an optimum compromise for their combination of efficient computation and atomistic-level detail [76]. KMC simulations have emerged as one of the fundamental tools for studying the growth of thin films and help to illustrate the physics of the growth process. KMC is distinguished from

molecular dynamics by employing statistically representative atomic moves instead of following the entire trajectories. This method mimics the atomic jumps randomly over a discrete lattice.

KMC favourably combines flexibility, predictive power, and numerical efficiency, and as such is very well suited for both basic understanding of NC growth and applications for in-silico aided design of nanofabrication processes. For this reason, KMC simulations have been widely used to study nanocrystalline growth. KMC models can be categorized into several groups, including specific event KMC [69, 70], bond counting KMC [8-14], and complete table KMC [61]. Out of these, the bond counting method is perhaps the most widely used in relation to film deposition modeling. Advantages of this approach involve a reliable assessment of the ground state of the adatoms, as well as an explicit accounting for the change in the total bond energy when the number of neighbours changes [70]. Particularly popular and efficient are solid-on-solid (SOS) models, where voids and overhangs are neglected [73].

Because of the efficient algorithm, KMC is a suitable method for modeling of NC synthesis. However, most published works reporting KMC modeling address the nucleation regimes that are also accessible to treatment by analytic nucleation theories [8, 9, 11, 12, 14, 69]. A few papers compare KMC modeling directly with similar experimental results [10, 70]. KMC studies pursuing a focused goal of

describing the effect of major process control parameters of PVD-based self-assembling synthesis of NCs are quite rare. Accordingly, understanding the impact of the synergy of the deposition conditions on the growing morphology is still incomplete. With the advancement of nanotechnology, there is a demand to guide process engineers for a more detailed description of the self-assembling nanostructures, especially grain size, grain shape, grain orientation, and texture.

2.4.3 Continuum kinetic modeling

Although very efficient, even KMC is not always able to handle practical size and time regimes, which in the case of PVD often reach the scales of more than 10^9 atoms and last from minutes to hours. In practical regimes of film deposition, analytic coarse-grained models [71-73, 77-79] are the most efficient. In continuum theory, one needs to solve kinetic equations such as the rate equations for submonolayers [80], and for the morphology on rough surfaces [79], often employing various finite-element models [72, 77, 78], etc. To formulate those models, one needs to know the details of atomic interactions at surfaces. Then, it is possible to solve the kinetic equations if relevant kinetic parameters as well as the equilibrium structures are known. Due to its scale independence, the system size and time are virtually unlimited for the continuum theory; however, the parameterization often must be supplied by other studies. The main disadvantage of continuum models is the context of NC production is the disconnection between the representation and nanoscale phenomena.

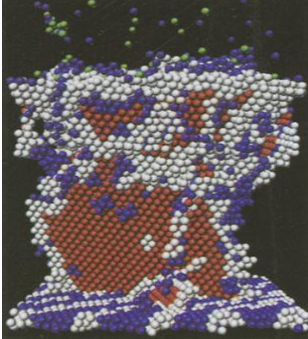
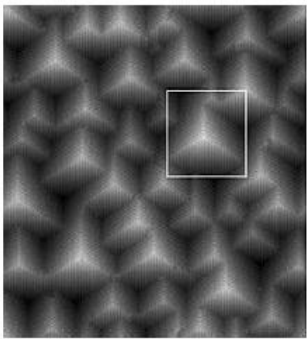
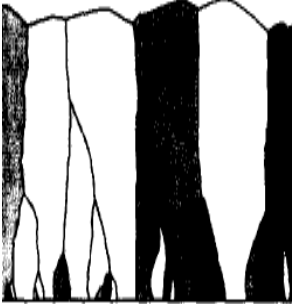
	MD modeling	KMC modeling	Continuum kinetic modeling
1	 <p>Example [81]</p>	 <p>Example [82]</p>	 <p>Example [72]</p>
2	System size less than 100 nm.	The system size less than 1 μm ,	Model size is virtually unlimited.
3	Simulation time in nanosecond regimes.	Simulation time in minutes regimes.	May handle times from minutes to hours.
4	Number of atoms below 10^5 .	Number of atoms below 10^7 .	Number of atoms is also unlimited

Table 2-1. Comparison of modeling techniques. (Reprinted with the permission of Elsevier and Springer)

2.4.4 The integrated multiscale scheme

Modern approaches tend to combine the various scale modeling tools into one hybrid scheme. In this method, often MD techniques may be used at the initial stage for atomic level simulations which define the basic parameters and then KMC may be applied to model NCs with the help of the defined binding energies, diffusivities and other relevant parameters. Then a continuum theory can be set up

to simulate the large scale growth. Hybrid multiscale models are reported increasingly often [74, 83-90]. Methods of coupling the various levels are intensely addressed [73, 83, 87, 91]. Thus, the emerging trend in process simulation is a hierarchical multiscale approach that combines several coupled models, each responsible for a particular length and time scale.

2.5 Summary and KMC Implementation Approach

The analytical scaling laws have proven to describe well the density of stable nuclei at early stages of deposition. However, the major interest for applications is presented by detailed morphologies that develop at later stages of the process, when the nuclei grow into nanocrystalline islands. The experimental morphologies shown in the Fig. 1.3 and Fig. 1.4 of the first chapter also demonstrate that the shape of deposited metallic islands depends on the substrate. It is clear that such differences cannot be captured by the density and/or the average size of islands provided by the scaling laws, and requires a more detailed consideration. With continuing deposition, the bases of the islands start merging and the pattern evolves into a continuous thin film. These late stages of nucleation also require appropriate simulation approaches capable to account for the changing surface morphology.

In the existing modeling and simulation approaches, KMC has emerged as a suitable method favourably combining atomic-level detail and numerical efficiency. In this work, I implement two KMC modeling techniques for describing NC synthesis, a lattice based model and an off-lattice model. For the

first technique, I further considered 2D and 3D versions. In chapter 3, I discuss the lattice based 2D model and its results; and in chapter 4, I present the lattice based 3D model. In chapter 5, I outline the influence of defects on the results of both 2D and 3D lattice models. In chapter 6, I introduce a new Off-Lattice based modeling technique. Chapter 7 summarizes the results of the thesis and outlines possible future directions of research.

CHAPTER: THREE

3 LATTICE BASED 2D MODEL

In this chapter, I present the development of a 2D lattice based KMC model where the main focus is the submonolayer deposition phenomena at the early stage of NC formation. I compare numeric results with the experiments available in the literature and demonstrate that my 2D model can be a useful tool for process engineers to simulate desired NC fabrication and predict the outcomes.

3.1 The Model Description

In this chapter, the film deposition-diffusion process of Cu and Ag NCs is represented by two simple square lattice models describing the lateral interaction between adatoms. Model 1 with eight neighbouring sites for each atom is simply the primitive square lattice and Model 2 with four neighbors in an alternating formation represents the (100) FCC lattice. The symmetry of the growing metal clusters depends on the type of lattice structure used in the model [92]. Fig. 3.1 shows the structure for both models. Simulations were performed for an area $L \times L=400 \times 400$ cells for Model 1 and 566×566 cells for Model 2. I assume the diameter of an atom equal to 0.25 nm making the simulated region size equal to 100 nm . In this chapter only 2D projections of the morphologies are considered.

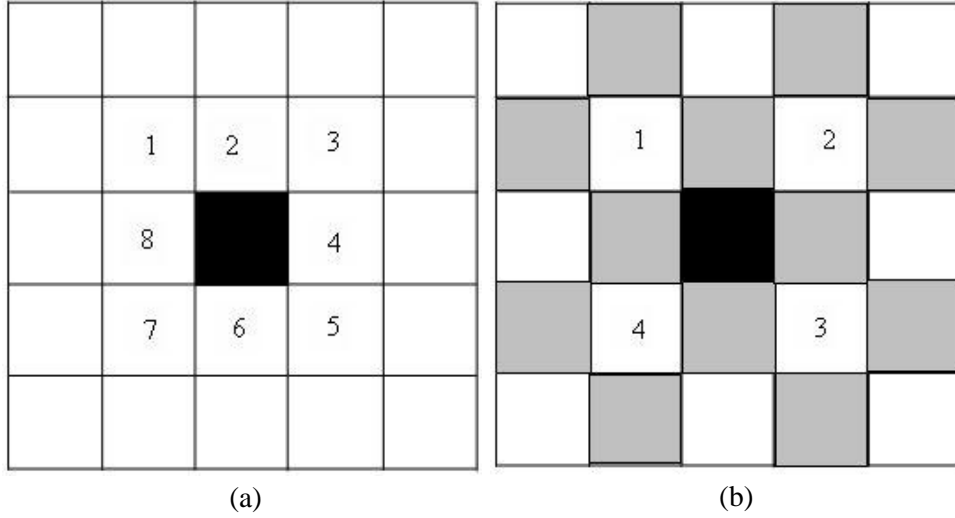


Figure 3.1. Two models for the lateral interaction of adatoms: (a) Model 1, primitive square lattice and (b) Model 2, FCC lattice. The black rectangles indicate the adatom and the numbers indicate the allowed positions to which it can jump.

The deposition and diffusion processes are described by the numbers of corresponding Monte-Carlo steps, N_{dep} and N_{diff} . Sites for both deposition and diffusion Monte-Carlo steps are selected at random locations in the 2D array, in such a way that individual deposition and diffusion events are not correlated. For a given period of time t , the number of attempted Monte-Carlo deposition and diffusion steps is determined by

$$N_{dep} = t R , \tag{3.1}$$

and

$$N_{diff} = t D_{adatom} / d^2 , \tag{3.2}$$

respectively, where R is the deposition rate in monolayers (ML) per second, and D_{adatom} is the surface diffusivity of adatoms. The adatom diffusivity can be represented by

$$D_{adatom} = D_0 \exp\left(-\frac{E}{kT}\right), \quad 3.3$$

Here D_0 is the pre-exponential factor, T is temperature, and E is the activation energy of adatom diffusion in the absence of lateral bonding with other adatoms. The latter is considered to be equal to 0.46 eV for Cu and 0.38 eV for Ag [20, 31].

At each Monte-Carlo deposition step, a randomly selected cell in the 2D array is selected. In the present 2D simulation, the deposition of an atom occurs at the condition that the selected cell is empty. At each Monte-Carlo diffusion step, two nearest-neighbor cells “a” and “b” are also selected randomly considering 8 nearest-neighbors for Model 1 and 4 neighbors for Model 2. Next, the probability P_{a-b} of jump from position “a” to position “b” is computed through the Metropolis algorithm with the energy function F depending on the number of lateral bonds n in positions “a” and “b” in such a way that $F = -\gamma n$, for $n > n_c$ and $F = 0$ for $n < n_c$, where n_c represents the number of bonds for a critical nuclei, adopted to be 3 for Model 1 and 2 for Model 2. The corresponding probability of an adatom’s jump from position “a” to position “b” is

$$P_{a-b} = \min\left(1, \exp\left(-\frac{\gamma(n_b - 1 - n_a)}{kT}\right)\right), \quad 3.4$$

where y is the energy of lateral bonds between adatoms, $n_{a,b}$ are the numbers of lateral bonds at neighboring locations “a” and “b”, respectively, The energy of lateral bonds between adatoms, y , was derived from the cohesive energies for Cu (3.52 eV) and for Ag (2.95 eV) [93].

Cohesive energy provides a reasonable approximation and is often used for calculating the bond breaking energy [94-96]. Accordingly, for Cu in Model 1, an atom has 8 lateral neighbors and 9 neighbors below on the substrate, so the total number of neighbor atoms is 17. Model 2 adopts 4 lateral neighbors and 5 effective bonds with the substrate. Thus the estimate of lateral bonding based on the measured cohesive energy for Cu provides the energy per bond of approximately 0.20 eV for Model 1, and 0.39 eV for Model 2. For Ag the values are 0.17 and 0.32 eV, respectively. The probability P given by Eq.3.4 is equal to 1 for jumps resulting in an increasing number of bonds, and is less than 1 otherwise.

Periodic boundary conditions are applied in the 2D model for both “x” and “y” directions. When an atom reaches the last position on an axis it automatically considers the site located at the other end of the axis among its nearest neighbours within the frame of operation to ensure that the crystal straddling the boundary continues to grow.

3.2 Simulation Process

The entire process of simultaneous deposition-diffusion is repeated for a number of time cycles, each describing a brief time interval, typically one second. Time in the simulation is scaled according to the number of deposition steps as well as the deposition rate that has been assigned to the system. For a given deposition rate, the number of attempted deposition steps N_{dep} is determined by the deposition time (see Eq.3.1), whereas the number of attempted diffusion steps N_{diff} depends on both time and temperature according to Eq.3.2 and Eq.3.3. The number of executed diffusion steps includes a further temperature dependence as described by Eq.3.4. This framework allows us to study the impact of the deposition rate, time, and temperature, as independent factors, on the plan-view surface morphology. For convenience, a kinetic parameter K is employed, which characterizes the relative influence of the number of attempted deposition and diffusion steps on simulation of the growth process. The value of K is given by the ratio of deposition and diffusion steps in the simulation,

$$K = \frac{N_{dep}}{N_{diff}}. \quad 3.5$$

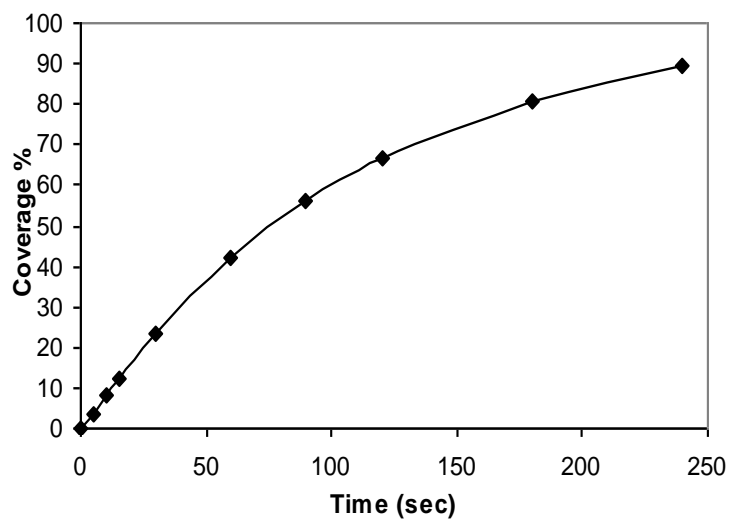
This definition is comparable to the so-called lumped parameter employed in the analytic scaling laws [8, 53, 97], which facilitates interpretation of some of the results of the simulation and comparisons with the analytical theory.

3.3 Results and Discussion

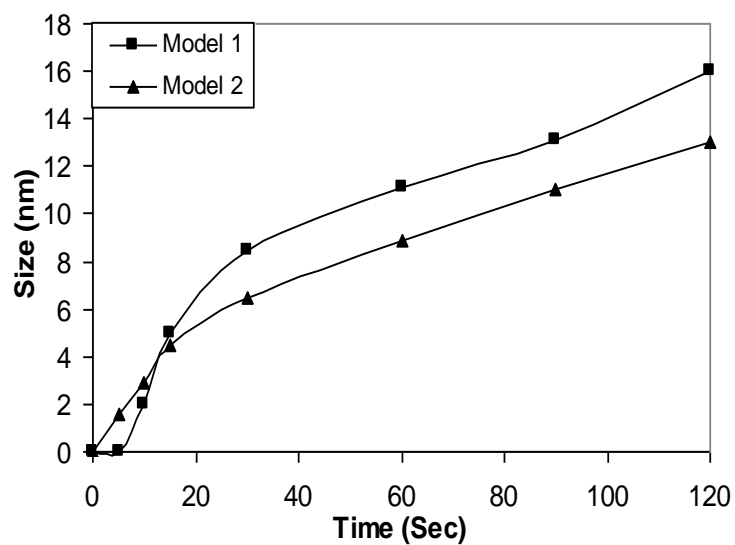
Presented below are the results of KMC simulation of the PVD deposition of metal clusters on the two model symmetries of the lateral interactions, and a study of the resulting nucleation and coarsening behavior. The variables include deposition rate, duration, and temperature. Outcomes of the simulation include the average size of metal islands and their 2D shape in the plane of the substrate. The size of the islands is defined by their average diameter, calculated as four times the total area of islands divided by their total perimeter. It is a valid approach as long as applied to regimes where the islands adopt nearly circular or nearly rectangular shapes. As it follows from published experiments and is also confirmed by modeling below, most self-assembled islands have such regular shapes in the broad range of surface coverage, so that this evaluation of the island size is fairly reliable. When counting the number of islands in smaller region, as a result of the periodic boundary conditions, broken islands might contribute larger values for the number of islands per square centimetre. For simplicity I converted the fraction into nearest integer values. The average island size is not expected to have much effect on the periodic boundary conditions. The densities of nanoislands generated have also been analyzed. The results are described below.

3.3.1 Time evolution of the surface morphology for two model substrates

Fig.3.2(a) shows the percentage of surface coverage by adatoms (Ag) and islands, which was determined by dividing the total number of deposited atoms by the total number of sites available in the system, as a function of deposition time.



(a)



(b)

Figure 3.2. Percentage of substrate coverage (a) and island size (b) as functions of time. Simulations correspond to Ag deposition at $T= 300\text{ K}$ and $R=0.0093\text{ ML/sec}$.

As can be seen in the experimental data of Fig. 1.3, at constant rate and temperature, island size increases with time, and if the deposition continues, the islands start merging. In the present model, obviously, the surface coverage increases with the time of deposition. In Fig. 3.2(b), the average size of Ag clusters is shown as a function of deposition time for the two models of lateral interactions. Similar to the Fig. 1.3, Fig. 3.3 and Fig. 3.4 demonstrate the corresponding evolution of the morphologies. In both models, the size of clusters increases with time. At the room temperature regimes considered in this example, growth occurs mainly because of arrival of deposited atoms at the surface, as well as by coalescence (merging of clusters).

Another mechanism that may contribute to a cluster's growth, primarily at increased temperatures, is the Ostwald ripening (growth of larger clusters at the expense of smaller ones). Gradually, the growing islands coalesce into a continuous thin film. According to the results presented, this occurs in about 4 minutes of deposition when the coverage reaches approximately 90 %.

As can be seen in Fig. 3.2(b), the islands increase in size quickly over the initial period of deposition (approximately 20-30 sec.), after which the growth slows down. The crossover occurs when the average inter-island distance becomes less than the effective diffusion length of adatoms, i.e. the condition at which neighbor islands start competing for capturing newly arrived adatoms. The regimes of

slower growth corresponds the best to the conditions of applicability of the analytical scaling law and its derivatives described in chapter two.

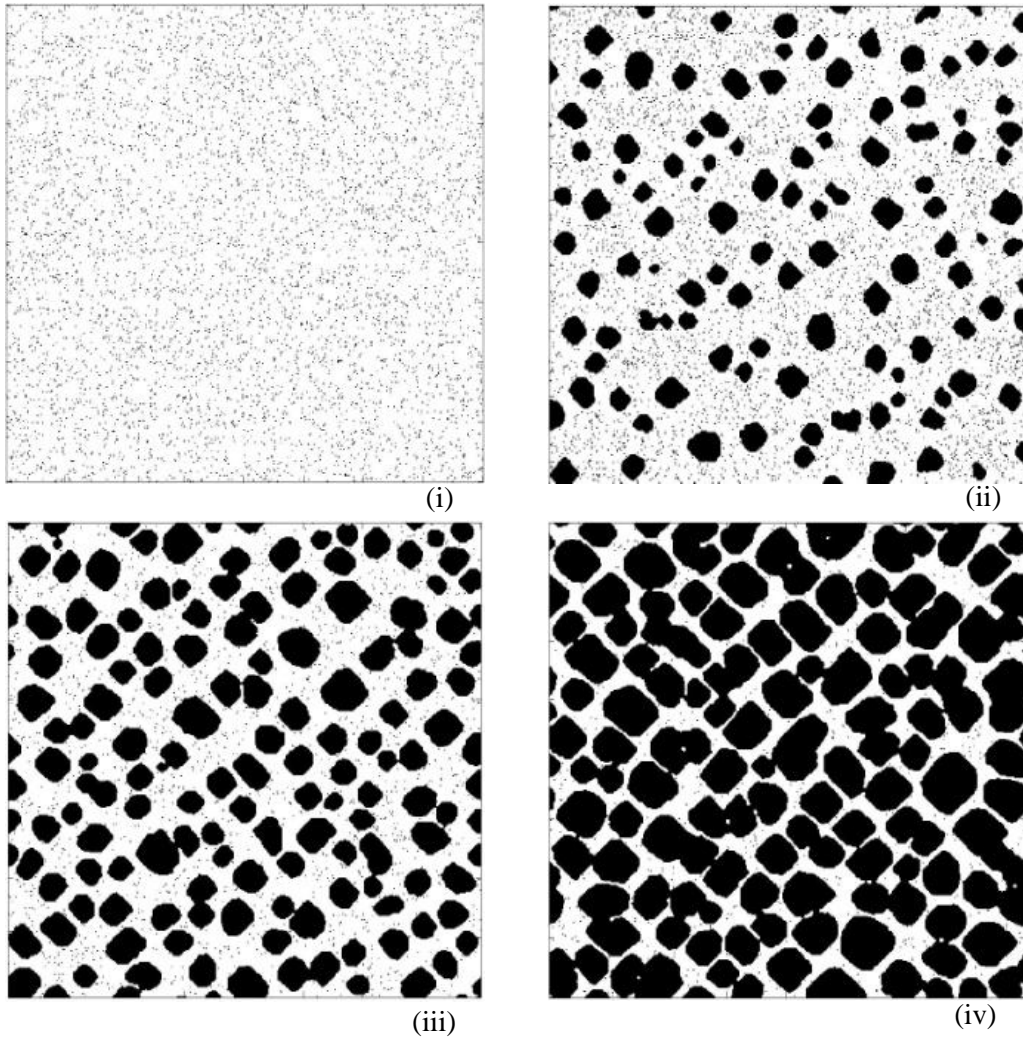


Figure 3.3. Simulated surface morphologies demonstrating Ag islands' growth for deposition times of (i) 5 sec, (ii) 30 sec, (iii) 1 minute and (iv) 2 minutes for Model-1 at $T= 300$ K and $R=0.0093$ ML/sec.

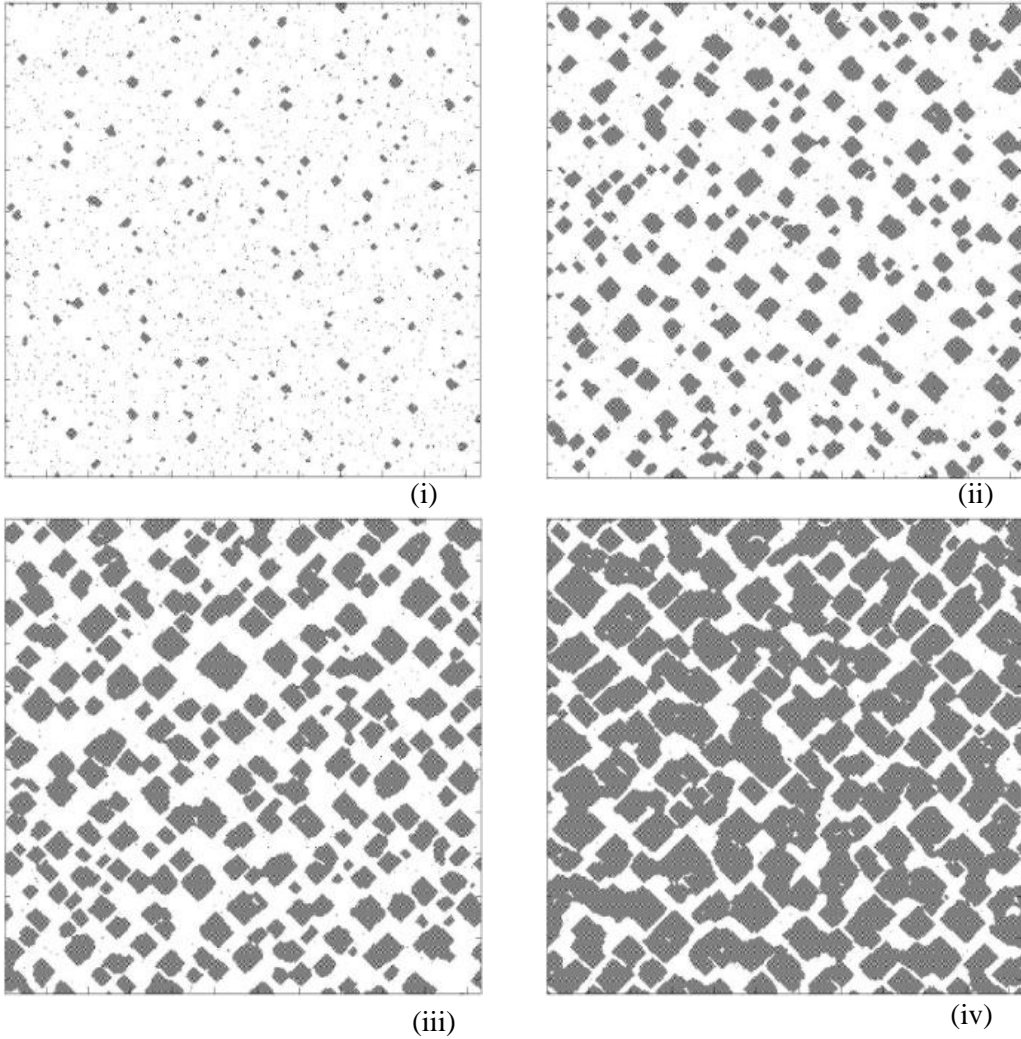


Figure 3.4. Simulated surface morphologies demonstrating Ag islands' growth for deposition times of (i) 5 sec, (ii) 30 sec, (iii) 1 minute and (iv) 2 minutes for Model-2 at $T= 300$ K and $R=0.0093$ ML/sec.

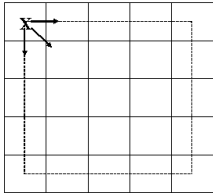
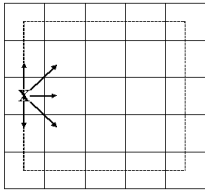
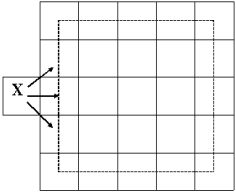
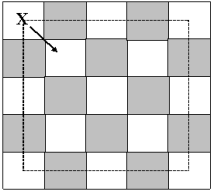
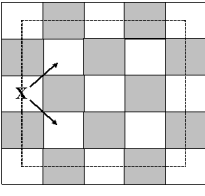
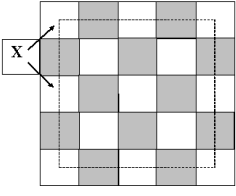
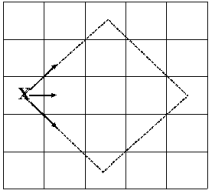
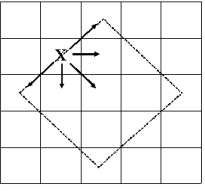
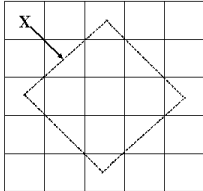
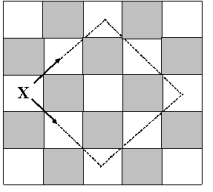
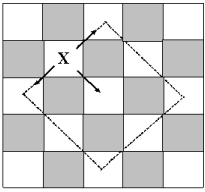
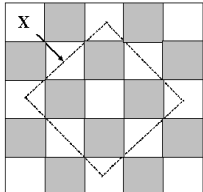
The comparative growth processes of the two models are shown in Fig. 3.3 and Fig. 3.4, and demonstrate that nano-islands corresponding to these models largely show a similar behavior. A difference seen in these figures is that with Model 2,

islands nucleate at an earlier stage of deposition compared to Model 1. This can be explained by the higher activation energy for adatom diffusion in Model 2.

Another notable point is the difference in shapes of the clusters with the two models, which is clearly seen in Fig. 3.4. Thus Model 2, which corresponds to FCC symmetry, leads to rectangular islands as expected for crystalline substrates, whereas Model 1 produces softer morphologies with more rounded corners, reminiscent of deposition onto non-crystalline materials such as glass. Remarkably, the experimentally observed clusters grown on crystalline substrates and glass (see Figs. 1.3 and 1.4) show similar morphologic trends to those obtained numerically. This similarity of the simulated and experimental morphologies is observed both at early sub-monolayer stages of deposition and for developed coverage, when the deposited structures may contain more than one monolayer of atoms. This confirms that the present 2D model is representative of both the submonolayer regimes of deposition as well as of its later stages.

From Fig. 3.3 and Fig. 3.4, it is evident that for both substrate geometries, the islands' facets adopt a preferential "diagonal" orientation with respect to the main crystallographic orientations at the surface. In order to understand the origin of this texture, relevant locations of adatoms either at a corner or at a side of an island were considered for both substrate symmetries, as illustrated by Tab.3.1.

Table 3-1. Geometries and numbers of neighbor atoms for 6 characteristic adatom locations in Model 1 and Model 2. Solid arrows show the bonds. Dashed lines indicate boundaries of hypothetical islands.

	Case1: Straight Corner	Case2: Straight Side	Case3: Straight Terrace
Model 1	 $m_1=3$	 $m_2=5 (>n_c)$	 $m_3=3$
Model 2	 $m_1=1$	 $m_2=2$	 $m_3=2$
	Case4: Diagonal Corner	Case5: Diagonal Side	Case6: Diagonal Terrace
Model 1	 $m_4=3$	 $m_5=5 (>n_c)$	 $m_6=1$
Model 2	 $m_4=2$	 $m_5=3 (>n_c)$	 $m_6=1$

Six typical adatom locations were identified marked by “x” in the table. For each typical adatom location, the number of bonds was determined with its neighbors, m , and compared it with the critical nucleation bond number n_c . If the number of neighbors m is equal or more than n_c , the atom is considered stable in that location.

In Model 1 and case 1, the adatom located at the corner of a straight island is bonded to 3 neighbors. In case 2, the atom located at the side of a straight island has 5 bonds. In case 3, the terrace adatom near the straight island has 3 bonds. In cases 4, 5, and 6, the atoms located in the corner, at the side, and near a terrace of a diagonal island have 3, 5, and 1 bonds, respectively. The number of bonds available defines the stability of the atom in that location. For Model 1, the critical bond number (n_c) is equal to 3 (See sect.3.1). Thus, an atom that has 3 or less neighbors is considered to be in unstable position. In cases 1 and 4, the corner atom has 3 bonds and is also unstable. However, in cases 2 and 5, the side atom has 5 neighbors and is bonded firmly with the island. Comparing the side and corner adatom positions in both straight and diagonal islands, it appears that they are equivalent in terms of stability. However, a different behavior is observed in the cases of terrace adatoms. In case 3, the straight island terrace adatom has 3 bonds. In such a position adatom is marginally unstable, but the addition of only one more adatom would stabilize it. For case 6, a diagonal island terrace adatom has only 1 bond, which is an unstable position. As a result, the diagonal terrace is less likely to undergo distortions by attachment of adatoms than the straight

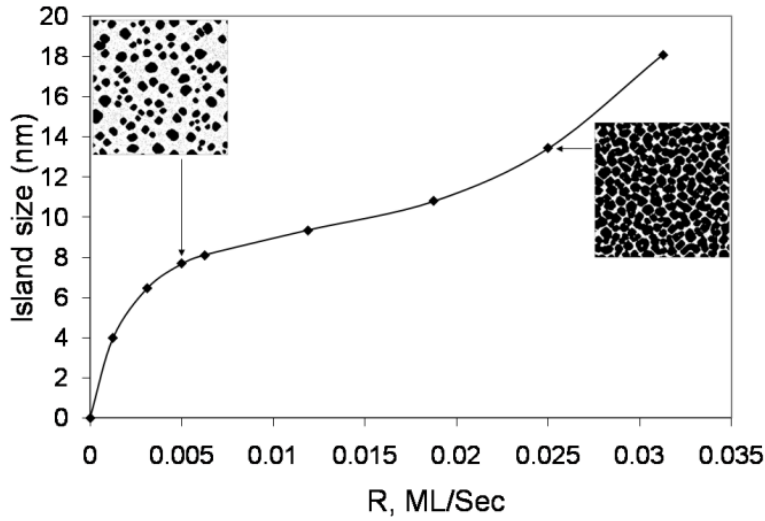
terrace. Because of this, a preferential diagonal orientation of the islands is observed, which show “rounded” corners formed by small segments of straight terraces. Similarly, one can analyze the typical positions of adatoms in Model 2. From the figures of Tab.3.1, it is evident that in distinction to Model 1, only locations at diagonal sides are stable, which naturally results in an even stronger preference of the diagonal texture than in Model 1.

One can conclude that Model 1 allows for growth in both straight and diagonal directions of the island’s boundaries, but the diagonal orientations are more immune to distortions than the straight ones, whereas in Model 2 only the diagonal direction is stable. Thus, the diagonal orientation is the preferred one in both models, as it can be seen in Fig. 3.3 and Fig3.4. However, since Model 1 allows the alignments in both directions, the corners of the growing islands are softer and round shaped. In contrast, Model 2 allows for the diagonal direction only, which explains why the corresponding islands seen in Fig. 3.4 are more uniformly shaped and corners of the islands are sharper than for Model 1 in Fig. 3.3.

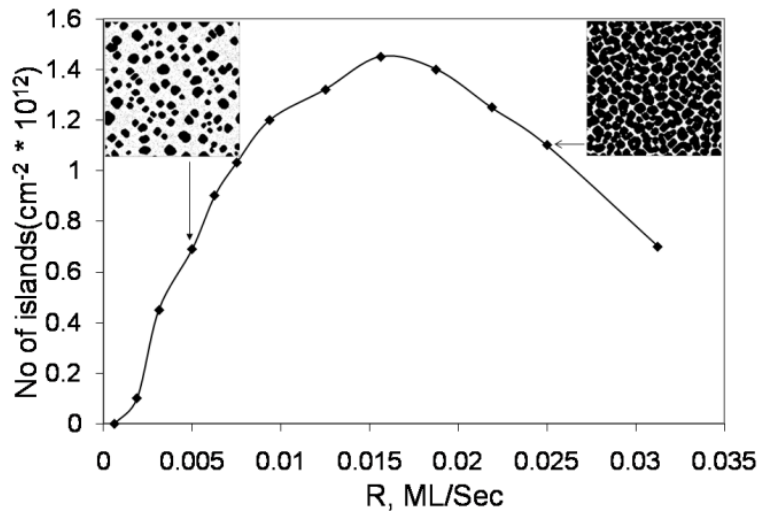
3.3.2 Effect of deposition rate

The effect of the deposition rate R has been studied under two representative conditions: constant deposition time and constant surface coverage which are illustrated by Figs.3.5-3.8. First, deposition during 1 min. is simulated with varying deposition rate (i.e. constant deposition time, see Fig. 3.5 and Fig. 3.7).

As follows from the figures, below the deposition rate of approximately 0.004 ML/s, the island sizes are very small (Fig. 3.5(a)) and few in number (Fig. 3.5(b)); however, both the island size and density increase steeply with R .

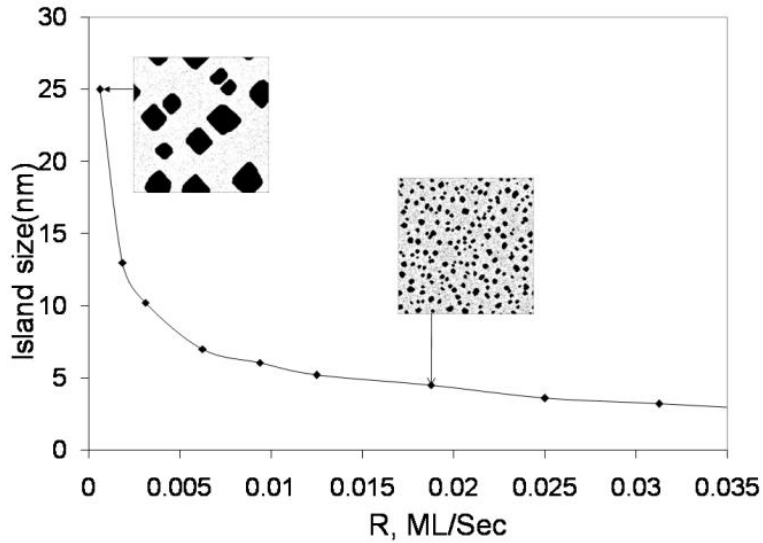


(a)

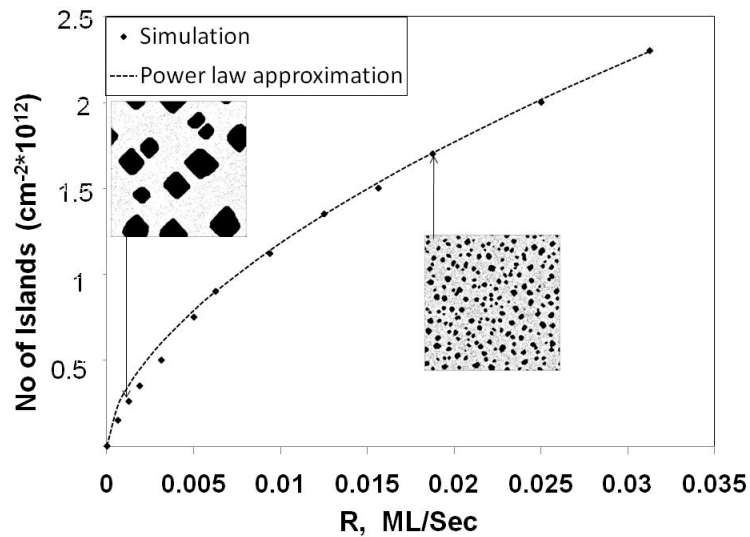


(b)

Figure 3.5. The average size (a) and density (b) of islands as functions of the deposition rate, with constant 1 min duration of deposition for Ag deposition using Model 1 at $T=300$ K.



(a)



(b)

Figure 3.6. The average size (a) and density (b) of islands as functions of the deposition rate, with constant 23% coverage, for Ag deposition using Model 1 at T=300 K. Also in (b) is a power law relationship for comparison.

When the rate increases beyond 0.005 ML/s, further change in size is minor, but the density of islands keeps increasing. However, when the deposition rate

increases above 0.02, the increase in island size with R is again considerable, and the density decreases sharply. The explanation is that at low deposition rate, the surface density of adatoms is also low. Formation of stable nuclei is a relatively rare event in these regimes, islands are sparse, and most of newly arrived adatoms are available for contributing to the growth of existing islands.

The size of islands is limited mostly by the availability of newly arrived adatoms, and increases in proportion to their supply. The plateau regime seen in Fig. 3.5(a) occurs at the conditions where newly formed stable islands start competing for adatoms with the existing ones. In this regime, the increasing density of islands (see Fig. 3.5(b)) becomes the limiting factor for their size, which stabilizes as Fig. 3.5(a) shows. This behavior is also illustrated by the morphologies shown in Fig. 3.7. At high deposition rates, when the surface coverage exceeds approximately 60%, the neighbor islands merge and a continuous thin film starts forming, as can be seen in Fig. 3.7(iv). This results to a decrease in the nominal island density (Fig.3.5(b)) and a pronounced increase in size (Fig.3.5(a)). Note, however, that the accuracy of the approach employed to evaluate the island size is limited in this regimes, and thus the increasing portion of the dependence in Fig. 3.5(a) for high deposition rates R is rather qualitative. However, the overall trends shown by Figs. 3.5(a,b) and Fig. 3.7 are representative and in line with the experiments on deposition of Ag on Ag (100) [16].

The effect of deposition rate while keeping constant the percentage of final surface coverage has also been studied (see Fig. 3.6 and Fig. 3.8). At very low deposition rate, only a few large islands are formed. As the deposition rate increased keeping the coverage fixed at the level of 23%, the island size decreases. Initially this change is dramatic, but later its effect is not as significant (Fig. 3.6(a)).

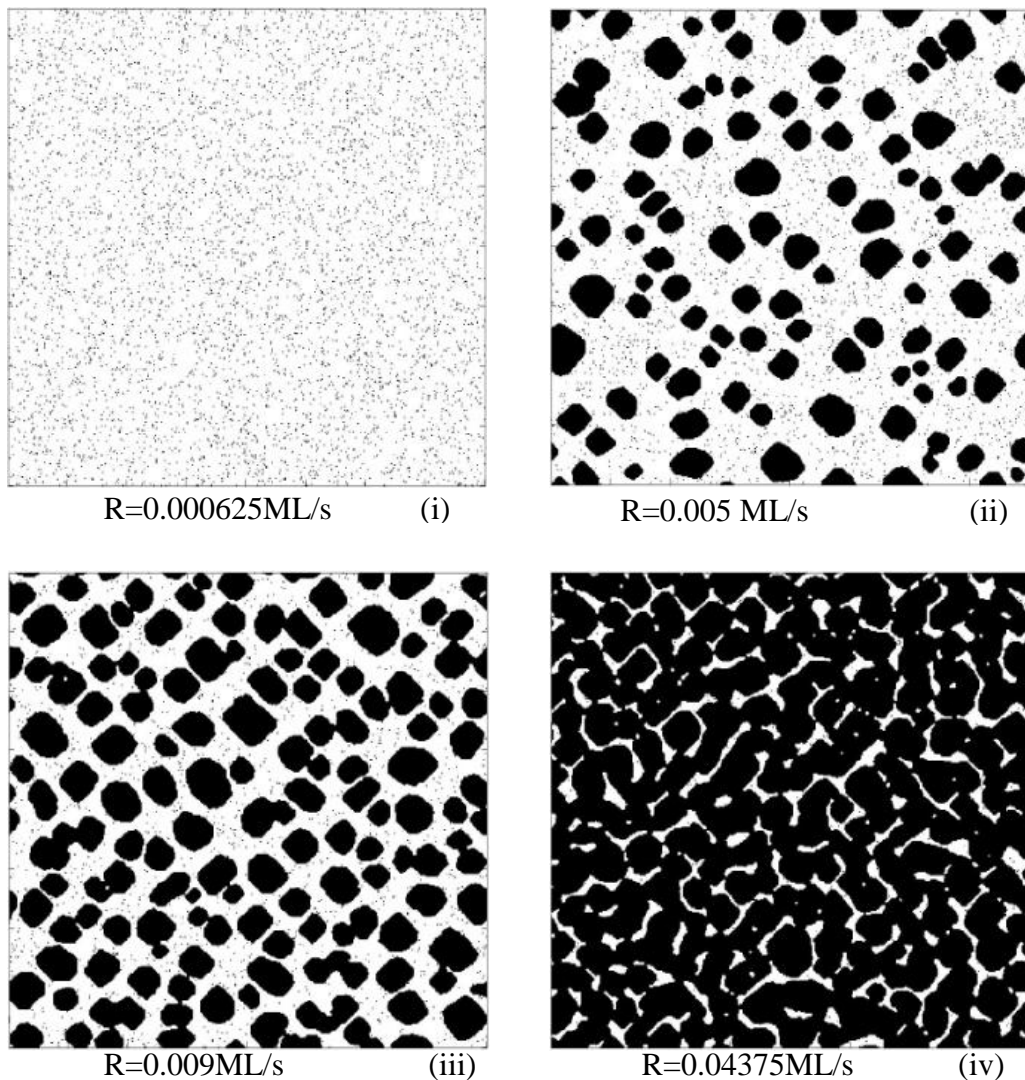


Figure 3.7. Simulated surface morphologies for Ag deposited at $T= 300\text{K}$ with varying deposition rates at constant duration of 1 min.

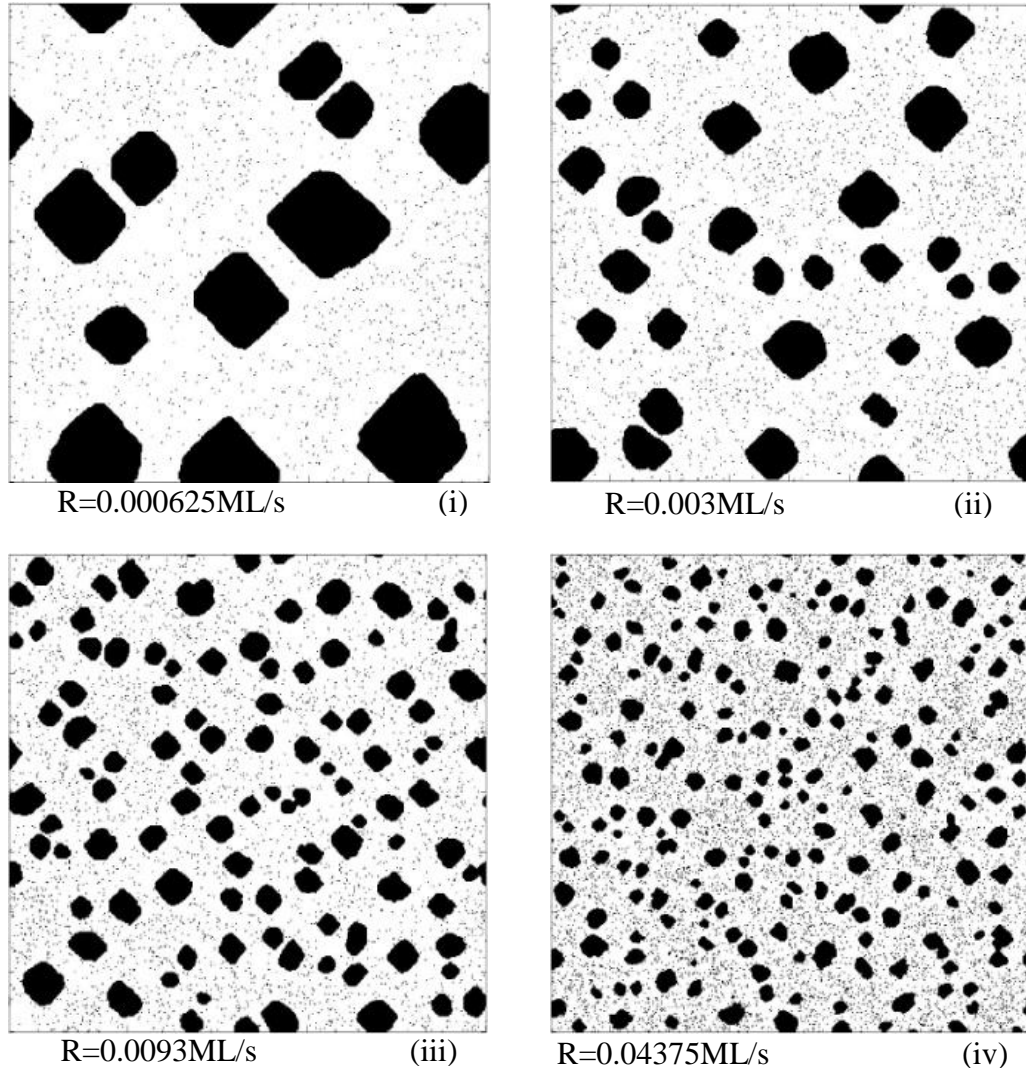


Figure 3.8. Simulated surface morphologies for Ag deposited at $T= 300\text{K}$ with varying deposition rates at constant coverage of 23%.

In contrast, the density of islands increases steadily with increasing R as demonstrated in Fig. 3.6(b) and Fig. 3.8. The last trend results from facilitated nucleation at higher deposition rates, which provides a larger number of stable nuclei per unit area. Concerning the decreasing dependence seen in Fig. 3.6(a), it may be explained by

the shorter deposition times required to deposit a particular surface coverage with increasing deposition rate. In this case, the island size is limited by the number of captured adatoms over the time required to reach a 23% surface coverage, which decreases with R .

Analysis of the dependence $N(R)$ in Fig. 3.6(b) shows that it is reasonably well described by the scaling law $N \sim R^{-0.583}$. Although the power of 0.583 is somewhat less than the asymptotic estimate of 0.67 that corresponds to the critical number of bonds adopted in this model, one can conclude that the density of islands can be described by the scaling law at the assumption that the surface coverage is kept constant at a relatively low value of 23%. In Fig. 3.6(b), the power law graph is shown along with results found from simulation which are very consistent. However, the scaling law is inapplicable to Fig. 3.5(b), which presents the dependence $N(R)$ at a constant time of deposition.

The conclusion is that variation of deposition rate is a powerful control factor by which process engineer can direct the process of NC growth. This process, however, depends over a number of other conditions, such as the time and coverage of the surface, whose impact should be accounted for properly. The well-known classical scaling laws, although very useful for understanding of basic physical trends, are not always flexible enough to capture efficiently all the diversity of deposition. This emphasizes the importance of efficient direct

simulations of the deposition process. In addition to more flexibility when describing the average characteristics such as the number of stable nuclei, KMC simulations also provide important information on the detailed morphology of the surface such as shown in Figs. 3.3, 3.4, 3.7 and 3.8, which is a mandatory component required for a detailed understanding of the trends of deposition.

3.3.3 Effect of the kinetic factor K

As the next step, the impact of the kinetic factor K is studied (see Eq.3.5) on the results of the simulations. It should be noted that K represents the numerical procedure rather than any PVD process control parameters, however, similar descriptors have been employed frequently as a convenient variable in scaling laws [8, 53, 97], and thus such an analysis would facilitate the comparison of numerical simulations with the analytic theory.

The graph in Fig. 3.9 shows the average island size as a function of K , for a constant surface coverage. The two dependencies seen in the figure correspond to varying the number of deposition steps (squares) and diffusion steps (triangles). Both dependencies are decreasing power-law functions of K . However, it is evident from the graph that the effect of deposition rate's change is more pronounced than the effect of diffusion change. The corresponding power laws are -0.54 and -0.31, respectively. This difference arises because of different duration of deposition in these two cases.

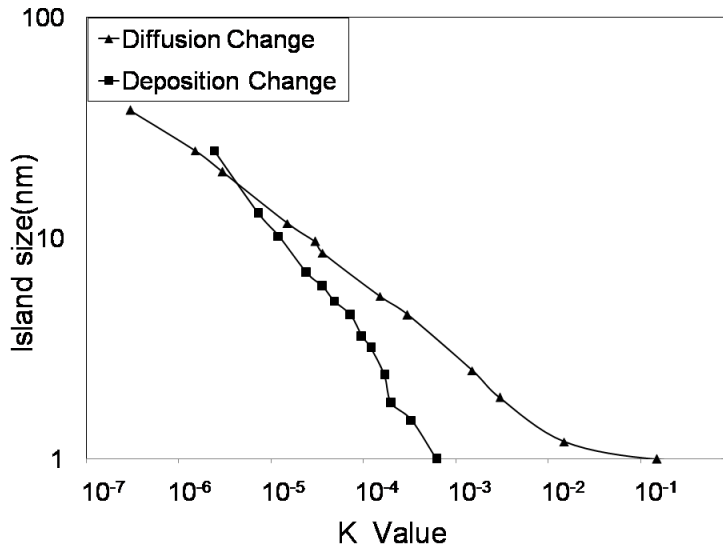


Figure 3.9. Average size of islands as a function of the kinetic parameter K , obtained by varying the number of diffusion steps at a constant 50% coverage (triangles), and by varying the number of deposition steps at a constant 23% coverage (squares), for 300 K deposition of Ag with Model 1.

Indeed, the results obtained by varying the number of diffusion steps (at constant coverage) correspond to the same deposition time of 1 min. In contrast, varying the number of deposition steps at a constant coverage results in a decrease of the duration of deposition in proportion to $1/K$. As demonstrated in Fig. 3.6(a), duration of deposition is an important factor limiting the island size, which results in the faster decrease of the size when the duration of deposition decreases. The point of intersection of the two dependencies in Fig. 3.9 corresponds to similar durations of deposition.

The overall power-law dependencies $\sim I/K^\gamma$ obtained are in agreement with the analytical scaling law [53, 97]. However, depending on whether the diffusion or deposition steps were varied *at a constant coverage*, the corresponding powers differ by more than 40%. This is another example demonstrating that caution is required when applying the basic scaling laws to analyze PVD processes, whose versatility should be accounted for carefully.

3.3.4. Effect of diffusivity and temperature

From PVD practice it is known that the islands' size and density are extremely sensitive to temperature [16, 64, 68, 98]. According to Eqs.3.2-3.4, in the model temperature determines the surface diffusivity through two terms: the number of diffusion steps N_{diff} representing the surface mobility of unbounded adatoms (Eq.3.2 and 3.3), and the probability P describing the interaction of adatoms with each other and stable islands (Eq.3.4).

Firstly, the number of diffusion steps alone has been varied, without considering the corresponding change of the probability P . Fig. 3.10 demonstrates how the change in the number of diffusion steps in the simulation affects the island size with fixed percentage of coverage.

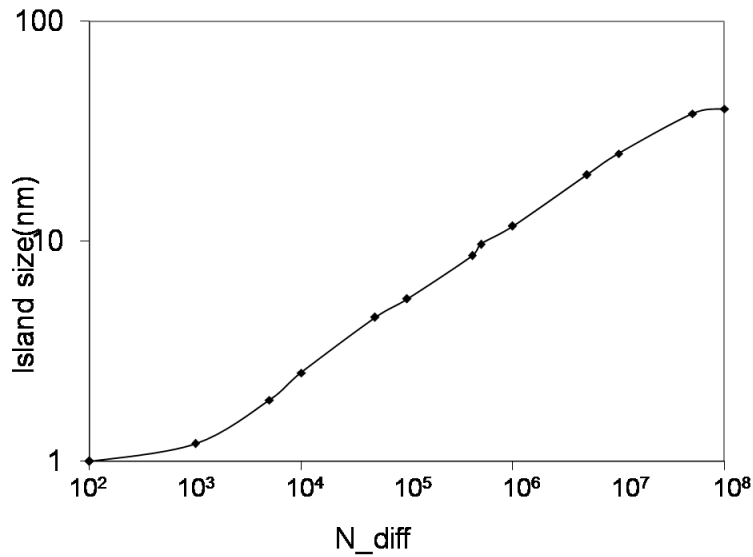
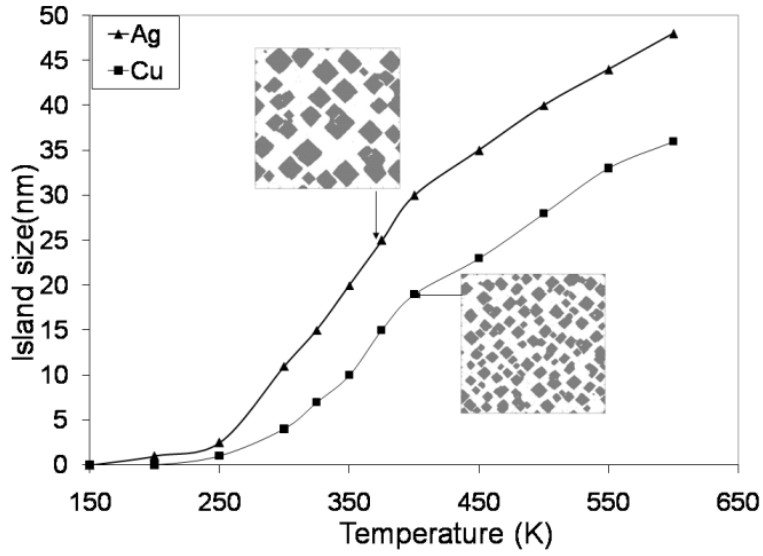
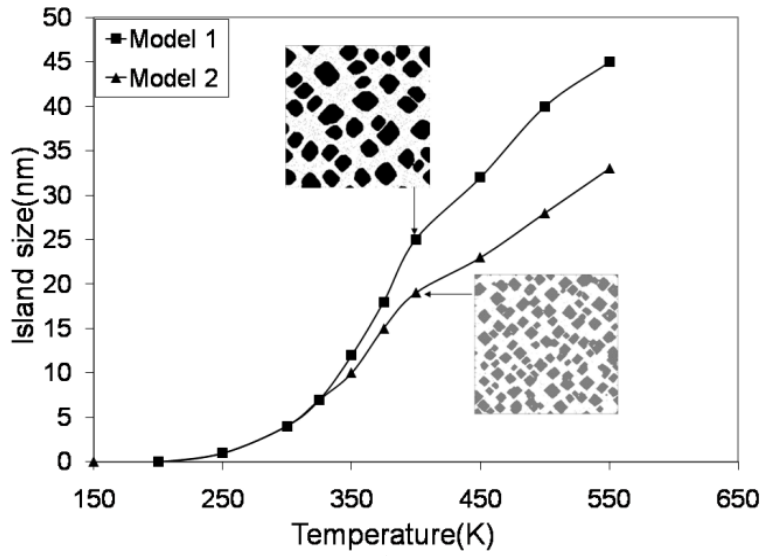


Figure 3.10. Average size of islands as a function of the number of diffusion steps N_{diff} (see Eq.3.3) at a constant 50% surface coverage for Ag deposition with Model 1.

This function is reasonably well represented by an increasing scaling-law dependence $\sim 1/N_{diff}^{0.3}$ with the power of 0.3, which is, in fact, the inverse of the corresponding curve in Fig. 3.9. It should be also noted that the maximum addressable value of N_{diff} is limited by the conditions at which one large cluster is formed, which depends on size of the system and the coverage considered. Next, the complete impact of temperature on the surface morphology has been investigated by varying T in both Eq.3.3 and Eq.3.4. Fig. 3.11(a,b) show the effect of temperature for two examples of metals and two different model substrates. Below 200K, diffusion is very slow and islands hardly form over the time of the simulation.



(a)



(b)

Figure 3.11. Average size of islands as a function of temperature at a constant 50% coverage for (a) two metals Cu and Ag with Model 2 (b), and Cu with Model 1 and Model 2.

This explains the initial portions of the dependencies in Fig. 3.11(a) and (b), as well as the corresponding morphologies in Fig. 3.12 and Fig. 3.13, where only minor islands are detected, if any. It should be noted that a similar trend was reported in experiments for Ag deposition in Ref [16]. More dramatic growth is observed in the temperature range 300-400K, where coarsening by Ostwald ripening becomes increasingly important when the temperature increases. Beyond 400K, however, the increase of island size with temperature slows down slightly. The reason might be that at high temperature, minor islands whose dissolution feeds growth of larger ones are dissolved rapidly at early stages of deposition, which results in a slower subsequent coarsening of the remaining larger islands.

Fig.3.11(a,b) demonstrates the effect of different activation and lateral bonding energies that correspond to two different metals and two different models, and Fig. 3.12 and Fig. 3.13 show the corresponding snapshots at various temperatures for Ag and Cu. Since Cu has a higher activation energy for surface diffusion, the corresponding number of diffusion steps is lower than for Ag. As a result, the island size is smaller in the case of Cu than for Ag deposition at similar temperatures. This observation from the models is consistent with experimental results shown in Fig. 1.4.

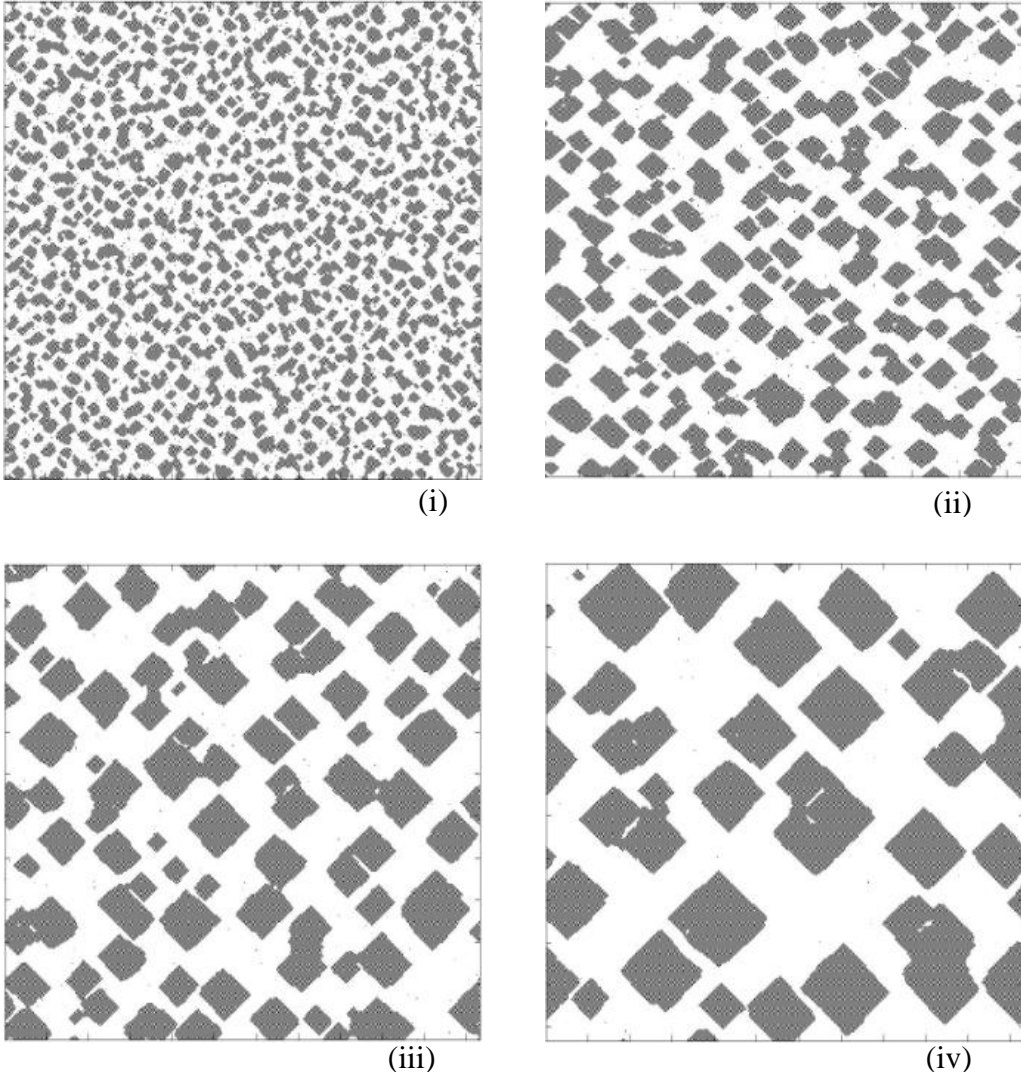


Figure 3.12. Simulated surface morphologies for Ag deposition on Model 2 at temperatures of (i) 250K, (ii) 300K, (iii) 350K and (iv) 400K for 1 min deposition at $R=0.0093\text{ML/sec}$.

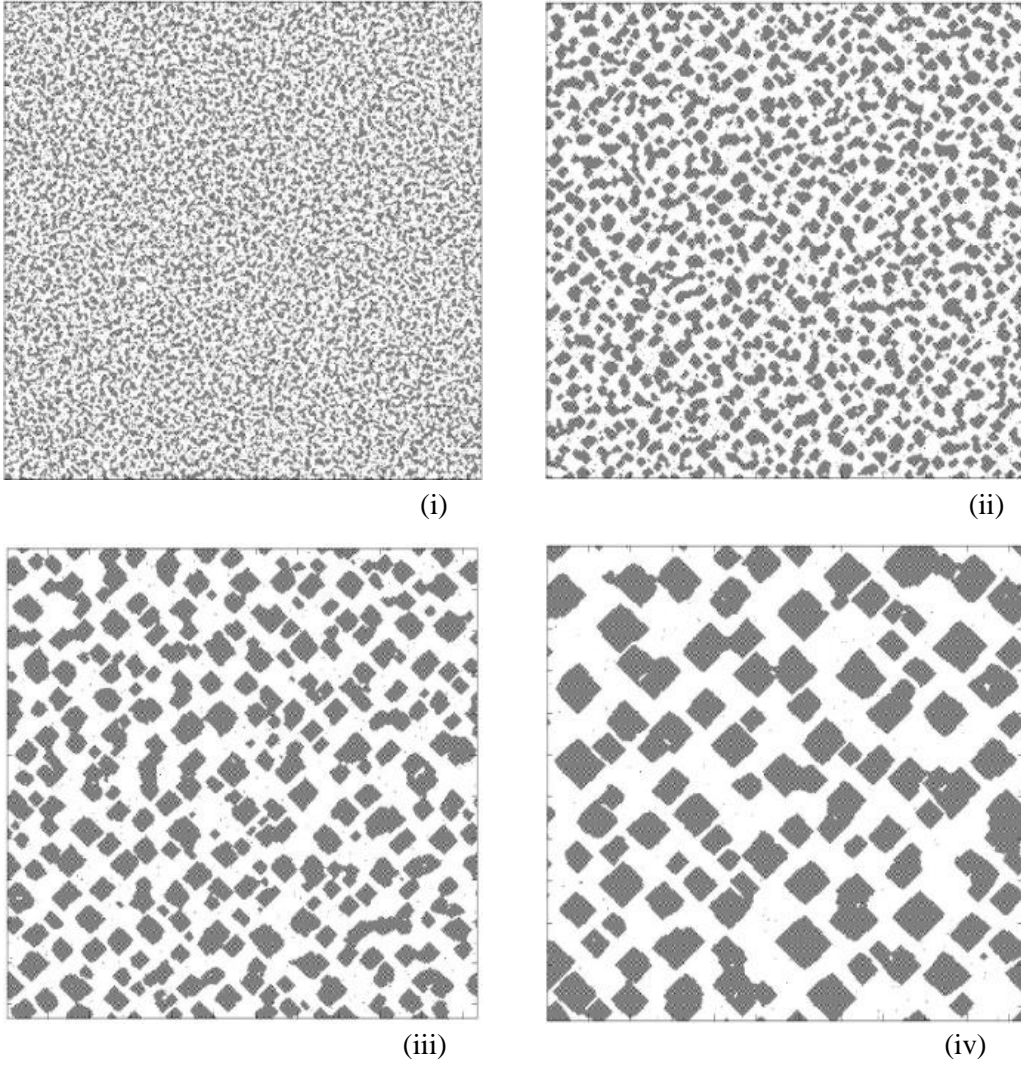


Figure 3.13. Simulated surface morphologies for Cu deposition on Model 2 at temperatures of (i) 250K, (ii) 300K, (iii) 350K and (iv) 400K for 1 min deposition at $R=0.0093\text{ML/sec}$.

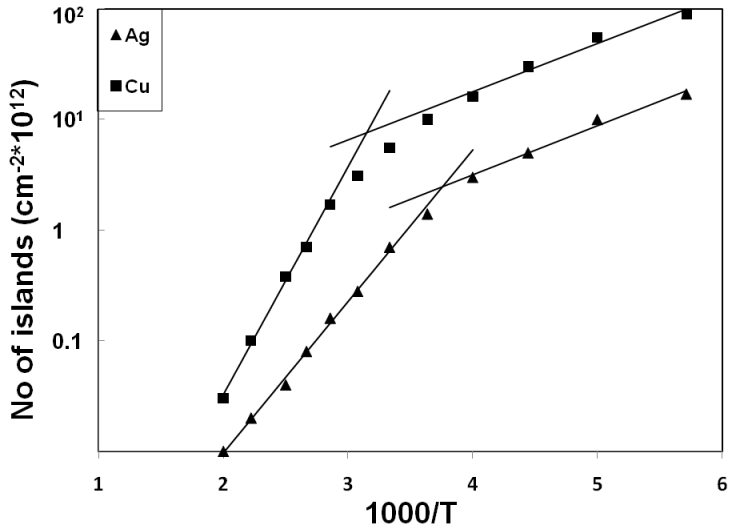


Figure 3.14. Average density of islands as a function of temperature for Cu and Ag with Model 1.

Finally, Fig. 3.14 presents the density of islands as a function of temperature for Cu and Ag using Model 1. Clearly, lower density of islands is observed at higher temperature with fixed surface coverage. However, the dependencies in Fig. 3.14 cannot be described by a simple exponential dependence or scaling law with a single activation energy U . The numeric dependencies rather show a crossover between two Arrhenius-like regimes with different activation energies, which occurs at temperatures close to 300K. At lower temperature, the lateral binding of adatoms may be considered irreversible since thermally activated bond breaking is negligible. When temperature increases, the thermally activated bond breaking events occur more frequently and the transition from the irreversible regimes to reversible ones occurs. From the simulation results presented in Fig. 3.14, two

Arrhenius-like dependencies have been identified for both Cu and Ag. The lines were drawn using the least-square fitting of subsets of the simulations results representing the asymptotic behaviors. The fitting errors were below 3% respective to the numerical results that were employed for the fitting. The effective activation energies for the low-temperature and high temperature regimes were found to be, respectively, 0.0382 ± 0.0041 eV and 0.1179 ± 0.0067 eV for Ag, and 0.0374 ± 0.0046 eV and 0.1778 ± 0.0008 eV for Cu. Such a behavior is observed in experiments [16, 32, 53, 98], and accompanied by the increasing impact of Ostwald ripening (also associated with reversible jumping) at increased temperatures.

3.3.5 Random Number Generation and Its Effect on Results

Random number generation and its quality is an important factor in KMC modeling. An ideal random number generator creates series of numbers that do not follow any periodicity or other predictable sequence. There are two common methods to generating random numbers using computers: the pseudo-random number generators and the true random number generators. Pseudo-random number generators use mathematical formulae to produce sequences of numbers that appear random. The most widely used algorithm for generating pseudo random number is the linear congruential method which is fast to execute. Pseudo random number generator is efficient, however, its output can be reproduced in the same sequence if the seed conditions are kept the same which is useful for debugging. For practical KMC simulation, a pseudo random number generator

must have a period so long that it can be ignored for most practical purposes. A true random number generator extracts randomness from physical phenomena acquired through a computer. An example might be intervals between radioactive decay. However, the cumbersome nature of measuring such phenomena limits the popularity of this method.

I used the C++ standard library pseudo random number generator “rand ()” function for generating random numbers in my simulation. The function returns an integer that is in the range from 0 to RAND_MAX. Here, RAND_MAX is the largest representable positive value of type short integer. When I needed a random number between 0.0 and 1.0, I used expression like “rand () / (RAND_MAX+1.0)” in the simulation to ensure the value remain less than “1.0”. The function “srand (seed)” enables of different sets of random numbers by using different seeds. Keeping the same “seed” value, the same set of random numbers can be reproduced.

In each Monte-Carlo simulation history, a specific surface configuration is generated. Here I check how change in random number sequence with different seed value affects the average island size presented in the simulation. For each condition from Fig. 3.5(a), I have run 6 different independent simulations. The resulting individual and average island size values as well as the standard deviations are shown in the Tab. 3.2. Fig. 3.15 compares the results of Fig. 3.5(a), the outcome of seed 1, with the average size over the other 6 runs. It can be seen

that the results from individual MC simulations are very well representative of the statistical average from several independent simulations.

Table 3-2. Island size of different sets of simulation at a given deposition rate, their average and standard deviation, for the conditions from Fig. 3.5(a).

Deposition Rate R, ML/sec	Island size measurements, nm							Average 1-6	RMSD
	Seed 1 (Fig.3.5a)	Seed 2	Seed 3	Seed 4	Seed 5	Seed 6			
0.00125	4	4.1	3.55	3.3	3.7	3.5	3.69	0.26	
0.00312	6.48	6.84	6.3	6.45	6.51	6.53	6.52	0.09	
0.005	7.7	7.9	8.01	7.6	7.71	7.8	7.80	0.15	
0.00625	8.12	8.2	8.2	8.23	8.45	8.22	8.26	0.12	
0.01187	9.35	9.41	9.19	9.33	9.18	9.4	9.30	0.09	
0.0187	10.8	10.93	11.05	10.79	10.96	10.89	10.92	0.10	
0.025	13.45	13.61	13.42	13.52	13.33	13.56	13.48	0.08	
0.03125	18.09	18.43	18.08	17.92	18.2	18.11	18.14	0.10	

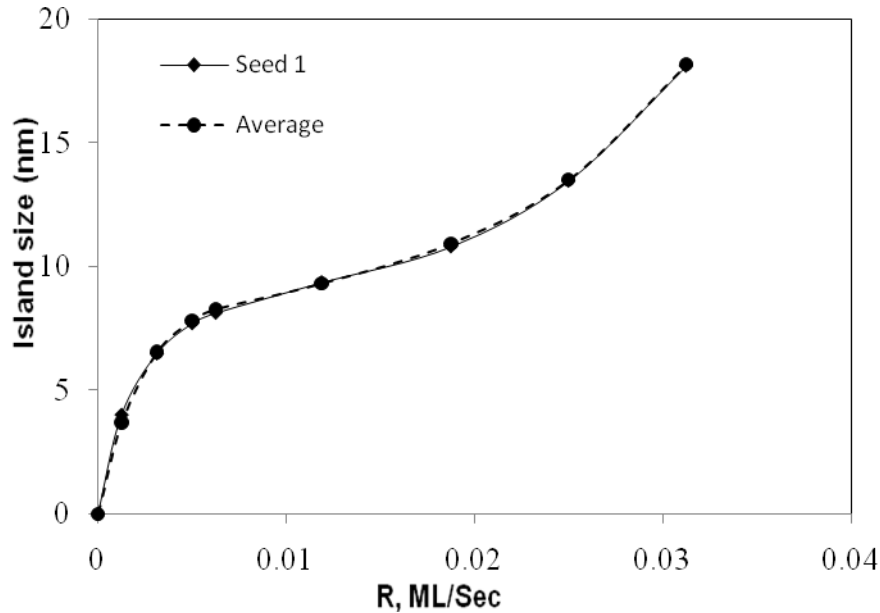


Figure 3.15. The dependence of island size on the deposition rate for the conditions from Fig. 3.5(a). Solid line represents the result of seed 1 and the dotted line is the average of the 6 runs (Table 3.2) to show the effect of the random number variation.

3.4 Summary

This chapter presents a KMC simulation for plan-view 2D morphologies of metallic nanoclusters during physical vapor deposition. Two models for the symmetry of the lateral interactions between adatoms have been investigated. One of these corresponds to (100) crystalline islands on a (100) surface with FCC symmetry, and the other one adopts the primitive lattice, which leads to softer shapes of deposited islands, and may better represent formation of nanoscale islands on non-crystalline substrates such as glass.

To model the adatom deposition and diffusion, I used the Kinetic Monte Carlo simulation method employing the Metropolis algorithm combined with the bond counting approach. Although particular aspects of the present KMC model have been either employed in the literature or anticipated to be useful [9, 10, 14, 31, 70, 76, 92, 98-100], I am unaware of a contribution which would combine all the advantages of the present lattice simulation. The innovations that particularly contributed to the efficiency and flexibility of the present model include:

(i) Explicit association of the number of deposition events (Eq.3.1) with real time, usage of deposition events as a “clock” in the model, and explicit treatment of deposition and diffusion events as statistically independent phenomena.

(ii) Algorithmic decoupling of the constant kinetic coefficient describing the number of diffusion steps in the asymptotic zero-coverage limit (Eq. 3.3) from the stochastic modeling of thermally activated jumps whose rates depend on the local configuration of adatoms (Eq. 3.4), which allows for an efficient time scale separation by avoiding explicit simulation of short frequency atomic vibrations with the fundamental frequency.

(iii) Absence of irreversible surface relaxation phenomena. From the very moment of adatom deposition at the surface, the rates of all surface jumps are given by reversible Arrhenius dynamics (Eq. 3.4) bringing the model of surface mobility in accordance with the principle of detailed balance, and resulting in statistically consistent predictions.

(iv) Usage of a simple but accurate bond counting approach to evaluate the surface energetics resulting in an extremely efficient numerical algorithm without well-known bookkeeping issues. For example, in the Embedded Atomic Model (EAM) [101-104], where an atom's local energetics is calculated with a detailed accounting of the interaction of all neighboring atoms, regular updates and comparisons of large catalogs of the system configuration are required. In distinction, my model covers the dependence of the surface energetic on the local configurations largely as the EAM model does, but it does not require any extensive arrays of data beyond the current surface configuration. As an alternative to the EAM model, the Lennard-Jones (LJ) potential based model has also been adopted [105-107] which is simpler than the EAM based approach and also is believed to be more reliable. While I employ the LJ potential in a complementary off-lattice simulation described in Chapter 6, in the present lattice model the simple bond-counting method has been employed. As a result, despite a significant rejection rate associated with the usage of the Metropolis algorithm, the lattice model has proven to be extremely efficient numerically.

Overall, in comparison to most published KMC approaches, the present approach favourably combines consistency, simplicity, and efficiency allowing me to study thoroughly controlled nanocrystal fabrication process. The simulated dependencies of the 2D surface morphologies match benchmark experimental observations from the literature. This includes the overall shape of the islands observed, the dependencies of the morphological trends on the deposition rate,

and the realistic temperature of cross-over in the temperature dependence obtained numerically. These examples demonstrate that my model is a viable approach that adequately represents major trends of 2D surface morphologies during deposition. It is expected that numerical models like this can be employed to efficiently predict the outcomes of NC deposition, and rationally direct selection of optimal process conditions for nanofabrication. The main object is to explore the submonolayer behavior of NC formation. Two types of metal Cu and Ag deposition were investigated on two different substrate types. These examples demonstrate that my model is a viable approach that adequately represents major trends of 2D surface morphologies during deposition.

CHAPTER: FOUR

4 LATTICE BASED 3D MODEL

In the previous chapter using a 2D simulation model, I demonstrated how the process parameters such as the deposition rate, temperature, time, etc. affect the size, shape and density of NCs fabricated. A 2D modeling approach captures morphological trends of the early stages of nanoparticle formation; however, in practice NC formation does not take place entirely in sub monolayer regimes (see Fig. 1.5) [31, 33, 34, 55, 61, 62, 92, 108, 109]. To describe experimentally observed mounded morphologies, a more detailed 3D modeling approach should be employed. In this chapter I describe a KMC model for simulating 3D NC deposition in order to predict and control the morphology of the NCs fabrication by tuning the process conditions. The predicted morphologies of thin films can be characterized by the island separation, the size, shape and density of NCs. I developed a model capable of representing the specific PVD process aspects for a given set of conditions, and employ it to study the impact of these conditions on the morphology of the deposited NCs

4.1 The Model Description

The 3D simulation of self-assembled NCs synthesis employs the solid on solid (SOS) model [82, 100, 110] using a bond counting KMC method. The substrate was represented with an FCC lattice model structure in a (100) plane. The metal

atoms deposited directly onto the substrate (odd layer) are allowed to occupy alternating (x,y) locations, as shown in white in Fig. 4.1(a). In the even layer the allowed (x,y) positions change to the complementary locations (see Figs.4.1(b) and (c)). The odd and even layers repeat the symmetry layer by layer. In contrast to the previous 2D model [111, 112], the 3D model represents the morphology in a more detailed way by describing the NCs height, $h(x,y)$. In this 3D FCC lattice, an atom has 4 nearest neighbor atoms in the same horizontal layer and 4 atoms in diagonal locations in each of the lower and upper layers. The maximum number of nearest neighbors is therefore 12, as is the maximum number of bonds per atom. Binding with atoms located farther than the nearest neighbor locations is not considered. The simulations were performed for $L \times L = 140 \times 140$ sites with periodic boundary conditions. For the 3D model, boundary conditions are applied similarly to the 2D model in “x” and “y” directions but not in the “z” direction. It is assumed that the distance between nearest neighbor atoms in the lattice, d , is equal to 0.25 nm resulting in the size of the simulated region $L = 25 \text{ nm}$. The height of a site is defined by

$$h(x, y) = N_h d / \sqrt{2} , \tag{4.1}$$

where N_h is the number of layers at a given location. In the following discussion, the average height, \bar{h} , is defined by the sum of maximum heights at all occupied (x,y) sites divided by the total number of the occupied sites. In the SOS model, at each Monte-Carlo deposition step, an (x,y) location is selected randomly.

Deposited atoms can occupy only allowed (white) sites in the upper layer at the given (x,y) location.

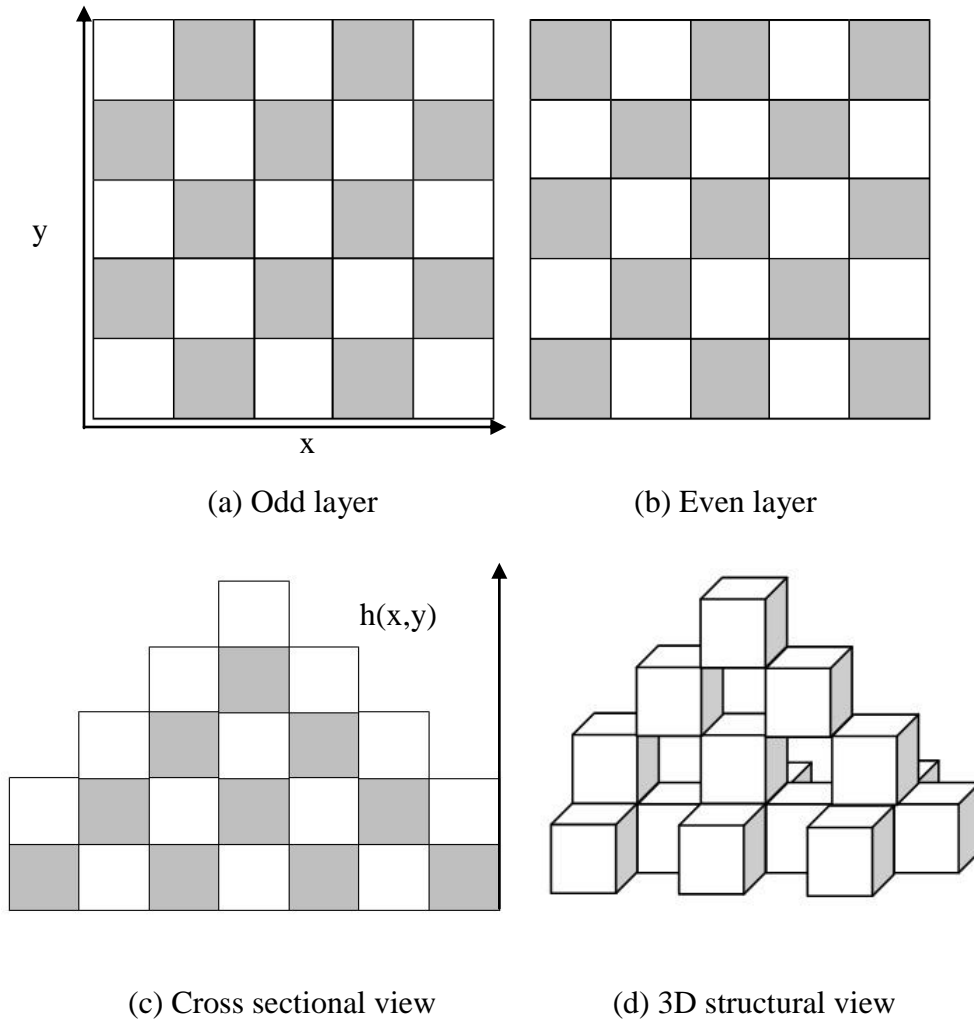


Figure 4.1. Model for FCC lattice. The white rectangles indicate the allowed positions for occupancy. (a) Odd layer (b) Even layer (c) Cross sectional view and (d) 3D structural view.

The approach to model deposition and diffusion steps is similar to that described in sec 3.1, except for the possibility for adatoms to diffuse over a 3D surface. The activation energy in Eq.3.3 was adopted equal to 0.46 eV. At each attempted diffusion step, an initial (x,y) position before the jump, “1”, is selected randomly. If the position is occupied, one of its eight (x,y) nearest neighbors is selected randomly and labeled “2”. If the position “2” is available for occupation, the adatom jumps from position “1” to position “2” according to employing the Metropolis algorithm with the energy function $F + F_s$, where F and F_s represent the binding energies of the deposited adatom with other adatoms and the substrate, respectively. The corresponding probability of adatom’s jump from position “1” to position “2” is given by

$$P_{1-2} = \min \left(1, \exp \left(- \frac{(F_2 + F_{s2}) - (F_1 + F_{s1})}{kT} \right) \right), \quad 4.2$$

Here $F = -yn$, where y is the energy of a bond between two adatoms and n is the number of adatom-adatom bonds in a given position.

We set $F=0$ for locations where the number of bonds n is less than a critical number n_c , $n \leq n_c$, where n_c is adopted to be 2. Similar to chapter 3, the energy of bonds between adatoms, y , was derived from the cohesive energy. Assuming that the cohesive energy represents the binding of a surface atom with 8 nearest neighbors, the estimate of the energy per bond based on the measured cohesive energy for Cu provides approximately 0.44 eV.

In the absence of defects at the surface of the substrate, the adatom-substrate binding energy F_s can be represented as $-4y_s$ for the 1st layer and is equal to 0 for upper layers. Here y_s is a nominal energy of an adatom-substrate bond, which may differ from y . Varying the substrate-adatom binding is also important to understanding how the change in the substrate binding energy affects the morphology of deposited nanostructures. The labels “1” and “2” in Eq.4.2 denote the energy function in the corresponding locations before and after the attempted jump, respectively. The flowchart of 3D KMC lattice based model is shown below in Fig.4.2 (a) and Fig. 4.2 (b) shows the diffusion steps simulation flowchart.

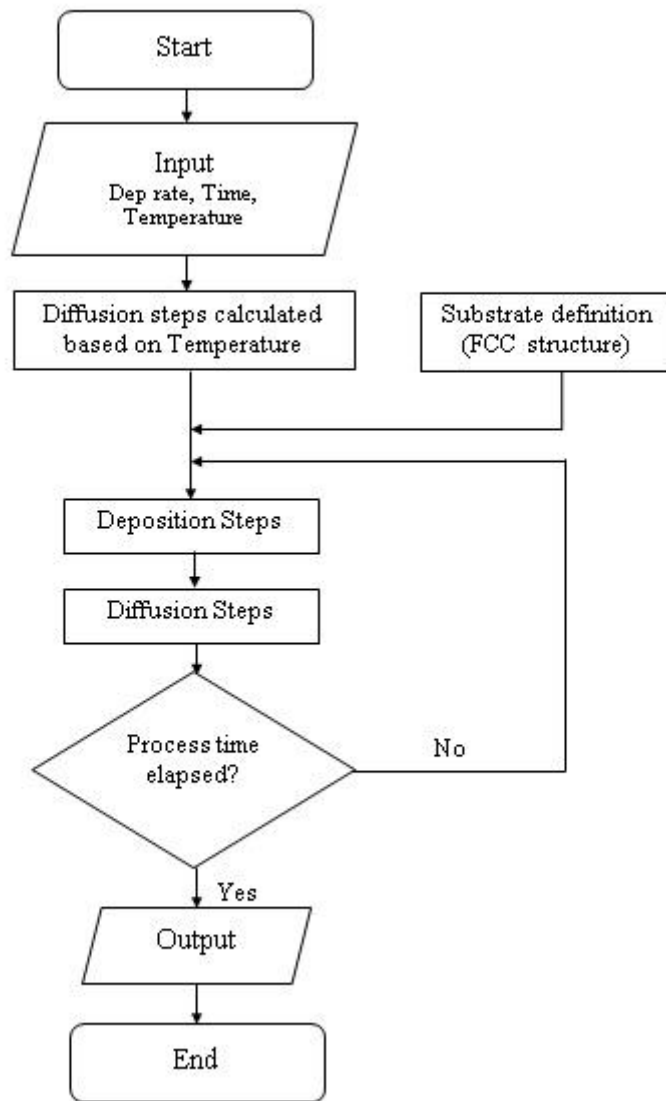


Figure 4.2 (a). Flowchart of 3D KMC lattice simulation process.

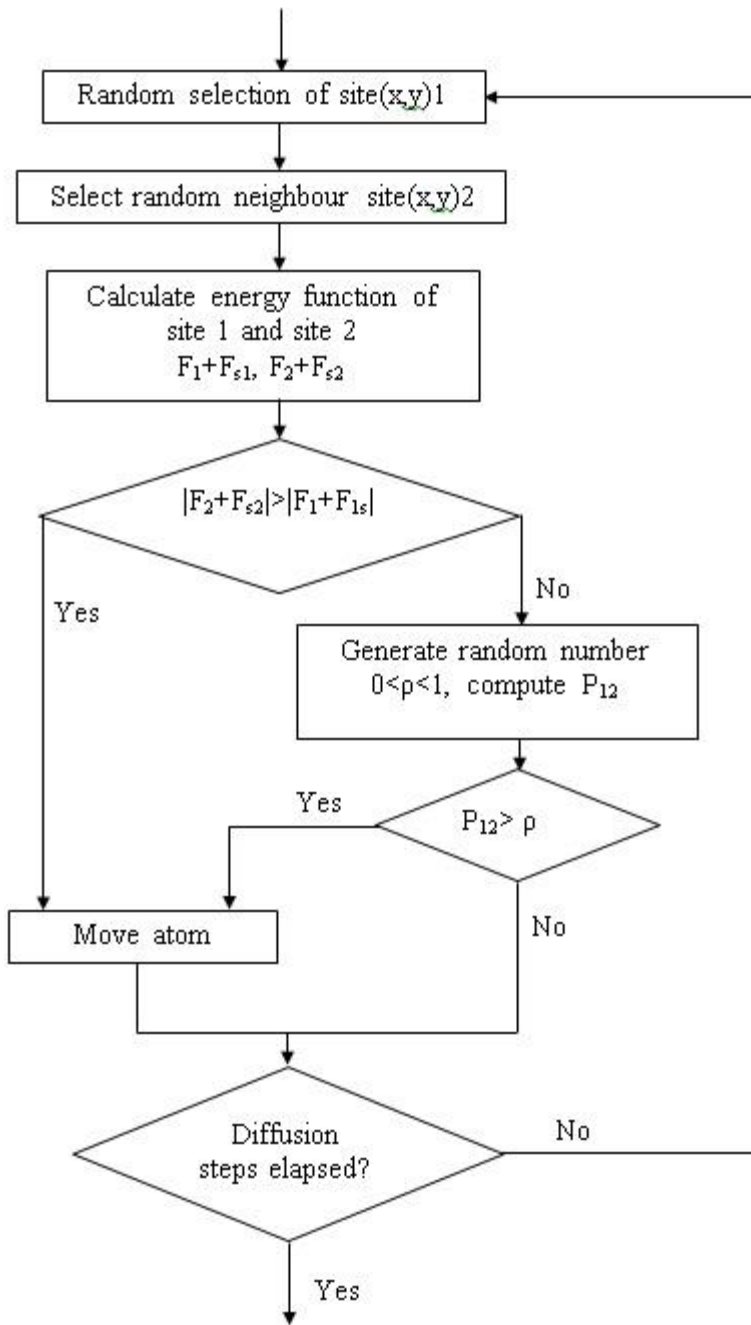


Figure 4.3 (b). Diffusion steps simulation flowchart.

4.2 Results and Discussion

4.2.1 Evolution of surface morphology during deposition of nanocrystals

The first example presents a simulation of deposition of Cu atoms on a Cu (100) substrate at the rate $R=0.086\text{ML}/\text{sec}$, which is equivalent to $0.2\text{ nm}/\text{sec}$, at room temperature. Fig. 4.3 shows snapshots of the surface morphology after 5 sec, 30 sec and 60 sec of deposition. Row (a) presents 3D images of the morphology and row (b) shows the corresponding 2D projections. As one could expect, the islands nucleate spontaneously at the surface and their size increases with time. At some point, the islands start merging while retaining the pyramidal surface morphology similarly to the experimentally observed behavior [33, 34, 56], see also Fig. 1.5. To characterize the surface morphologies, I employed the islands' density (N) and lateral size (S). As previously, the latter is defined by the island's average surface diameter [112], calculated as four times the total surface area of islands divided by their total surface perimeter.

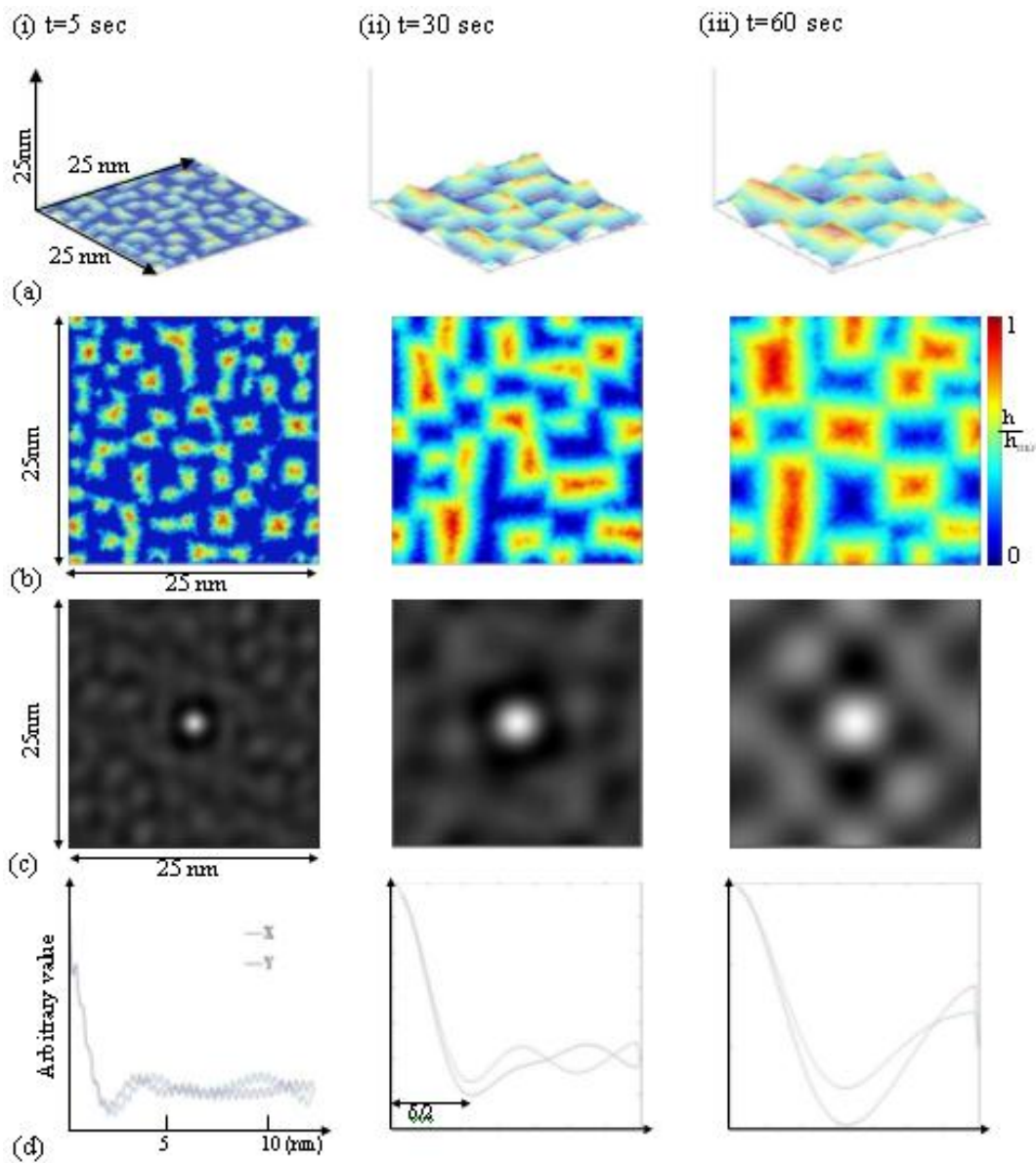


Figure 4.4. Simulated surface morphologies demonstrating Cu islands' growth for deposition times of 5 sec, 30 sec and 60 sec at $T= 300$ K and $R=0.086$ ML/sec or 0.2 nm/sec. (a) The 3D view of the substrate, (b) the 2D view of the same images, (c) the 2D height-height correlation function, and (d) the 1D height-height correlation function of the above substrates.

Furthermore, the inter-island distance was estimated from the height-height correlation function,

$$C(r,s) = \sum (h(x,y) - \bar{h})(h(x+r,y+s) - \bar{h}) , \quad 4.5$$

Here $h(x,y)$ is the height of a location of reference defined by eq.(4.1), $h(x+r,y+s)$ is the height at a location $\{x+r,y+s\}$, and \bar{h} is the average height value. Row (c) in Fig. 4.3 shows the examples of $C(r,s)$ functions representing the symmetry of the patterns, and row (d) presents the normalized $C(r,0)$ and $C(0,s)$ dependencies. The first large minima in these dependencies are representative of the half the average distance ($\delta/2$) between islands. One of them represents the X-direction relationship and the other in Y-direction relationship. In the correlation function shown in Fig. 4.3(d-i), oscillations are visible resulting from the periodic FCC structure of the uncovered substrate. At later stages of deposition when the coverage increases (Fig.4.3 (d-ii) and (d-iii)), this oscillatory component vanishes.

In Fig. 4.4, the average size and distance of Cu clusters are shown as functions of deposition time. It can be seen that both the island size and inter-island distance increase with time. At early stages of deposition when stable islands form, their lateral size increases rapidly with the arrival of new adatoms.

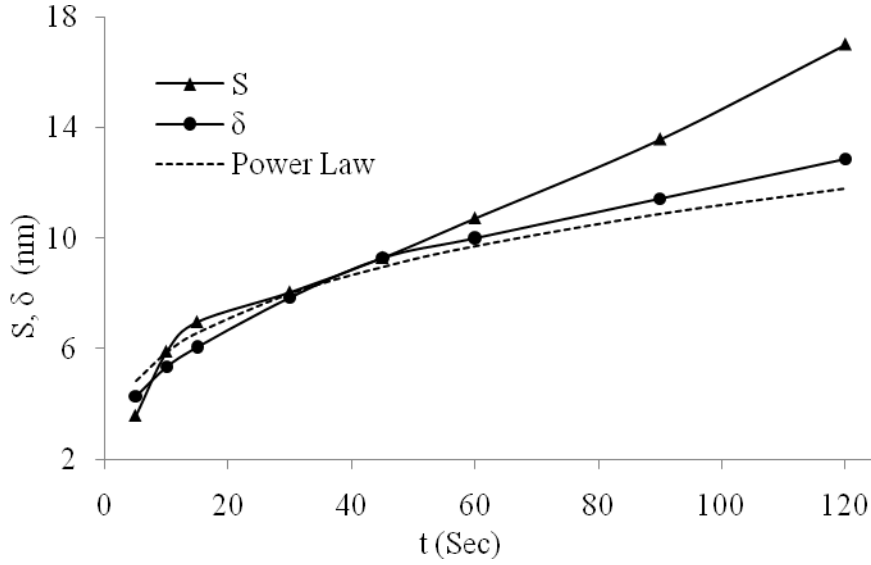


Figure 4.5. Average island size (S) and inter-island distance (δ) as functions of time (t) at the deposition rate $R=0.086\text{ML}/\text{sec}$ and $T=300\text{K}$.

If the deposition continues, stable islands keeps growing both laterally as well as vertically (see Fig. 4.3 (a)), and the evolution in the lateral dimensions somewhat slows down after the initial stage as can be seen in Fig. 4.4. One could expect that the regimes of slower growth (after approximately 15 sec in Fig. 4.4) can be described by the analytical scaling law for the inter-island distance (Eq. 2.12). This power law dependence with $m=0.28$ is also shown in Fig. 4.4. The power law function follows closely the inter-island distance $\delta(t)$ derived from the minima of the correlation functions. However, the average size dependence $S(t)$ is reasonably close to the theoretical prediction only for deposition times less than approximately 60 sec, after which the dependence $S(t)$ deviates from both $\delta(t)$ and the power law. The reason is that with time, the islands' bases start to overlap

which affects the estimates of the average island's size S , but not the inter-mounds distance δ . Thus, the described dependencies $S(t)$ and $\delta(t)$ provide complementary descriptions of the surface morphology, and only $\delta(t)$, but not $S(t)$, can be represented by scaling law (2) with $m=0.28$ at advanced stages of the deposition.

At room temperature, the morphology determined experimentally for Cu islands grown on Cu(100) can be described by $m=0.25$ [34] and that for Fe/Fe(100) has been matched by $m=0.16$ [55]. At increased temperatures, a Fe/Mg(100) system fits the value of $m=0.25$ at 400 K, [56] Ge/Ge(100) morphology can be represented by $m=0.4$ [54] at 500 K and Rh/mica corresponds to $m=0.33$ [57] at 700 K. Theoretically, a universal value of the coarsening exponent $m=0.25$ has been derived by Mullins [60] by analyzing a kinetic equation describing adatom diffusion on a mounded surface. More recently, the value of the power exponent $m=0.25$ was confirmed by Hunt [59] considering a more detailed kinetic model of surface mobility on a mounded landscape with an accounting for the Schwoebel barriers. However, subsequently Siegert [58] has demonstrated that, although in most cases a 0.25 value of the exponent could be expected, it may adopt values between 0 and 0.33 depending on the material and islands' geometry. The present estimate of $m=0.28$ falls into the interval between the generic value of $m=0.25$ and the upper theoretic limit of 0.33, and is in a reasonable agreement with the reported experiments.

Overall, the predicted morphology of growing NC's is compatible with both the theory as well as with experimentally reported morphologies, both at an early post-nucleation stage (see e.g. Fig. 1.5) as well as at later stages when the deposited structures contain multiple layers of atoms.

4.2.2 Control of NC synthesis by varying the deposition rate

As the next step, the capability of the model to demonstrate control over the morphology of self-assembled arrays of NC's during PVD synthesis by varying the conditions of deposition is explored. One of the major process parameters in PVD of NCs is the deposition rate [31, 34, 55, 62, 63, 113, 114]. Fig. 4.5(a) shows the 3D images representing the evolution of the morphology with time at various deposition rates, and Fig. 4.5(b) shows 2D images for the same examples. From Fig. 4.5, it is evident that there are gradual changes in size and density and inter-island distance due to the change in deposition time t and rate R . By varying these two parameters, a significant control over the NC's fabrication process can be reached.

Similarly to the study in chapter 3, the effect of deposition rate on the inter-island distance and density for two different process conditions is investigated below.

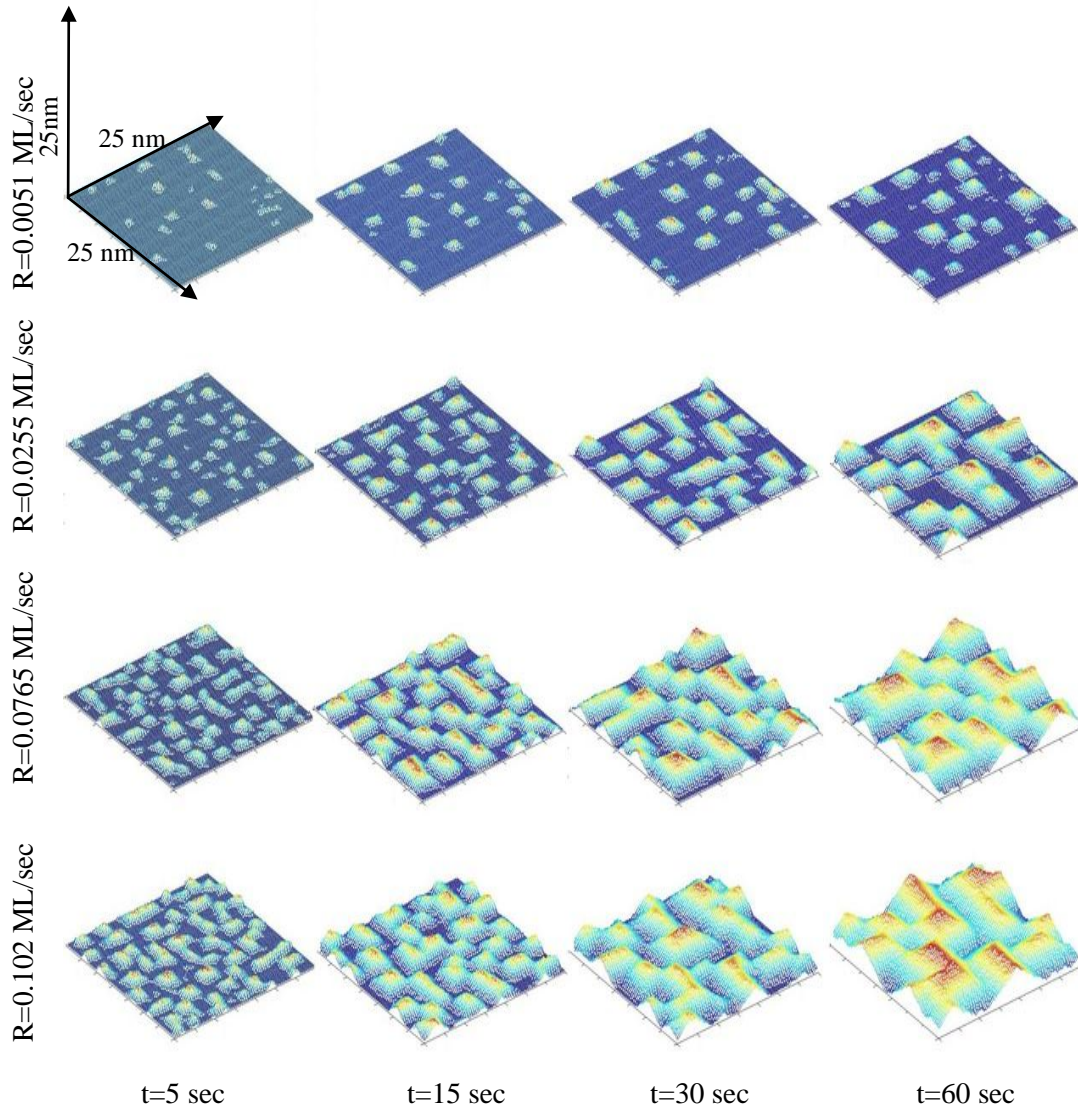


Figure 4.6 (a). Effect of deposition rate and time on the 3D surface morphology. Gradual changes of NC size and shape observed due to changes in parameter R (ML/sec) and t (sec) at $T=300$ K, $y_s=y=0.39$ eV; 3D view.

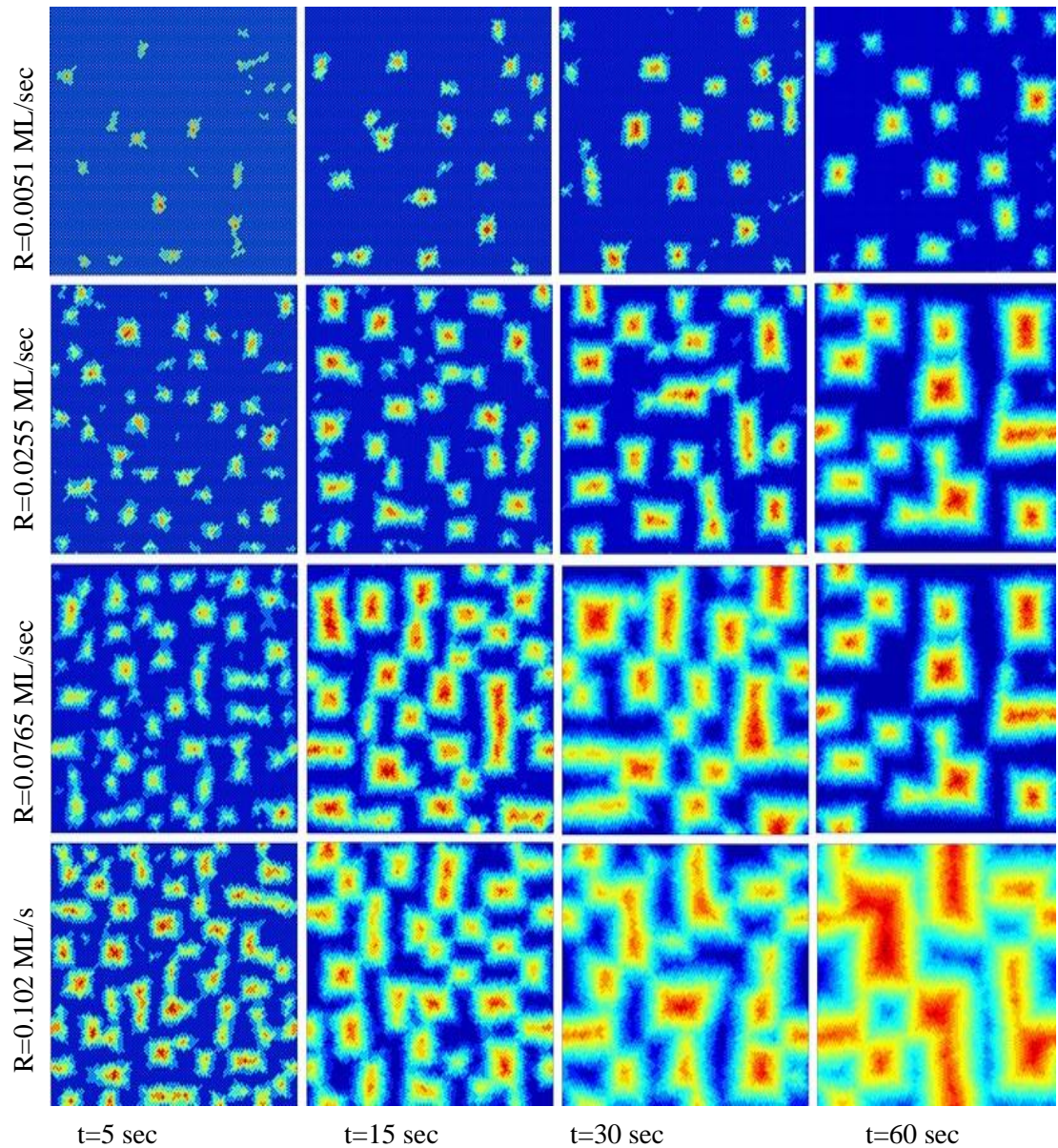


Figure 4.7 (b). Effect of deposition rate and time on the surface morphology. Gradual changes of NC's' size and shape observed due to change in parameter R (ML/sec) and t (sec) at $T=300$ K, $y_s=y=0.39$ eV; 2D view.

One deposition process occurs at a fixed time of deposition, and the other one employs a fixed amount of deposited material θ (coverage). In contrast to the previous 2D study where the coverage θ was kept relatively low to ensure sub-monolayer deposition regimes, here this constraint is absent and as such it is possible to consider larger amounts of deposited material that result in a pronounced mounded morphology.

Fig.4.6 shows the effect of deposition rate R on morphology and the 1D correlation function for constant time $t=30$ sec (Fig.4.6(a-b)) and constant coverage for $\theta=2.6$ ML (Fig.4.6(c-d)), by varying the deposition rate in the same limits from $R=0.0051$ ML/sec to $R=0.102$ ML/sec. The correlation function characterizes the effect on separation due to change in deposition rate.

Fig.4.7 shows the same effect on N and δ . In this figure, circles denote the constant time process, triangles denote the constant coverage process, and the dotted lines show power law approximations. Fig. 4.7(a) shows the dependence of the island density (N) on deposition rate (R). The density of islands is determined by counting their number on a $25\text{ nm}\times 25\text{ nm}$ surface area accounting for the periodic boundary conditions.

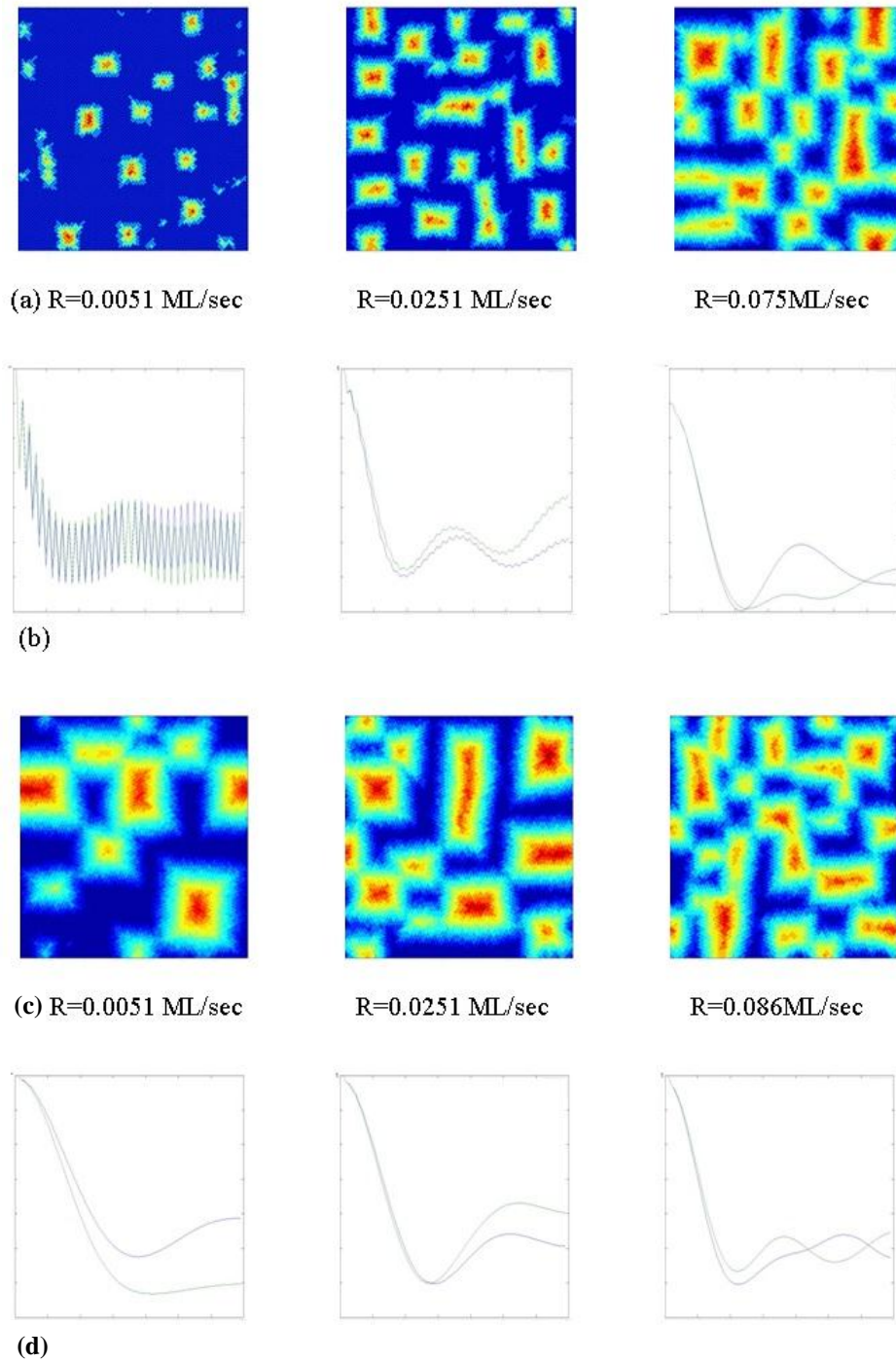


Figure 4.8. Effect of deposition rate at fixed time 30 sec, for (a) deposited substrate and (b) 1D H-H correlation. Effect fixed coverage 2.6ML for (c) deposited substrate and (d) 1D H-H correlation. All simulations at 300K.

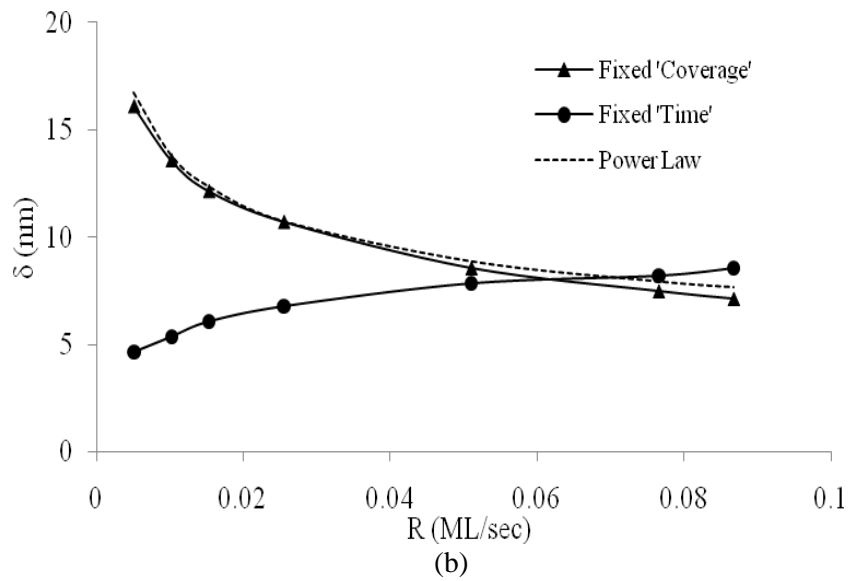
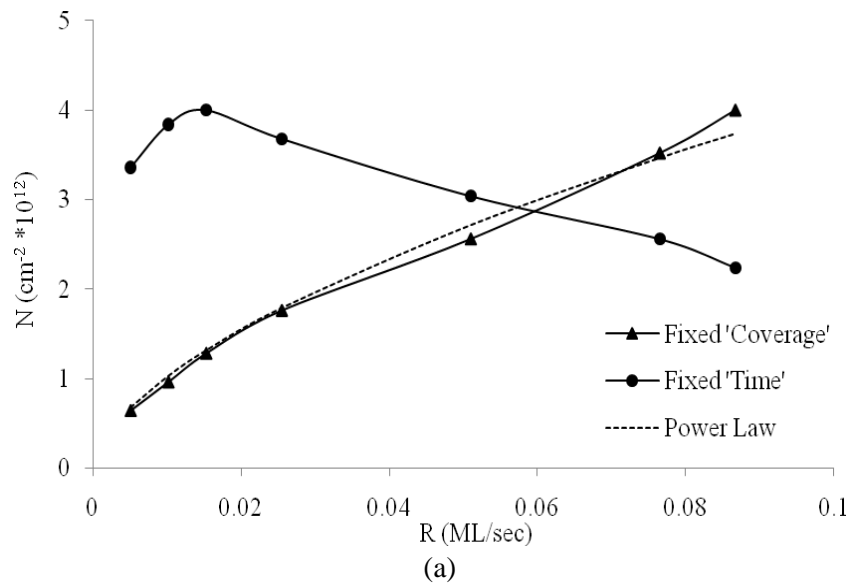


Figure 4.9. (a) The average island density and (b) average inter-island distance, as functions of the deposition rate R , for fixed time $t=30$ sec and for fixed coverage of $\theta=2.6$ ML, at $T=300$ K.

At constant deposition time and low deposition rate R , the island density N increases with the increase of R , reaching a maximum between 0.01 and 0.02 ML/sec, then decreasing smoothly with further increase of R . For $R > 0.08$ ML/sec, the decrease in N becomes slightly sharper.

The reason for this behavior might originate from the synergy of several elementary processes, the arrival of new adatoms resulting in the island nucleation and growth, and further coalescence of growing islands. As a result, the growth of existing stable islands and the nucleation of new islands occur simultaneously, and the morphology is determined by these processes. As a result, at low deposition rate R with fixed t , a small number of stable islands arise, leaving vast surface area island-free. At higher R , the island density N keeps growing as long as the amount of deposited material θ increases [111, 112]. The maximum number of islands is observed at coverage $\theta \sim 0.5-0.7$ ML. Further increase of R results mostly in an increase of the islands' height h , whereas the number of islands N rather starts decreasing by merging of neighboring islands. When deposition occurs at constant coverage θ , the density N increases steadily with increasing R because a facilitated nucleation at higher R provides a larger number of stable nuclei per unit area. In Fig. 4.7(a), I also show the dependence of $N(R)$ from the scaling law described by Eq.2.11. The corresponding exponent value p was estimated to be approximately 0.60, which is close to the asymptotic value of 0.55 based on the critical number of bonds adopted in the model ($i=2$) with the correction for 3D geometry [50, 51].

Fig. 4.7(b) presents the dependence of the average inter-island distance δ on the deposition rate R . For constant deposition time t , the distance δ increases with R , with the increase being more pronounced at low deposition rate. This trend is consistent with the corresponding decreasing part of the dependence of the islands density $N(R)$ in Fig. 4.7(a), and is explained by the prevailing coalescence of islands as discussed earlier. In the case of constant amount of deposited material θ , with low R , the inter-island distance δ decreases with R because higher deposition rates produce more stable nuclei per unit area, resulting in a decrease in the inter-island distance. The dotted line shows the power law describing the average distance δ at fixed θ , (Eq.2.10). The dependence in Fig. 4.7(b) is reasonably described with p equal to approximately 0.54, which matches very closely the asymptotic estimated value of 0.55. Thus, for constant coverage θ , the average density N and distance δ of islands can be described by the scaling law (Eq.2.11). In contrast, the scaling law expressed by Eq.2.10 and its derivatives are inapplicable to the constant t dependencies in Figs.4.7(a,b).

From the results presented, it is evident that the variation of deposition rate is a powerful control factor and a process engineer can determine density, growth and separation by setting deposition rate conditions during NC fabrication. Although the scaling laws can provide a reasonable approximation for constant-coverage deposition processes, in practice the fabrication of NCs may depend on a multitude of various factors, not all of which can be captured by simple analytical

dependencies. An efficient yet more flexible KMC simulation technique can help to comprehend the synergism of the various contributing factors. Furthermore, 3D KMC simulations reported here provide important information on the detailed morphology of the surface for better understanding of the trends of deposition, as well as for efficient in silico aided PVD process design. This process, however, depends on other conditions, such as the temperature and substrate type, whose impact should be accounted for properly.

4.2.3 Effect of temperature and surface binding energy

Temperature of the substrate is another major control factor for NC fabrication [31, 52, 55, 57, 62, 63, 66, 67, 97]. Despite extensive literature on this subject, few numerical studies address simulation of the NC's synthesis in practical temperature regimes. This section reports 3D KMC simulations of the temperature dependence for the range from 225 K to 375 K, which is immediately relevant to PVD applications. In the model, temperature has a direct effect on the surface diffusivity of adatoms and also influences the reversibility of the model, see Eqs.3.3 and 4.2, respectively. In Eq.4.2 representing the probability of reversible atomic jumps, the temperature dependence comes in proportion to the energy function which in turn is determined by the nominal adatom's binding energies with other adatoms, y , and with the substrate, y_s . The ratio y_s/y represents the affinity of NC's to the substrate, large y_s/y corresponding to strong affinity. Here, 3D KMC modeling is employed to investigate the temperature dependence

of the surface morphologies for various wetting conditions represented by various y_s/y ratios.

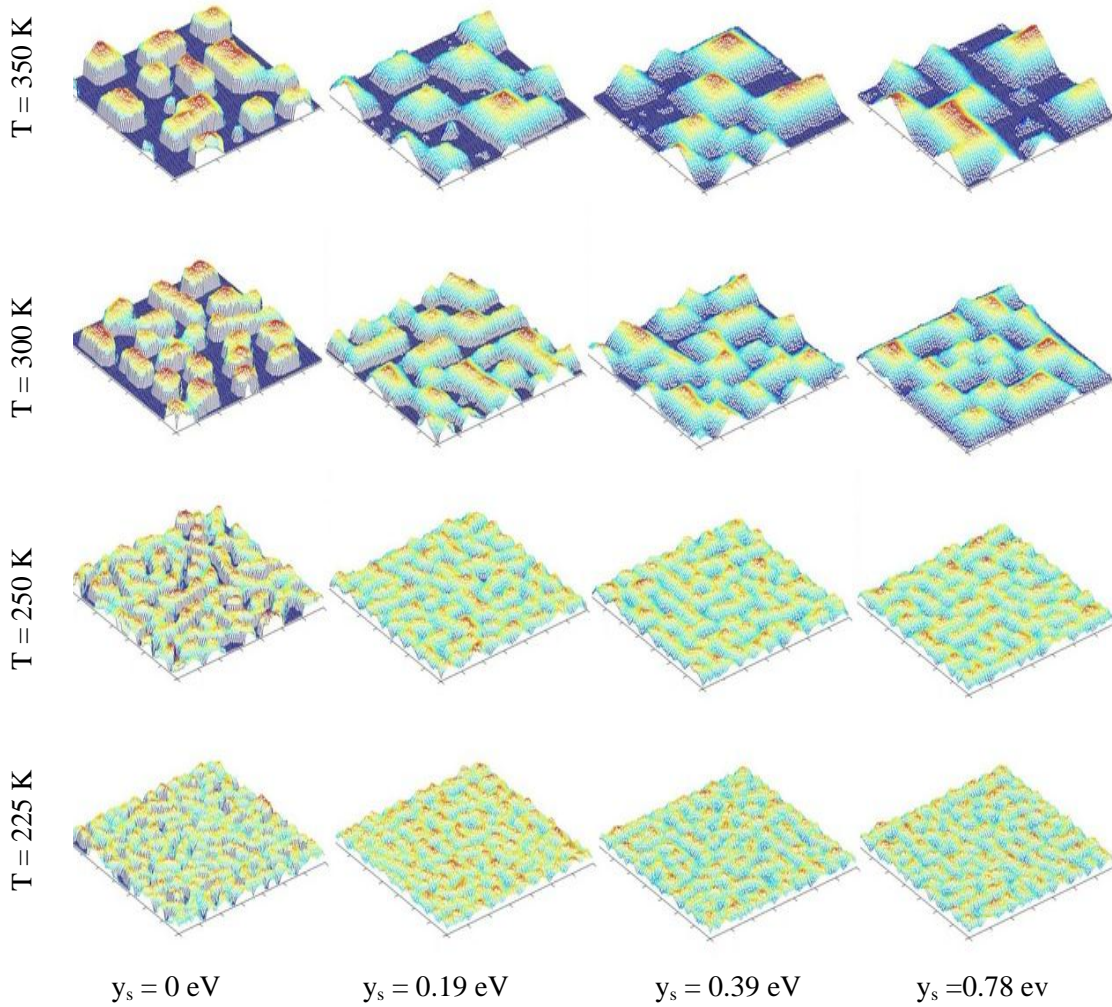


Figure 4.10 (a). Effect of temperature and the adatom-substrate binding on the surface morphology. Gradual changes of NC's size and orientation observed due to change in temperature T and parameter y_s/y at $t=30$ sec, $R=0.086$ ML/sec, $y=0.39$ eV; 3D view.

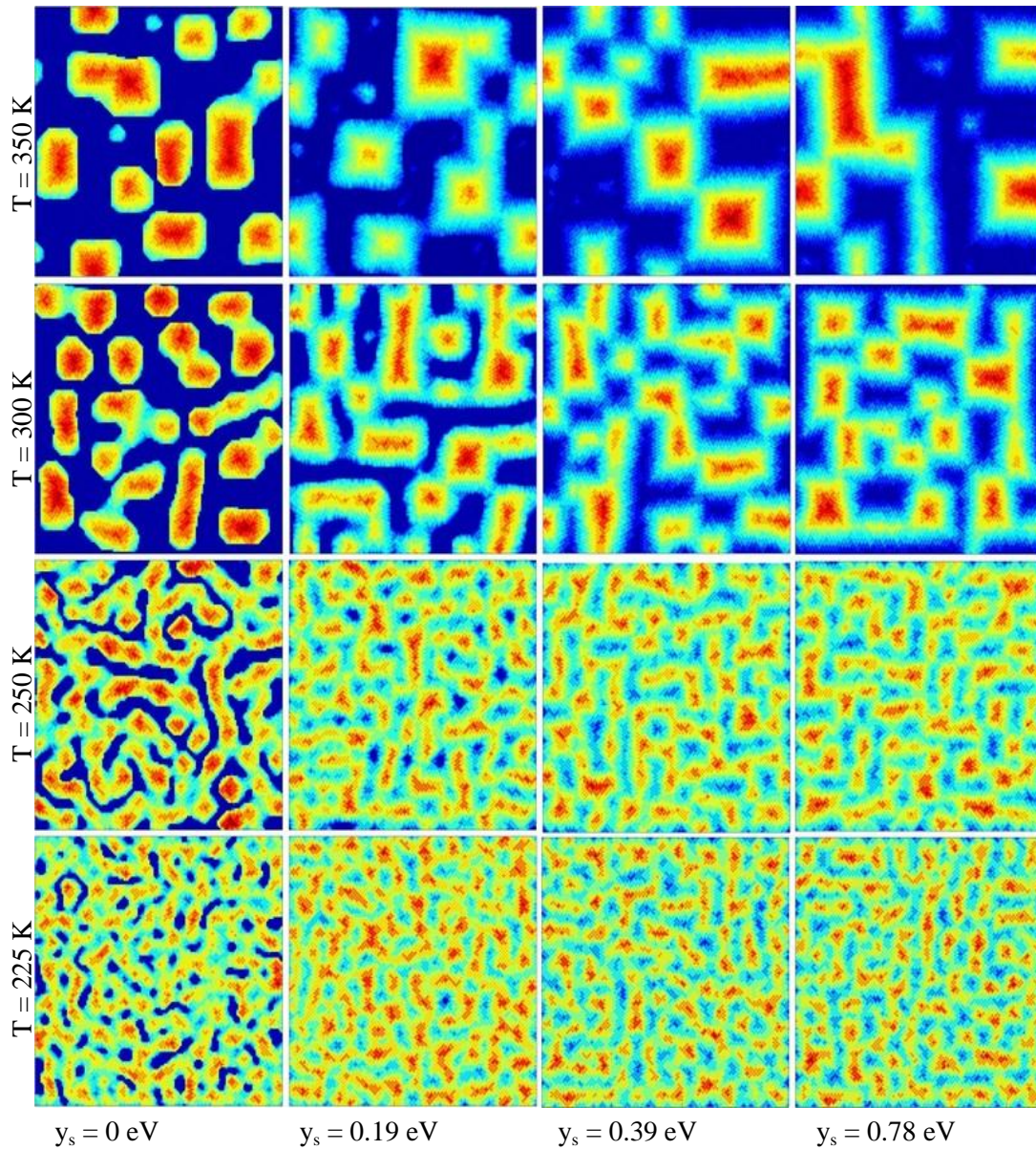


Figure 4.11 (b). Effect of temperature and the adatom-substrate binding on the surface morphology. Gradual changes of NC's' size and orientation observed due to change in temperature T and parameter y_s/y at $t=30$ sec, $R=0.086$ ML/sec, $y=0.39$ eV; 2D view.

Fig.4.8(a,b) shows the surface morphologies after 30 sec of deposition at temperatures varying from 225 to 350 K, for a set of representative substrate binding energy ratios from 0 to 2. It can be seen that the number of islands decreases and size increases with temperature, because the increased surface mobility at higher temperatures facilitates coarsening of islands both by coalescence and Ostwald ripening.

It is also observed that the change in binding energy has an effect on surface coverage, height and orientation of the NC's formed. By varying the ratio y_s/y , it is possible to investigate the influence of the wetting conditions on the surface morphology at various temperatures. In the limiting case of $y_s=0$, pillar-like islands are formed with a relatively high aspect ratio. With an increase of the ratio y_s/y from 0 to 2, the islands acquire a more regular pyramid-like shape and their bases are more pronouncedly aligned along the [100] direction. Presented here are the simulations with the ratio y_s/y up to 2; however, for y_s/y higher than 3, the influence of the wetting conditions on the size, shape and orientation of the islands becomes less pronounced.

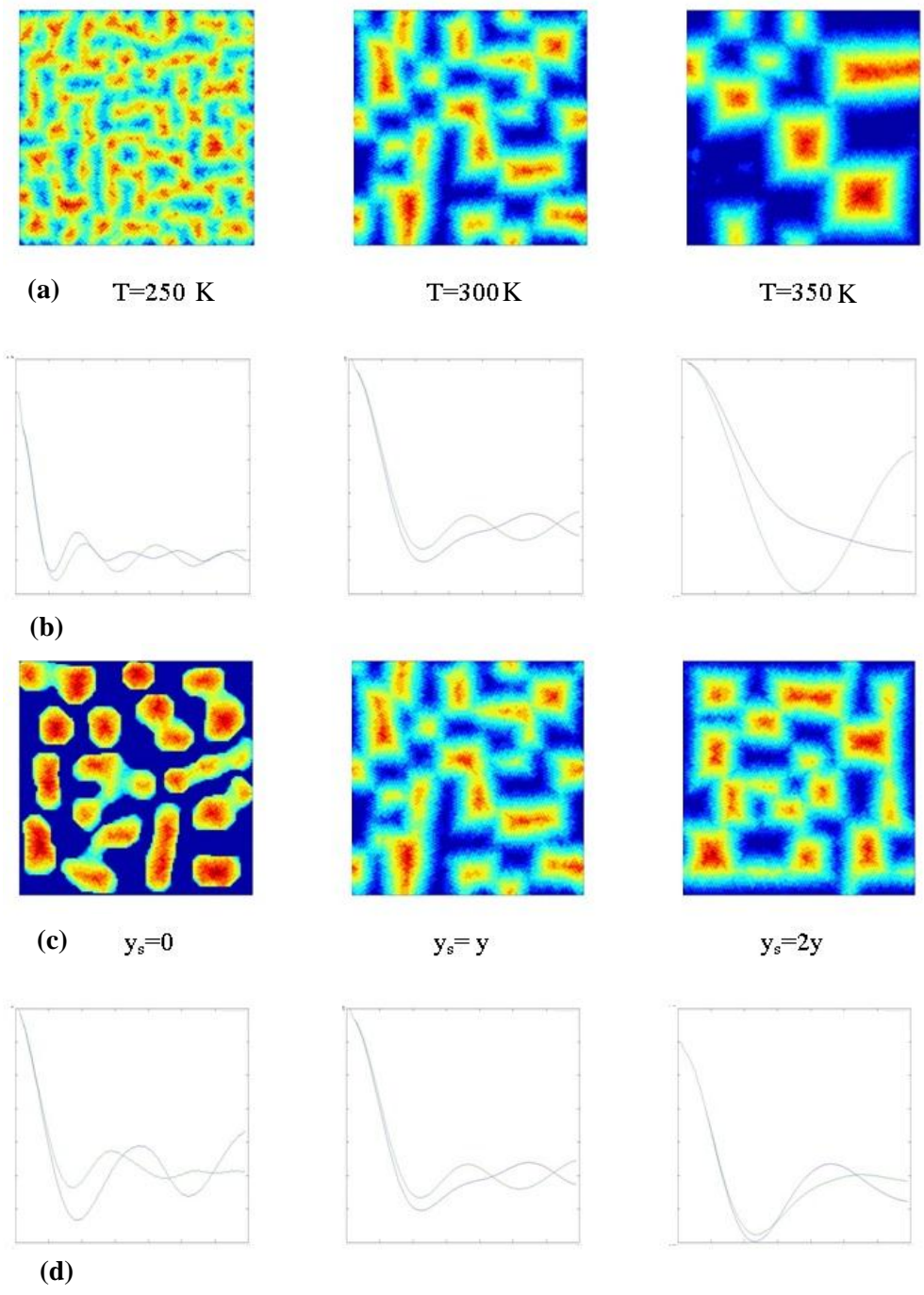


Figure 4.12. Effect of temperature ($T=250$ to 350K) (a) substrate, (b) the respective correlation function. Effect of substrate binding energy ($y_s=0$ to $2y$), (c) substrate, (d) the respective correlation function at $T=300\text{K}$, $R=0.086\text{ML/Sec}$.

Fig.4.9 shows us the morphology and the corresponding 1D correlation function demonstrating the effect of the temperature and surface binding energy on the deposited morphology. The effect of temperature on NCs size, shape and distance is clear and significant. The effect of substrate binding energy on NC shape is more pronounced when y_s is close to zero and less effective when $y_s > y$.

Fig.4.10 shows the inter-island distance δ and the average height \bar{h} as functions of the ratio y_s/y at $T=300$ K. When $y_s=0$, the inter-island distance δ is relatively low because of a larger number of higher pillars arise at this condition. With an increase of y_s the inter-island distance increases slightly, which is accompanied by a strong decrease in the islands' height. The latter, however, stabilizes when the ratio y_s/y reaches 1 and the reason might be the merging of atoms with the increase of wetting condition.

The temperature dependencies of the islands' size, height, and inter-island distance, for the example of $y_s/y=1$ are shown in Fig. 4.11. All of the dependencies are increasing functions of temperature, reflecting the trend of the increase of the NC's size, which is also seen in Fig. 4.8. Such temperature dependence is in agreement with reported experiments [31, 52, 55, 57, 62, 63, 66, 67, 97], and results from an increased surface mobility that facilitates the NC's coarsening at higher temperatures.

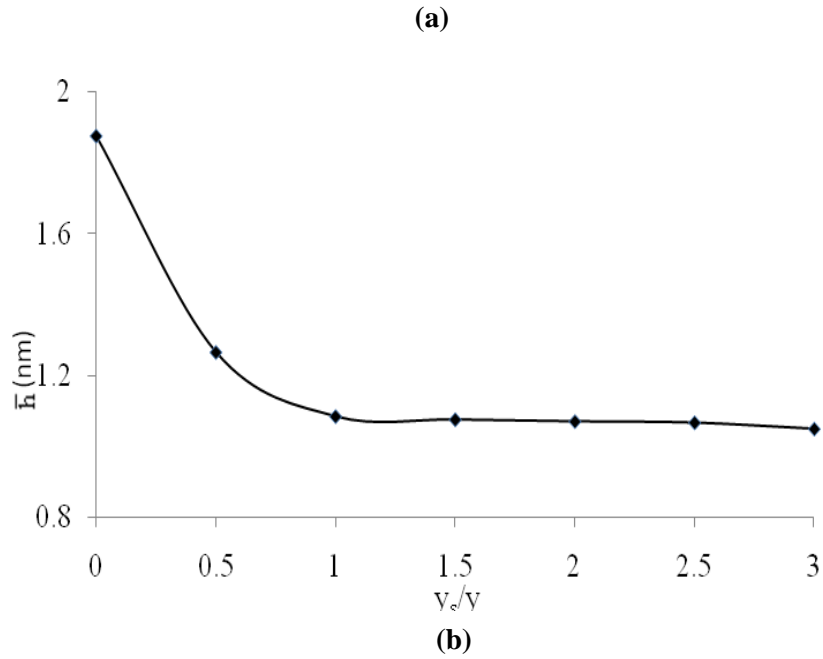
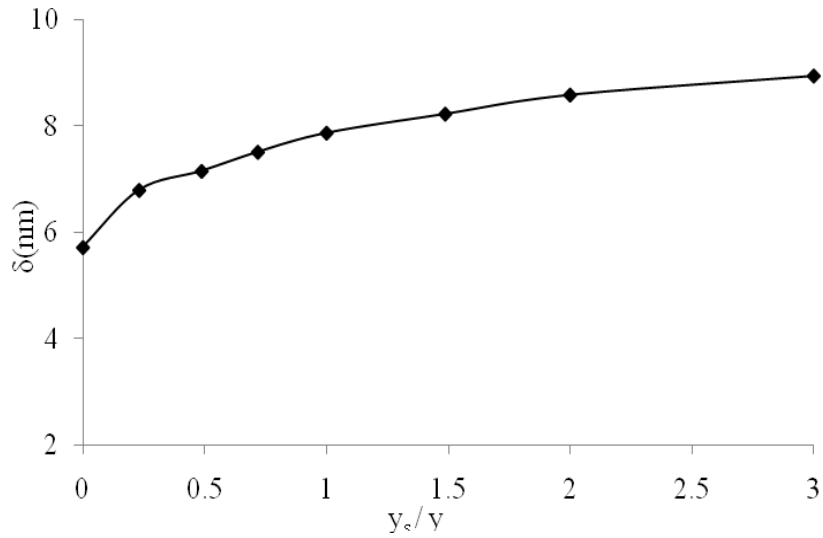


Figure 4.13. Average inter-island distance (a) and average island height (b) as a functions of the binding energy ratio (y_s/y) at $T=300$ K, for $t=30$ sec, $R=0.086$ ML/sec, $y=0.39$ eV.

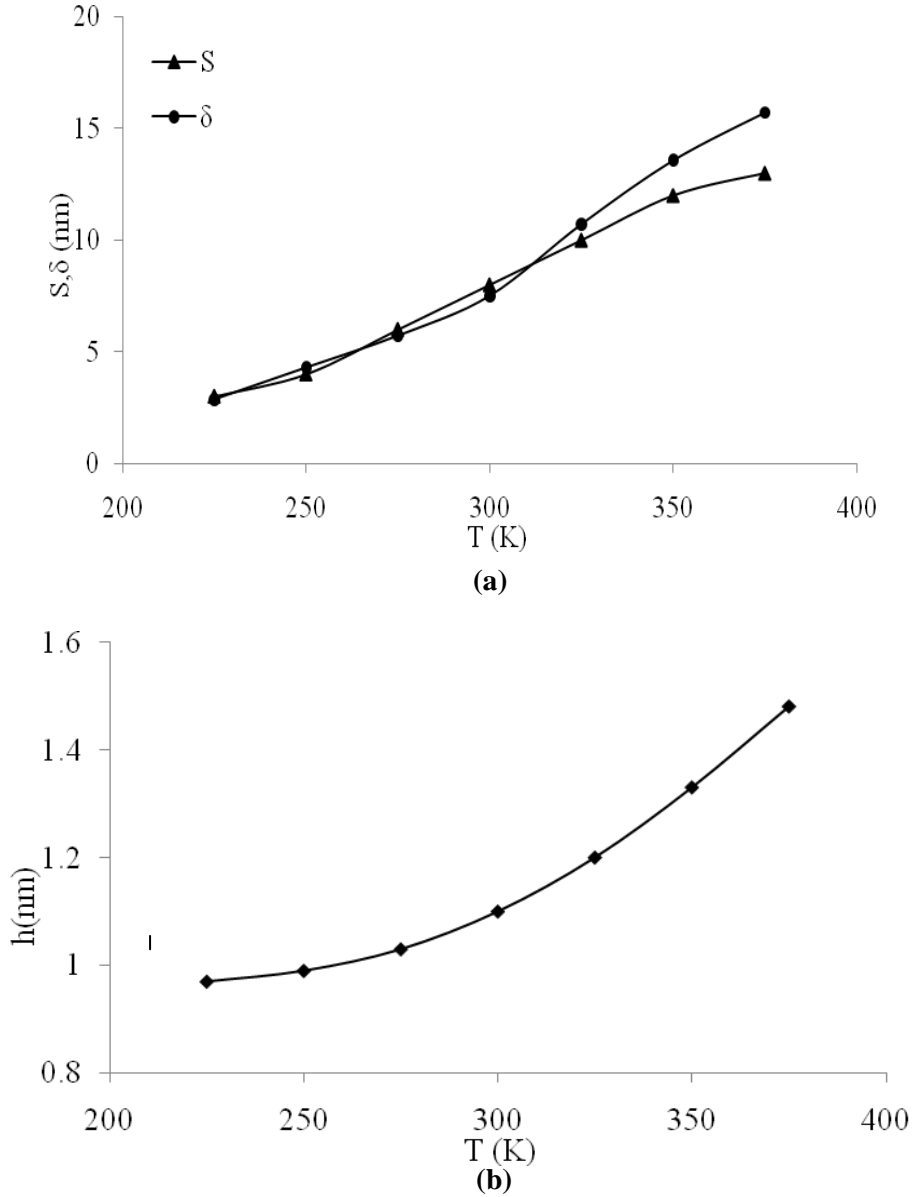


Figure 4.14. Average island size and inter-island distance (a) and average island height (b) as functions of temperature (T), at $t=30$ sec, $R=0.86$ ML/sec, $y_s=y=0.39$ eV.

The trend seen in Fig. 4.11(a) of the distances δ increasing faster than the estimated lateral size S at high temperatures is also an indirect consequence of the

island's coarsening. In order to maintain an equilibrium shape, large islands formed at higher temperatures tend to grow in height (Fig.4.11(b)) resulting in relatively distant NCs separated by uncovered surface; see also the high-temperature morphologies in Fig. 4.8(a,b).

Fig.4.12 presents the density of islands as a function of temperature for three different values of y_s . As one could expect, all the dependencies show that a lower number of islands per unit area are observed at higher temperatures. The graph also shows that a crossover of two Arrhenius-like regimes with different activation energies exists similar to the predictions of the 2D model [111, 112] and experimental results [31, 53, 55]. This crossover is attributed to the increasing impact of reversible jumping at increased temperatures. At lower temperatures, the nucleation and growth of NC's is an irreversible process, whereas at higher temperatures, thermally activated bond breaking events occur more often and the transition from largely irreversible to reversible (e.g. somewhat slower) islands growth takes place. Fig. 4.12 shows the average density of islands as a function of temperature ($1000/T$) for $t=30\text{sec}$, $R=0.86\text{ ML/sec}$, and three different values of y_s . Symbols represent the numerical results and lines show the Arrhenius approximations.

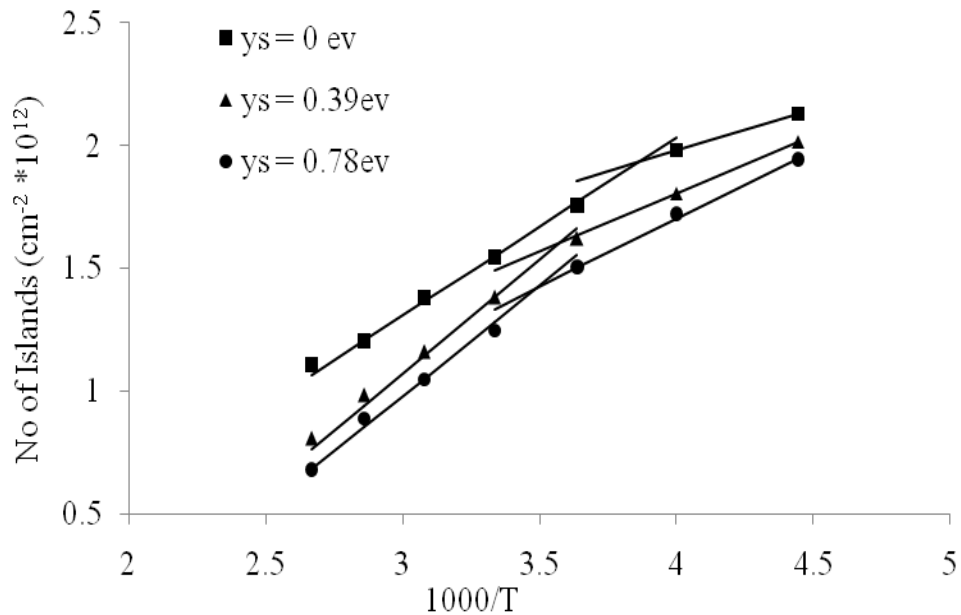


Figure 4.15. Average density of islands as a function of temperature ($1000/T$) for $t=30$ sec, $R=0.86$ ML/sec, and three different values of y_s . Symbols represent the numerical results and lines show the approximate slopes.

Fig.4.12 also illustrates the effect of binding energy on the crossover temperature T_x . With $y_s=0$, the crossover occurs at $T_x = 255$ K, at $y_s=0.5y$, $T_x = 272$ K (not shown); at $y_s=y$, $T_x = 278$ K; and at $y_s = 2y$, $T_x = 285$ K. Thus, increasing the ratio y_s/y from 0 to 2 shifts the crossover temperature from 255 K to 285 K. The observed increase of T_x with y_s can be explained by higher substrate binding energies impeding the reversible bond breaking process, thereby shifting the stronger coarsening regimes towards higher temperatures.

4.2.4 Rotation of crystals

An interesting phenomenon that can be demonstrated by the modeling is the rotation of the NCs orientation depending on process parameters. Morphologies formed at lower temperature show an alignment along $[011]$ and $[0\bar{1}1]$ directions; whereas at higher temperature, developed crystals tend to rotate 45 degrees and be aligned along $[010]$ and $[001]$ directions. From Fig. 4.13, it is evident that when temperature changes there is a tendency of rotation. From Fig. 4.13, it is evident that due to temperature change, there is a tendency of crystal rotation.

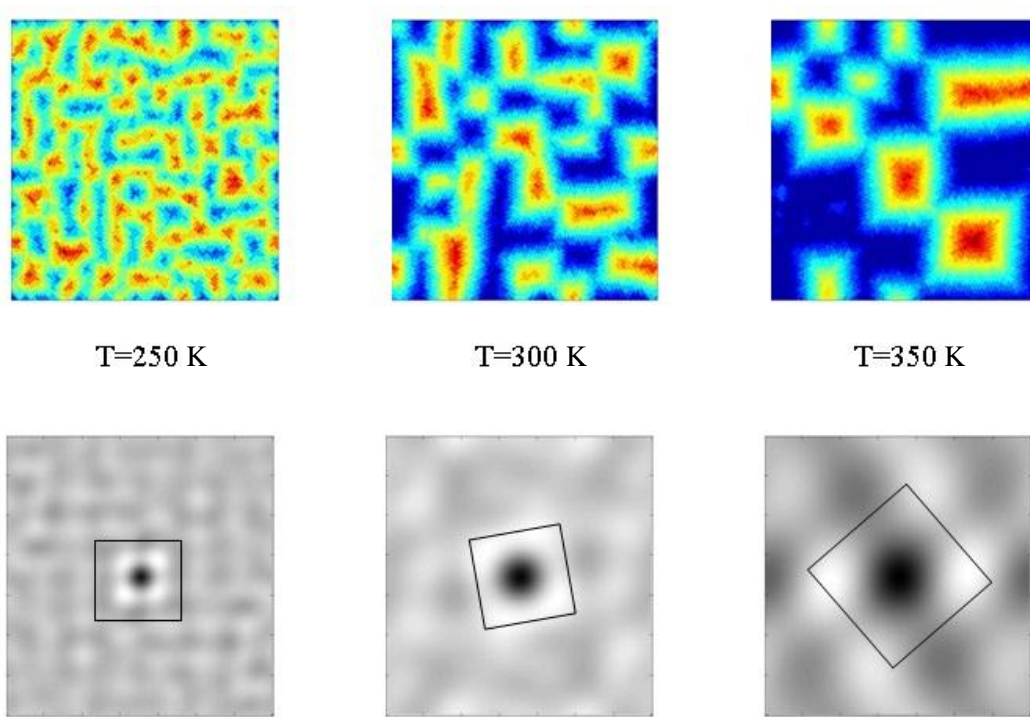


Figure 4.16. Rotation of crystal due to change in temperature. (Correlation function results are presented in inverse way for better visibility)

A change in texture and rotation of crystals has been observed in several experimental papers [115-118] and may be important for a number of applications [35, 119, 120]. Having the ability to predict the texture by varying the process parameters in the model can be a powerful tool for in silico process design.

4.3 Summary

In this chapter, I presented a 3D lattice based solid-on-solid KMC simulation of PVD synthesis of self-assembled metallic NCs on a crystalline substrate. The model of adatom mobility comprises reversible jumps between allowed FCC sites on a surface of a three-dimensional landscape. The surface wetting conditions can be varied by changing the energy of binding between adatoms and the substrate. The lattice 3D KMC approach described in this chapter has demonstrated a high level of flexibility to capture a complex interplay of the multitude of various factors on which the fabrication of NCs may depend. The model has been validated by comparison with benchmark experiments reported in literature, the analytical scaling laws, and simulations including the earlier 2D modeling of nanocrystalline synthesis.

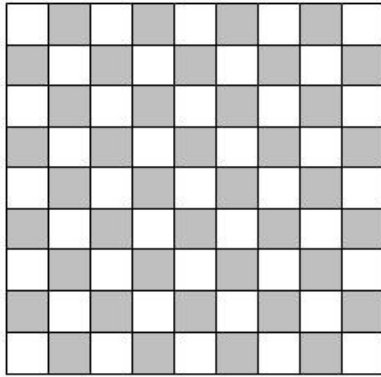
CHAPTER: FIVE

5 DEFECTS ANALYSIS

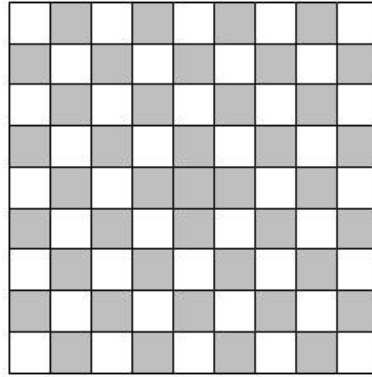
When studying nanocrystal synthesis, it is important to consider defects that may be present on substrates. The ideal crystal has an infinite periodicity of identical cells, whereas real crystals are limited in size, and they may have some disorder in stacking. The common defects on substrates can be classified as point defects, line defects and area defects [4]. Defects may arise spontaneously or be generated by external stress, strain and other influences. For simplicity, the external effects are not considered in this work. I consider hypothetical vacancy type defects in the model and represent the three major categories of defects by various combinations of the vacant sites. In this chapter, I introduce the defects in both 2D and 3D models and observe the effect of the defects on the morphology of the NC arrays.

5.1 Point Defects

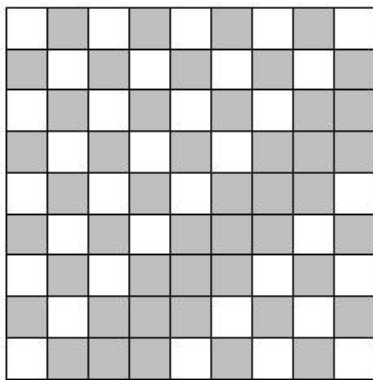
Three major types of point defects include vacancies, interstitials and impurities. They may arise during the original crystal growth, or be activated by heat. They also may be the result of other factors such as radiation etc. The most common types of defects are vacancies and they take place when atoms are missing in a crystalline lattice site.



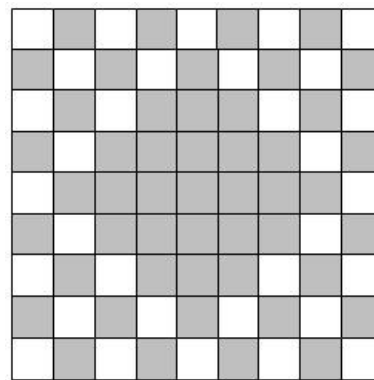
(a) Perfect crystal without defects



(b) Vacancy point defects



(c) Vacancy line defects



(d) Vacancy area defects

Figure 5.1. Examples of the hypothetical vacancy defects on the substrate: (a) perfect crystal without defects, (b) vacancy point defects, (c) vacancy line defects, and (d) vacancy area defects.

The point defects such as vacancies play a vital role in solid state diffusion, including recrystallization, grain growth, sintering and phase transformations. The concentration of point defects in a crystal is typically between 0.1% and 1% of the atomic sites at room temperature. However, in this work a higher amount of defects up to 10% is intentionally introduced in order to observe the effect clearly.

For the 2D model, the total number of allowed positions in the perfect FCC (100) substrate area of $100\text{nm} \times 100\text{nm}$ is 80089 (283×283). A detailed description of the model is available in chapter 3, Model 2. To create a vacancy type point defect, a position allowed for occupation is selected randomly and converted into a prohibited one. Thus, introduction of 800 vacant sites provides a 1% level of point defects. Various defect percentages are obtained by varying the number of the vacant sites in the model. In the 3D model, a similar approach of introducing defects on the substrate has been employed. The number of defects was 245 for an area of $25\text{nm} \times 25\text{nm}$ comprising the total of 4900 sites (70×70), which is 5% of the total number of sites. An important point is that the present model only considers defect sites on the substrate. Vacancies on the upper layers have not been considered.

From Fig. 5.2, it is evident that the introduction of point defects in 2D model has an effect on the morphology. Increasing of the amount of point defects results in a decrease of the average crystal size. With many defects, crystals break down and do not form well defined islands. In the 2D model, I only deal with the submonolayer deposition and thus the vacancy point defects have a profound effect on NC size and shape.

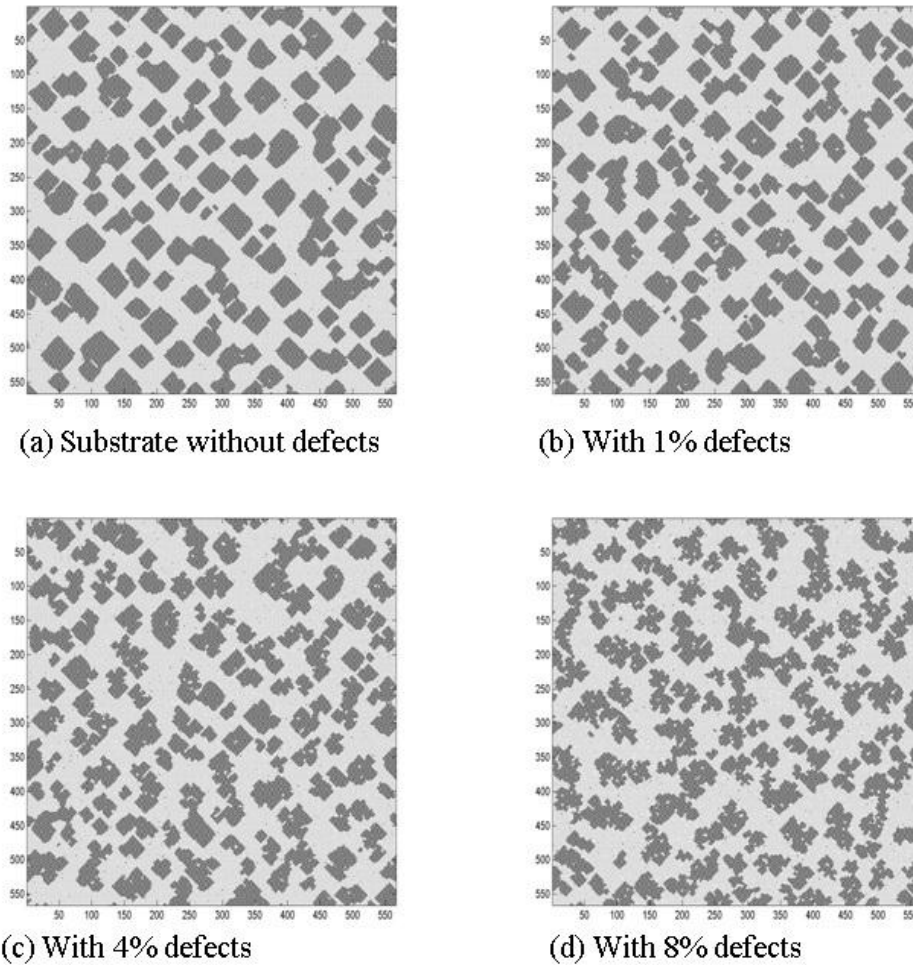


Figure 5.2. Vacancy point defects in 2D model of a NC array: (a) nanocrystalline array on the original substrate without defects, (b) nanocrystalline array on a substrate with 1% defects, (c) nanocrystalline array on a substrate with 4% defects, and (d) nanocrystalline array with 8% defects.

Fig.5.3 illustrates the effect of vacancy point defects in the substrate on the 3D morphology of a nanocrystalline array. With 5% defects, the effect is not significant; however, with 10% defects a slight increase in inter-island distance is

observed. In the 3D model, the presence of vacancy point defects on the substrate is less significant than in 2D model. The reason might be that after multilayer deposition, when more than 2ML is deposited, the effect of point defects at the substrate is decreased in the upper deposited layers.

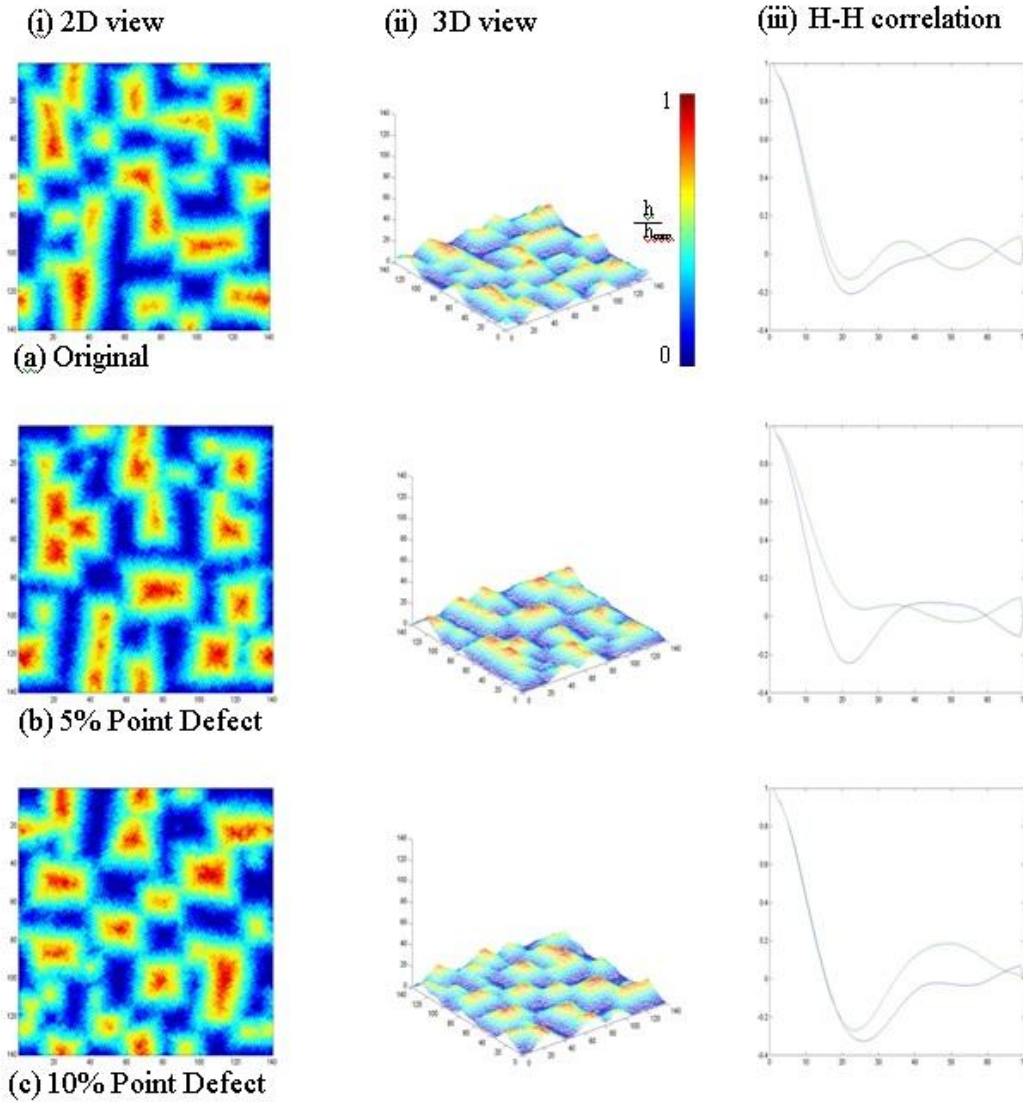


Figure 5.3. Vacancy point defects in the 3D model of a NC array. The 2D view, 3D view and the height-height correlation functions of (a) original substrate without defects, (b) substrate with 5% defects, and (d) with 10% defects.

To conclude, vacancy point defects have a pronounced effect on sub-monolayer crystal formation and are less important for multilayer 3D NC morphology.

5.2 Line Defects

To simulate line defects, I also consider the substrate with an FCC (100) crystal orientation. Then, an entire line of allowed locations is converted into vacancies. These artificial vacancy lines are used to analyze the effect of line defects in the model.

From Fig. 5.4, it is evident that the vacancy lines have an effect on the morphology. The line defects break the NCs acting as boundaries beyond which growing NCs do not extend. I explored this effect for various directions of the defects, [001], [010] and [011]. It appears that for the 2D model, the direction of the defects does not have any other influence than creating the boundary or breaking the integrity of growing NCs.

Fig.5.5 demonstrates the importance of vacancy line defects in the 3D model. Interestingly, both [010] and [001] line defects have a tendency to guide the 3D NC growth along the direction of the defects.

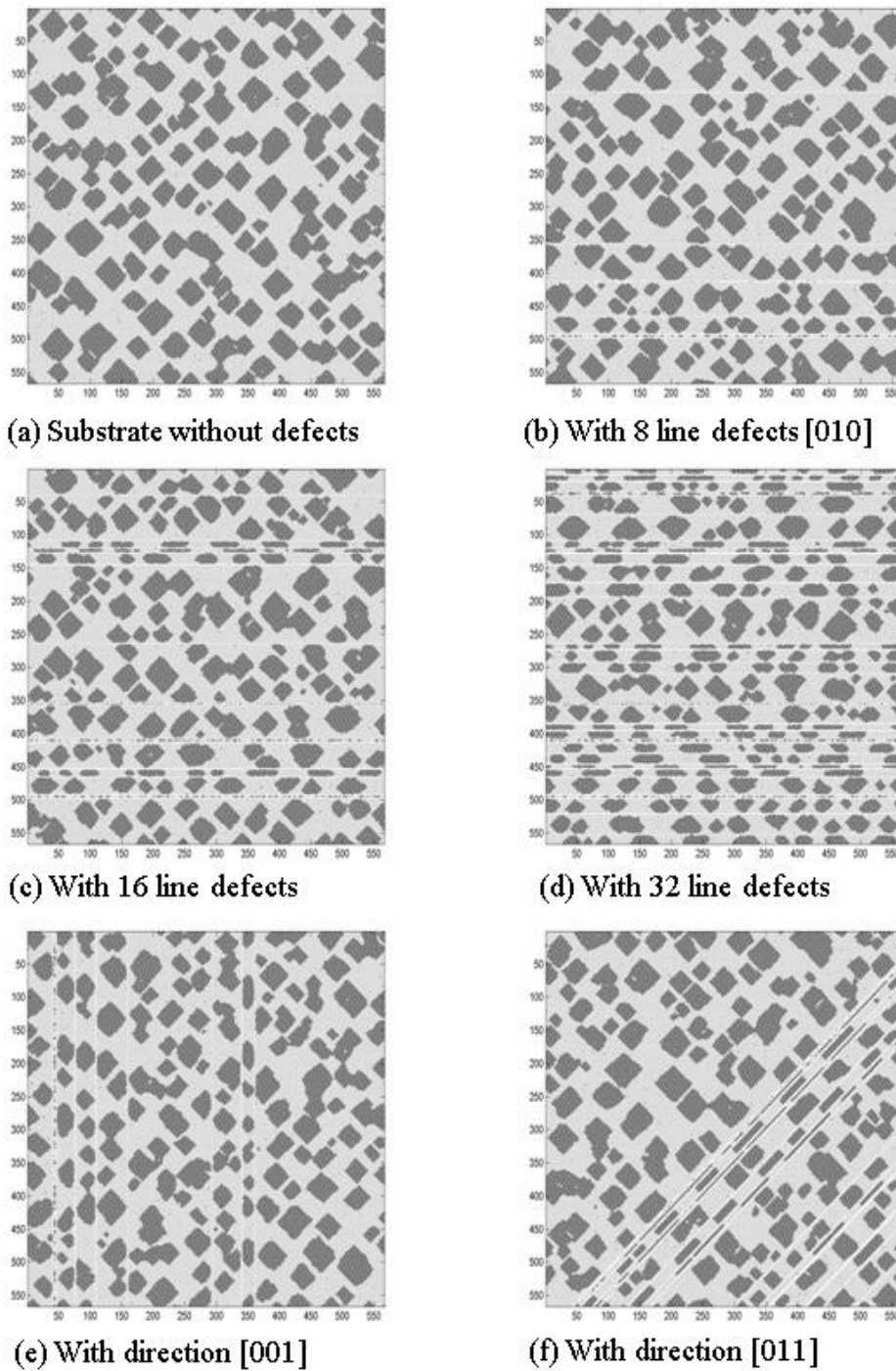


Figure 5.4. Vacancy line defects in the 2D model; (a) original substrate without defects, (b) substrate with 8 line [010] defects, (c) with 16 line defects, (d) with 32 line defects, (e) with [001] line defects and (f) with [011] line defects.

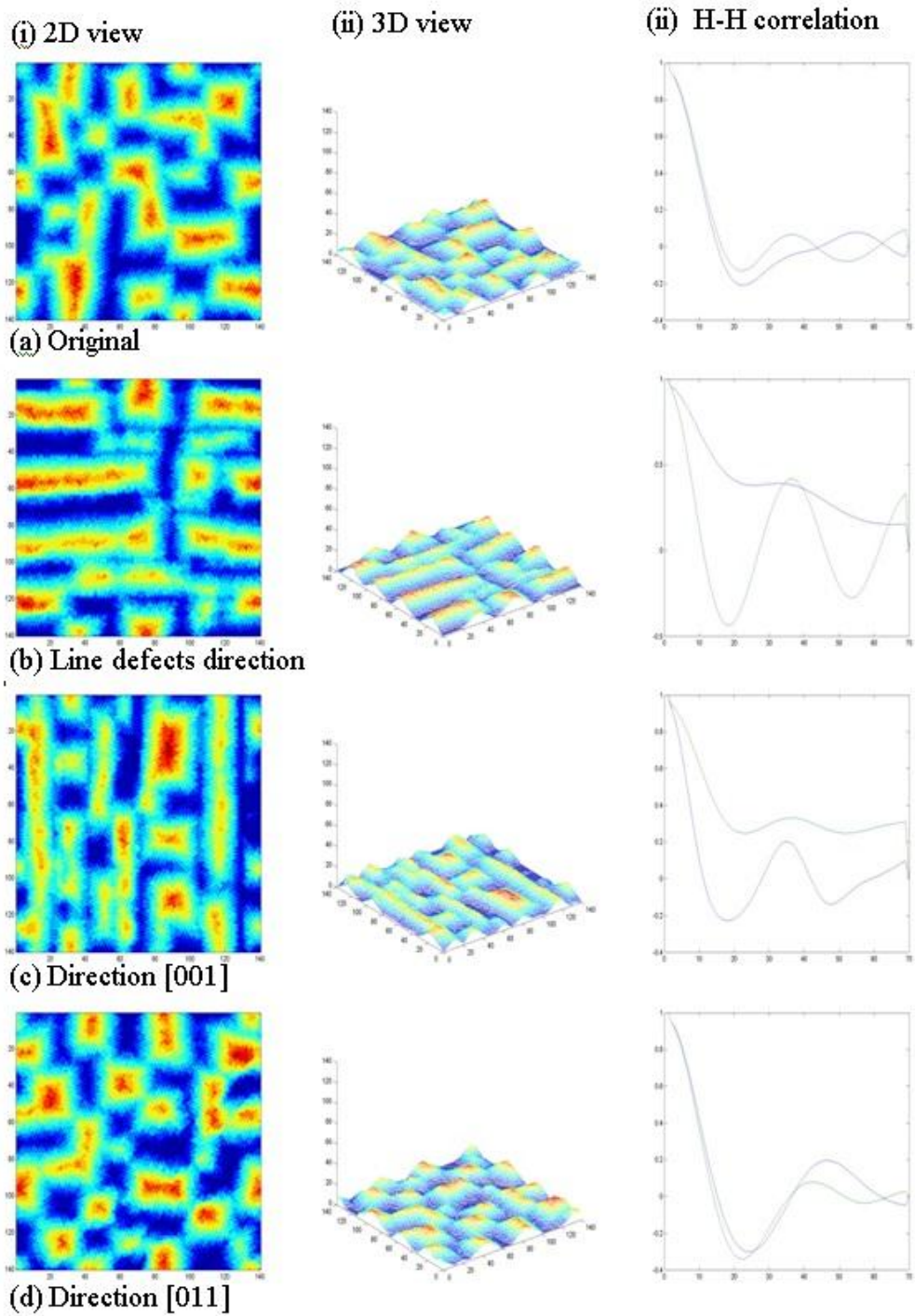


Figure 5.5. Vacancy line defects in the 3D model. The 2D view, 3D view, and the height-height correlation functions for: (a) original substrate without defects, (b) line defects in [010] direction, (c) [001] direction, and (d) [011] direction.

Both the morphologies and H-H correlation functions for [010] and [001] directions clearly show an affinity along the direction of the defects. However, defects in the [011] direction did not show a pronounced effect on the morphology. A conclusion can be made that by incorporating artificial defects, elongated quasi dimensional NCs can be produced. Fabricating NCs with a prepatterned substrate is an interesting field of study attracting a lot of attention[121-125].

5.3 Area Defects

To model area defects, a region of the substrate is randomly selected where atoms are forbidden to occupy. For this initial study, these defects have an area of approximately 1 nm^2 around the selected site, which corresponds to a total of 18 atoms. The area defects do not possess the FCC(100) structure such as the rest of the surface. Introduction of the artificial area defects breaks the homogeneous crystalline structure and introduces a discontinuity into fabricated NCs. The total number of area defects multiplied by the area of one defect gives the estimate of the total defects at the surface. Similar surface area defects have been implemented in the 3D model.

Fig.5.6 shows the effect of area defects on the morphology in the 2D model. Clearly, the increase in the amount of defects decreases the average NC size. With high defect densities, NCs break into fragments and form quite disordered arrays.

Since the 2D model represents submonolayer deposition, the effect of area vacancy defects is significant for both size and shape of the islands.

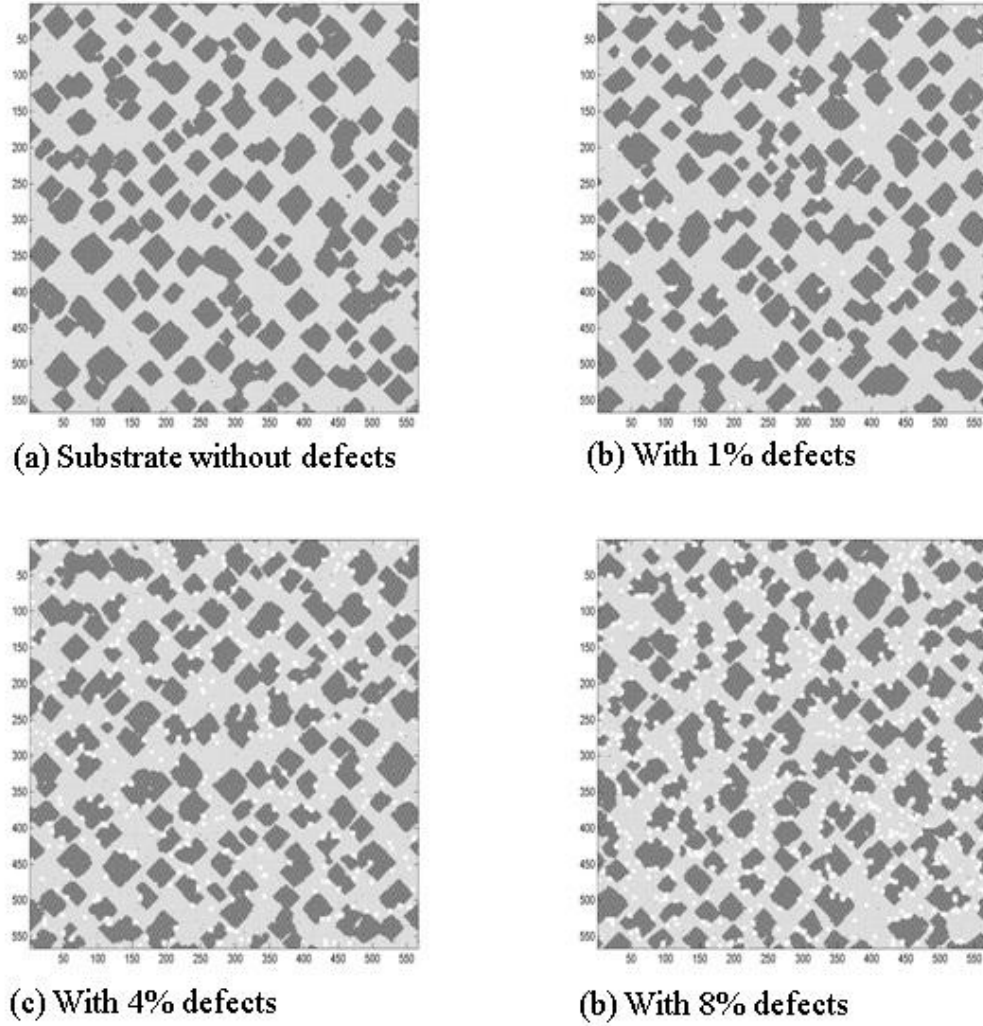


Figure 5.6. Vacancy area defects in the 2D model: (a) original substrate without defects, (b) substrate with 1% defects, (c) substrate with 4% defects, and (d) with 8% defects. The defects are indicated as white areas.

Fig.5.7 illustrates the effect of vacancy area defects in the 3D model. Increasing the amount of defects has a significant influence on the islands' shape and their separation. With many defects, crystalline shapes become less pronounced and a disordered array of uneven islands develops.

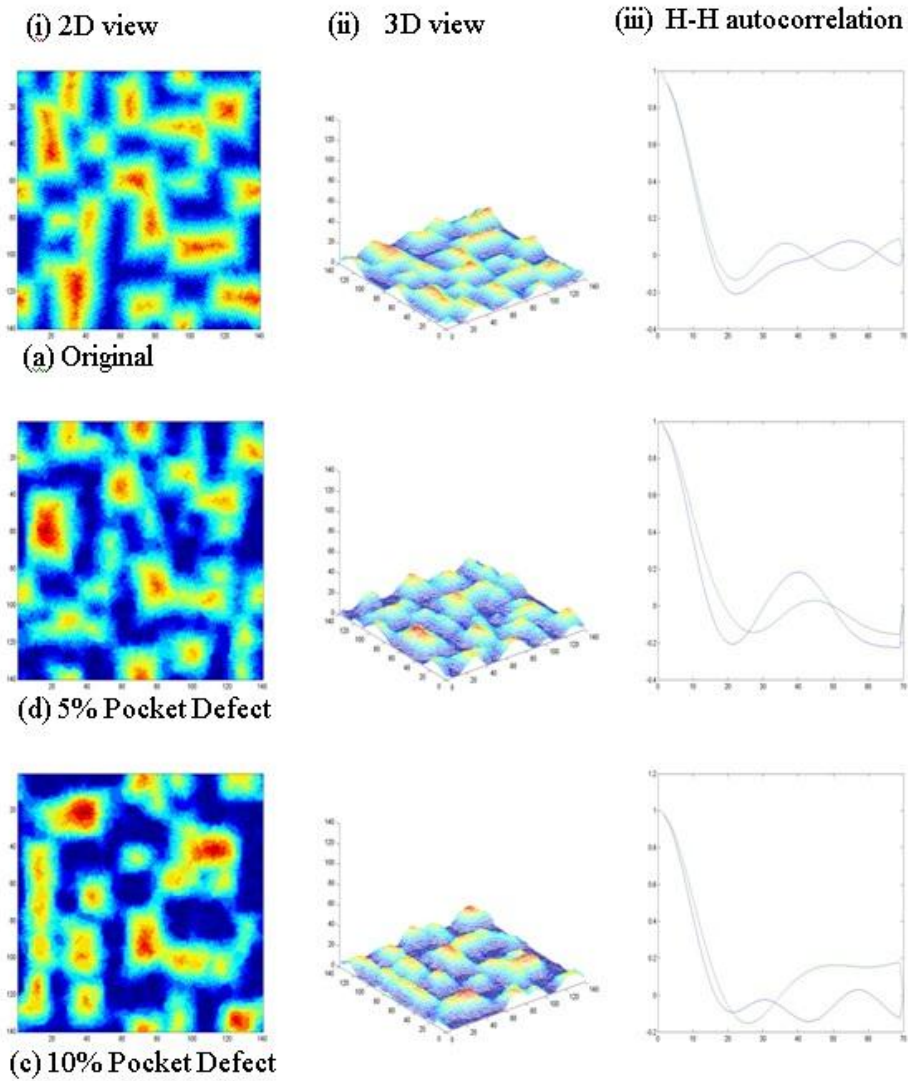


Figure 5.7. Vacancy area defects in 3D model: The 2D view, 3D view and the height-height correlation functions of (a) original substrate without defects, (b) substrate with 2.5% defects and (d) with 5% defects.

5.4 Comparative Analysis of Defects' Influence

In Fig. 5.8, the effect of various defects on NC size is compared for the 2D model. It is evident from Fig. 5.8 that area defects have a more profound impact on the size than line and point defects.

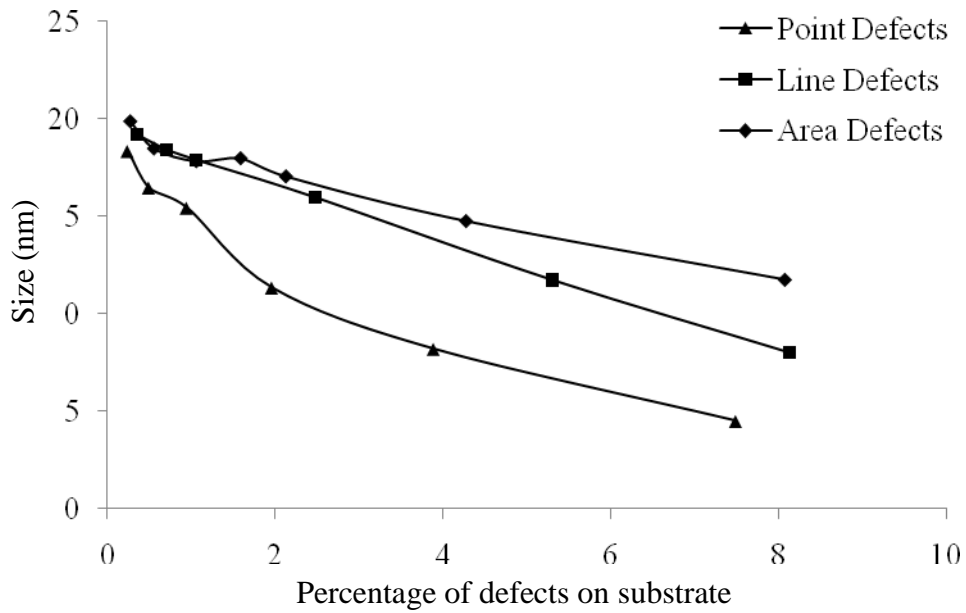


Figure 5.8. Comparison of the effect of various defects on NC size with increasing defects in the 2D model.

The common trend is that the increase of the amount of defects decreases the size of the islands, which can be attributed to the obstruction of the adatoms' surface mobility, resulting in slower NC growth.

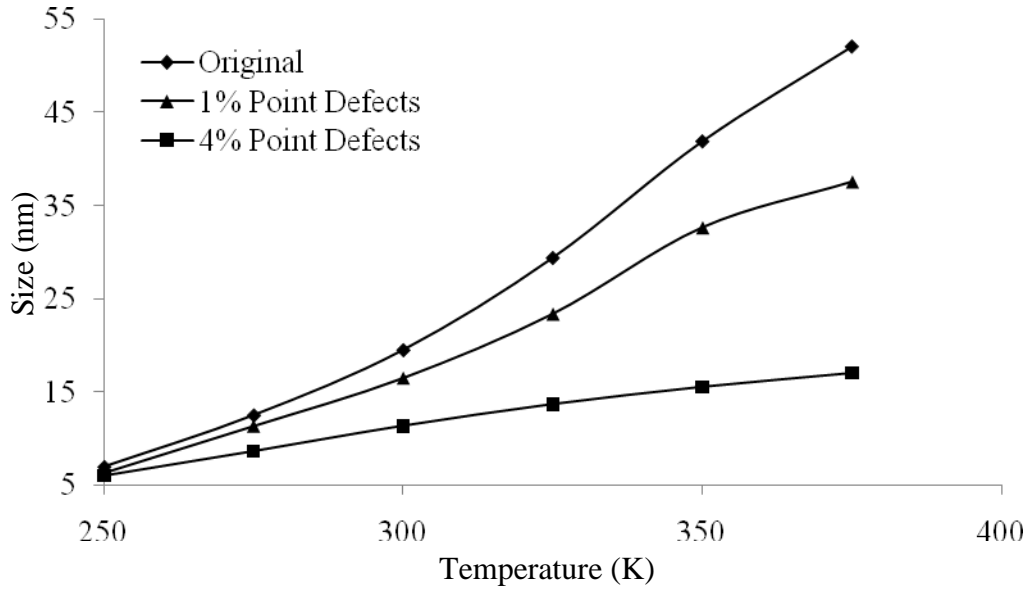


Figure 5.9. Effect of point defects on the temperature dependence of NC size in the 2D model.

In previous chapters, it has been demonstrated that NC size strongly depends on the substrate temperature. Fig. 5.9 shows the influence of the presence of point defects on the temperature dependence of NC size in the 2D model. It is evident from the graph that NC growth on the imperfect surface is slower at all temperatures, and the impact increases with the amount of the defects.

Fig.5.10 further illustrates how the morphology changes when temperature is varied in the 3D model with 5% point defects at the substrate. At varied temperatures, the results of the 3D model are not much affected by the presence of point defects at the substrate. Maybe the defects on substrate got buried under the deposited material and did not effect on the grown morphology.

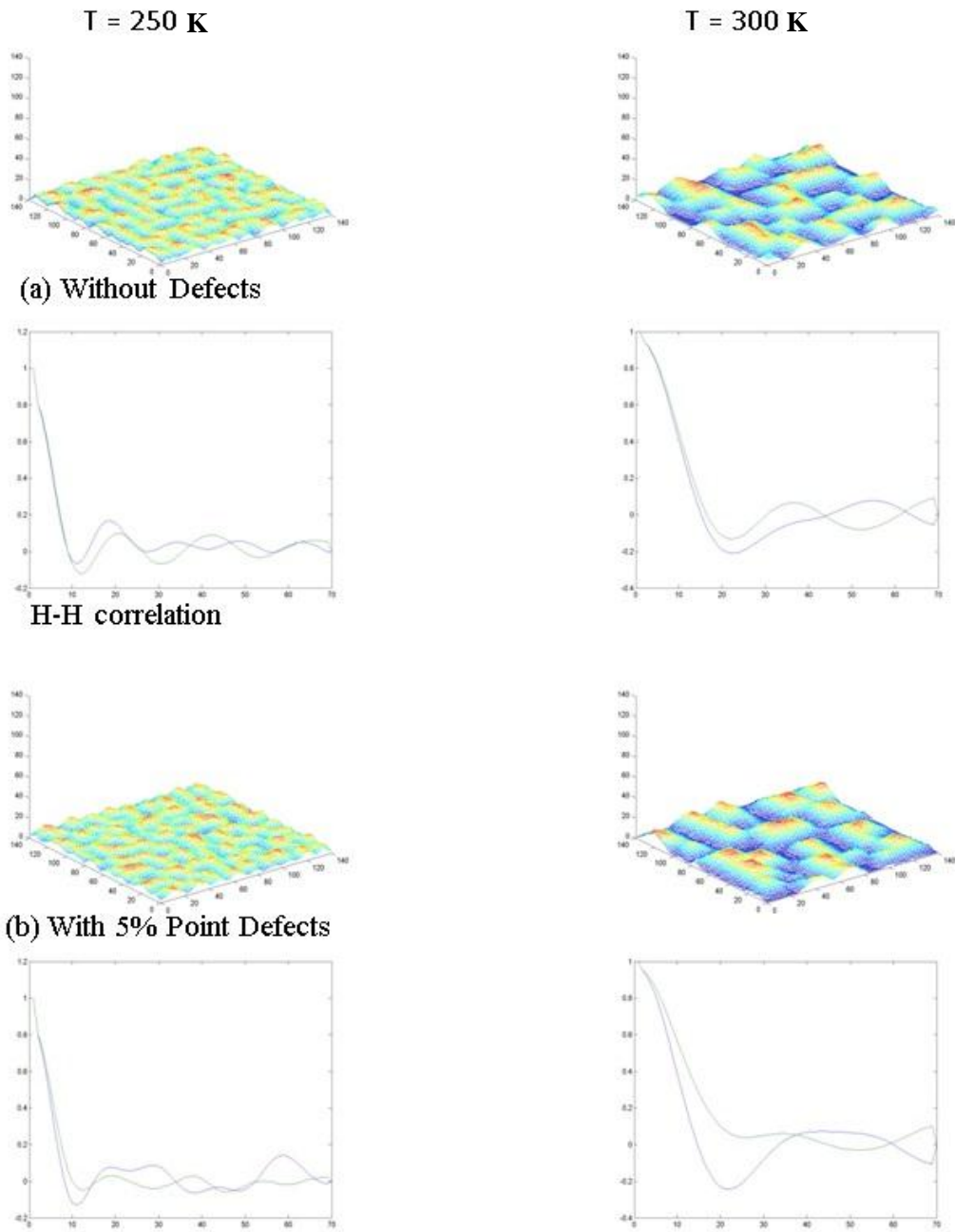


Figure 5.10. Effect of temperature on the 3D morphology: (a) original substrate, and (b) in the presence of 5% point defects.

Fig.5.11 shows that the coarsening at higher temperatures also has less effect in the 3D model for size and distance of NCs when the line defects and the area defects are introduced.

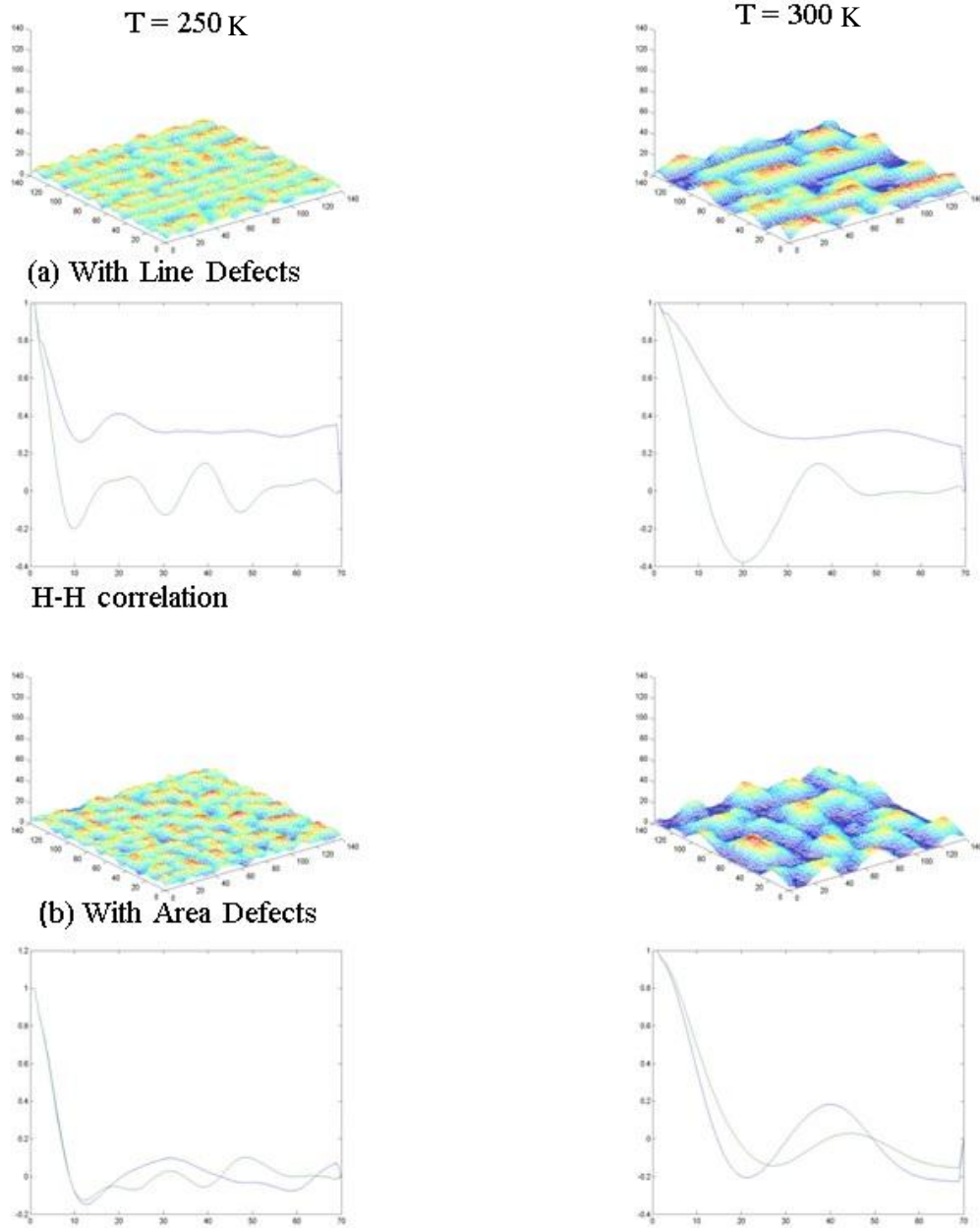


Figure 5.11. Effect of temperature on the 3D morphology (a) with line defects and (b) with area defects.

5.5 Summary

Defects are integral part of crystalline solids. Here, I have investigated the effect of hypothetical vacancy type defects in both 2D and 3D KMC models. I observed that the presence of defects affects the size and shape of the NCs simulated, and the influence is more pronounced in the 2D model than in the 3D one. The reason might be that 2D model addresses submonolayer surface morphologies for which substrate defects play an important role. In the 3D model, once the film has bridged the substrate defect, it no longer influences subsequent growth. Line defects in the 3D model acted as templates to produce aligned elongated NCs. The presence of defects was also found to decrease coarsening of NCs at higher temperatures. The modeling results confirm that patterned substrates might help to generate desired shapes of nanoparticles and control the pattern texture. Having the capability to incorporate the defects analysis in the NC simulation process makes the model more flexible to handle imperfect surfaces.

CHAPTER: SIX

6 OFF-LATTICE MODEL

In the previous chapters, I have described simulations of NC synthesis using lattice based models. The assumption in lattice based models is that the substrate determines the structure where deposited atoms can occupy only predefined locations. Although atoms are permitted to jump randomly allowing the simulation of realistic phenomena of NC formation, a particular atom can only occupy a specific location in the FCC structure, and inter-atomic distances remain always constant throughout the structure. Such lattice based models provide strong capability to mimic the atomistic behaviour, but in a simplified manner. What really happens to atoms during PVD deposition is somewhat more complex. Atoms do not follow any coordinated predefined structure during NC formation, rather inter-atomic potentials define their exact locations and the probability of the corresponding jumps is based on the activation energy. As the sole objective is to develop models to simulate NC fabrication by PVD methods, in this chapter, I explore another type of stochastic model based on inter atomic potentials which I denote as the off-lattice model. The proposed model does not restrict an atom within the coordinated predefined structure. Rather, in this model a newly added atom is free to settle down in a position equal to lattice constant or greater or less than that distance. The criteria of finding a new location depend on the minimum energy location of the added atom comparing its entire neighbours within the search distance specified by the model.

6.1 The Model Description

The proposed off-lattice model is based on a detailed interaction potential and an atom can settle down on a substrate anywhere corresponding to a minimum value of the potential within its search area of interaction specified by the model. Fig. 6.1 describes the structure of the on-lattice and off-lattice model types.

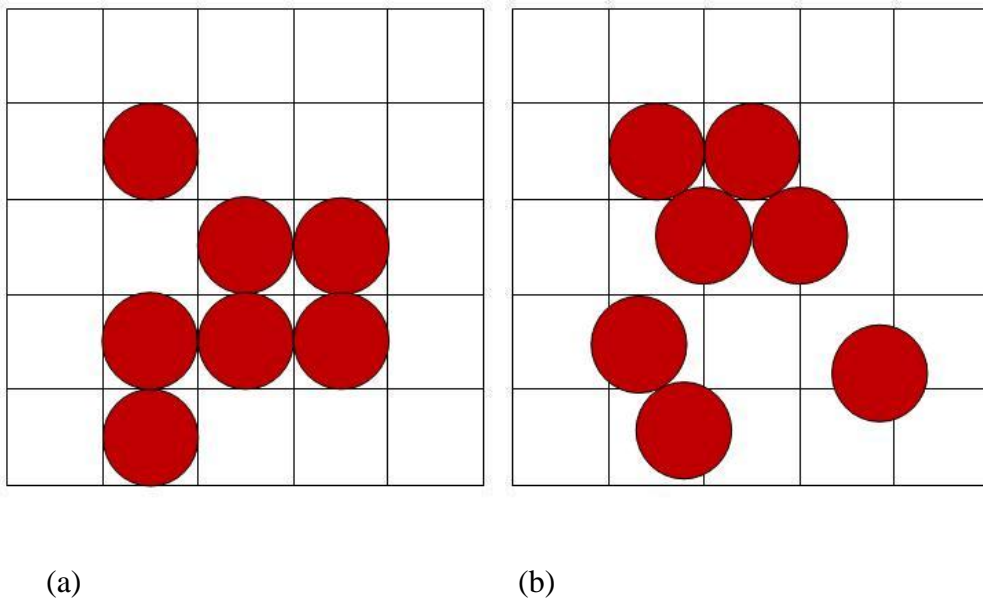


Figure 6.1. (a) Lattice based model structure and (b) off-lattice model structure.

Fig.6.1(a) shows the lattice based model in which atoms are constrained within the specified grid of the model prescribed and Fig. 6.1(b) shows the off-lattice type of model where atoms are not restricted within the specified coordinates of the model. In my implementation, the off-lattice model does employ a grid to facilitate local searching, but the grid does not constrain atom placement.

Each cell may contain multiple atoms but is sized to be approximately the scale of the interaction distance; as such, a cell may contain one full atom or be attributable to fractions of multiple atoms. Similar to the lattice model, both 2D and 3D versions have been implemented for the off-lattice simulation.

6.1.1 Inter atomic potential

In the lattice based model, I used cohesive energy to determine bond energy and employed the same bond energy to calculate the probability of an atom jumping to a new position. In the off-lattice model, I used the pair inter-atomic potential to determine the minimum potential location corresponding to the occupation within the search radius. For simplicity, I used the Lennard-Jones potential to calculate the inter-atomic potential. The Lennard-Jones potential, also referred to as the (6-12) potential, is a mathematically simple model to describe the interaction between a pair of atoms. In future, other potential models such as the Johnson's embedded-atom method (EAM) or other interaction potentials could be used in this off-lattice simulation. The most common expression of the L-J potential is [105, 106, 126]:

$$V_{LJ} = 4\varepsilon \left(\left(\frac{\sigma}{r} \right)^{12} - \left(\frac{\sigma}{r} \right)^6 \right) = \varepsilon \left(\left(\frac{r_{min}}{r} \right)^{12} - 2 \left(\frac{r_{min}}{r} \right)^6 \right). \quad 6.1$$

Here ε is the potential well depth, which for Cu can be estimated $\varepsilon=0.3\text{eV}$ [106], r is the distance between the atoms, σ is the distance where the potential (V_{LJ}) is equal to zero, and r_{min} is the distance at which the potential function reaches the minimum, which can be expressed as $r_{min} = 2^{1/6}\sigma$. In the present simulation, r_{min}

$\approx 0.25 \text{ nm}$ [106]. The L-J potential provides a reasonable estimate to describe the interaction of adatoms at a surface for PVD simulation [105, 106, 127, 128]. Multi body interaction potentials such as EAM [101, 102, 104] can also be employed; however, this complicates the task and increases the simulation time. Due to its computational simplicity, the Lennard-Jones pair potential is used extensively in computer simulations.

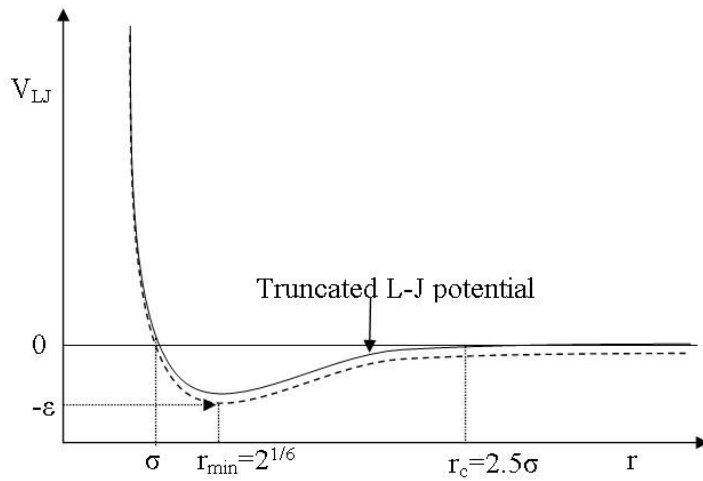


Figure 6.2. A graph of strength versus distance for the Lennard-Jones potential.

To save computational time, the Lennard-Jones potential is often truncated at a cut-off distance of $r_c = 2.5\sigma$, where $V_{LJ}(r_c) = -0.0163 \varepsilon$. Beyond r_c , the truncated potential is set equal to zero. To avoid a sharp step at distance r_c , the LJ potential is shifted upward so that the truncated potential would be zero exactly at the cut-off distance. The resulting truncated Lennard-Jones potential V_{trunc} is defined as follows:

$$V_{trunc}(r) = \begin{cases} V_{LJ}(r) - V_{LJ}(r_c) & \text{when } (r \leq r_c) \\ 0 & \text{when } (r > r_c) \end{cases} \quad 6.2$$

By definition, $V_{trunc}(r_c) = 0$, thus eliminating the jump discontinuity at $r = r_c$.

6.1.2 Minimization method

During the PVD process, an adatom positions itself on the substrate based on the global and local minimum on its potential energy surface. In the off-lattice model, I used an energy minimization process to compute the equilibrium configuration of all neighbouring atoms within the search area of 2.5σ . Energy minimization employs an optimization of the system to move atoms by reducing the net forces on them until the forces become negligible.

I used the conjugate gradient method [129-131] to perform energy minimization. The conjugate gradient method is an efficient, iterative method and often used for solving partial differential equations; as such, it is one of the best choices for the potential minimization in the model. In the simple gradient method, the solution progressively follows the direction of steepest descent until the minimum value is reached. However, convergence using this method can be slow, especially for deep potential ‘valleys’. The conjugate gradient method improves on this by introducing orthogonal elements to the descent direction. For a function f of N variables, the gradient ∇f indicates the direction of maximum increase. The steepest descent method with an adjustable step length performs a line search to

reach the minimum. After this first iteration, the following steps implement an iterative move along a subsequent descent direction. To apply the conjugate gradient method, I calculate total potential contribution from all neighbors within the search radius as follows:

$$\phi = \sum_{r=2.5\sigma} V_i(r) . \quad 6.3$$

The minimum of a function is obtained when $|\nabla \phi| = 0$.

The gradient $\nabla \phi$ is expressed through the derivatives of the potential function:

$$\nabla \phi = \sum \nabla V , \quad 6.4$$

$$\nabla V = \frac{\partial V}{\partial r} \frac{\partial r}{\partial x} x + \frac{\partial V}{\partial r} \frac{\partial r}{\partial y} y + \frac{\partial V}{\partial r} \frac{\partial r}{\partial z} z , \quad 6.5$$

where $r^2 = x^2 + y^2 + z^2$ and $2rdr = 2xdx + 2ydy + 2zdz$. Because the Lennard-Jones potential is spherically symmetric, the functional form of the three terms is the same and is efficient to compute. The procedure starts with calculating the steepest direction, and then computes the conjugate direction using the Polak–Ribière formula [132, 133]. Then a line search is performed to find a minimum and the position updated. The procedure repeats until the minimum is found.

The model works on the principle described in Fig. 6.3 which shows the process of finding the minimum point on surface (a), the option of multiple minima in a cell (b) and the choice of nearby minimum within the search radius of r_c to which to jump (c) based on the same probability function described in earlier models.

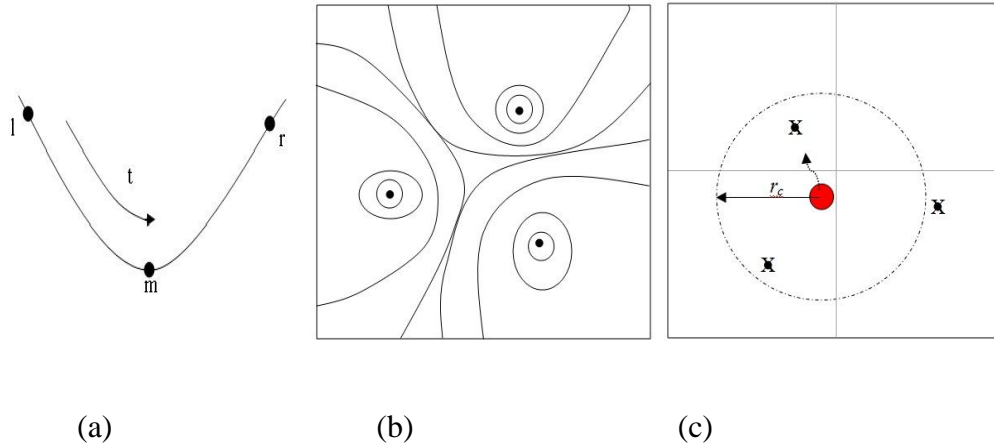


Figure 6.3. (a) Finding the minimum; (b) multiple minima within a cell; (c) selecting the appropriate minimum point and based on jump probabilities using the metropolis algorithm (eq.3.4).

The minimization routine checks all atoms within its search radius and computes the interaction potentials using potential calculation considering all neighbouring atoms. Based on the list of nearby atoms, it computes minimum locations and the corresponding potentials. Minimization of the function based on a 1D solver along the direction is used to find the minima. The 1D solver first finds 3 points straddling a minimum as a function of parameter t (see Fig. 6.3 (a)). The parameter t expands dynamically to ensure $f_m < f_l, f_r$.

6.2 Simulation Process

Fig.6.4 shows the stochastic simulation process flow chart. At the beginning of the simulation cycle, deposition rate and diffusion rate go through a probabilistic determination stage where the rate of deposition and rate of diffusion are compared with a random number to decide which process to follow. With a higher deposition rate, chances of adding a new atom during this step are high and more atoms are added to the simulation. At higher temperature when diffusion rates are high, each adatom follows a prolonged sequence of annealing steps. These deposition and diffusion processes continue until the break point is reached. The break point can be any desired end criteria such as time elapsed, atoms added or target film thickness reached, etc. Each cell contains a list of sites of the locations of minima in the energy function. These are locations where depositing atoms will be added or to which diffusing atoms could potentially jump. Due to the process of deposition and diffusion, a change in potential level of all the neighbouring atoms takes place. A transition list tracking each possible jump must be updated every time an atom is added or moved in the vicinity.

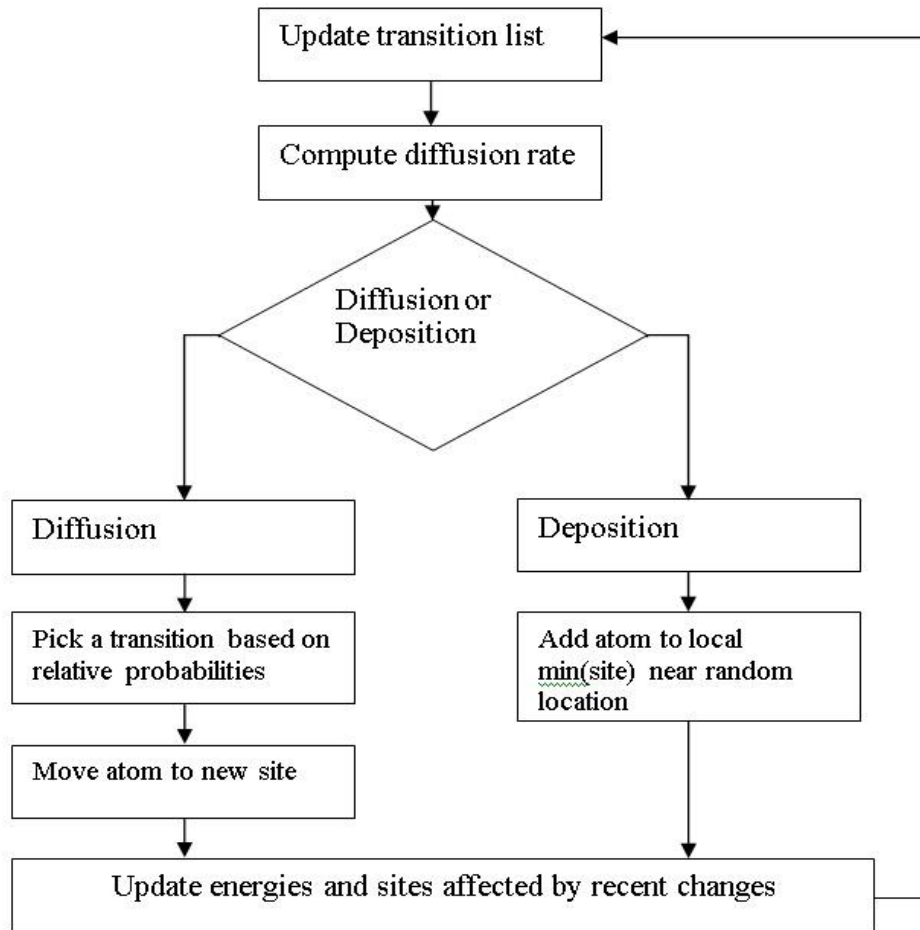


Figure 6.4. Process flow diagram of the off-lattice model.

6.2.1 Boundary conditions

Periodic boundary conditions are applied the same way of lattice based mode does. For 2D model the boundary conditions are applied in both “x” and “y” directions and for the 3D model in “x” and “y” directions but not in the “z” direction.

6.2.2 Substrate potential treatment

Unlike the 2D lattice based model where I omitted the substrate binding energy for simplicity, in the off-lattice model I employ a periodic or randomized potential to represent crystalline or amorphous substrates, although an idealized homogeneous substrate can also be used.

6.3 Monolayer Off-lattice Model (2D Mode)

I carried out simulations for $12.5\text{nm} \times 12.5\text{nm}$ area and assumed minimum inter-atomic distance to be 0.25 nm . Figure 6.5 (a) shows the search grids and potential minima position by “x” marks. The shown grid exists only to simplify searching. In the rest of the discussion the grid is not shown for simplicity.

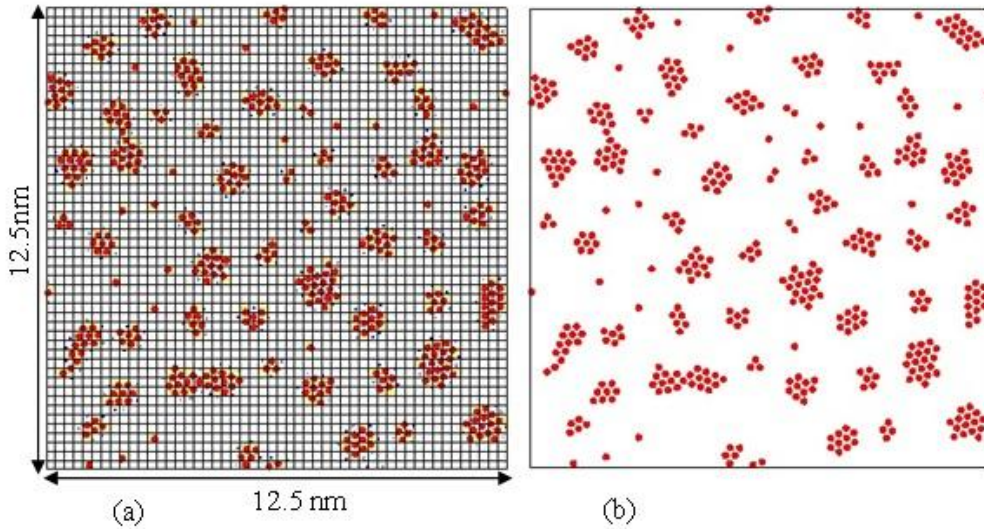


Figure 6.5. 2D off-lattice simulation results for $12.5\text{ nm} \times 12.5\text{ nm}$ area. (a) With corresponding search grids and potential minima location and (b) without the grid or minima position shown.

6.3.1 Evolution of surface morphology due to constant deposition

I carried out simulation of the deposition process with constant deposition rate and investigated the corresponding changes in surface morphology. Fig. 6.6 shows the change in morphologies due to continued deposition. I observe that tiny NCs form on the surface and grow in size as the deposition continues. Mature 2D clusters start merging over the time and form a thin film.

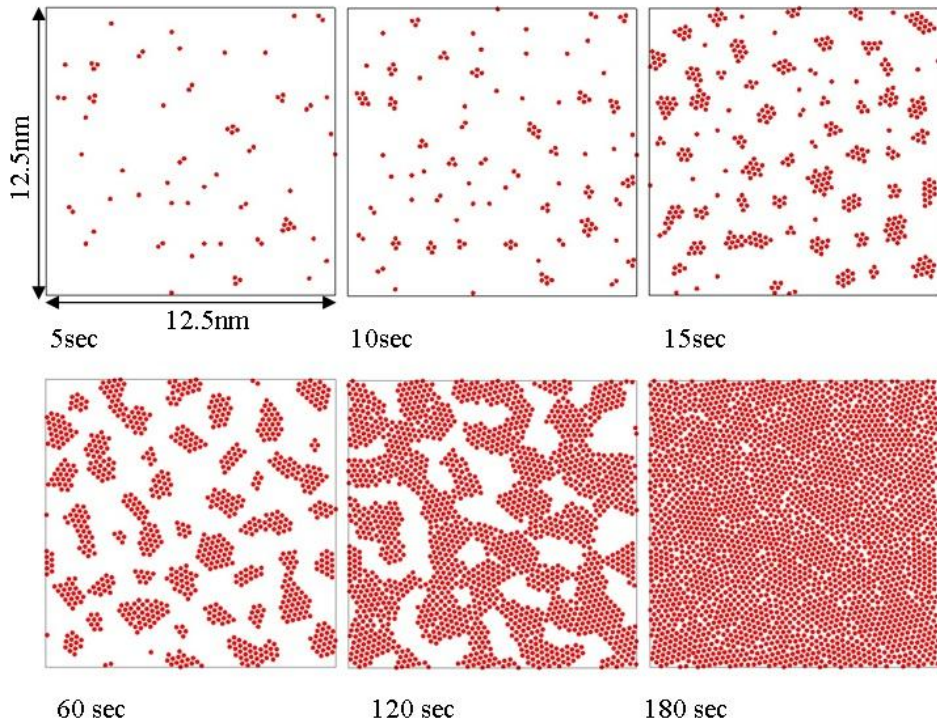


Figure 6.6. Simulation of $12.55 \text{ nm} \times 12.5 \text{ nm}$ area at various times (5-180 sec) at $R=0.006 \text{ ML/sec}$ and $T=300 \text{ K}$.

An interesting phenomenon is found for 180 sec deposition where an almost continuous thin film with grain boundaries is formed. The grain boundaries could

only be observed in the present off-lattice model without periodic substrate potential. Lattice based models or off-lattice model with substrate potential did not result in grain boundaries. At this stage, the NC growth would occur on multiple layers rather than in 2D.

6.3.2 Effect of deposition rate

Lattice based models have demonstrated that deposition rate plays a vital role in determining the size, density and distance of the fabricated NCs. I apply the similar conditions of constant time and constant coverage deposition processes to determine the off-lattice model behaviour.

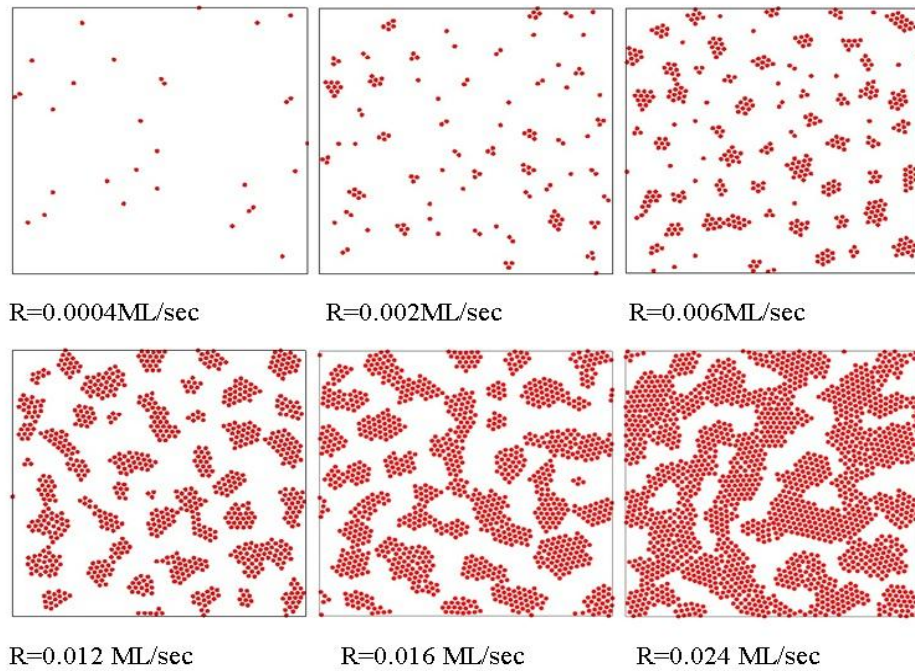


Figure 6.7. Simulation for constant time of 30 sec at various deposition rate $R=0.0004 \text{ ML/sec}$ to $R=0.024 \text{ ML/sec}$, at $T=300 \text{ K}$

Fig.6.7 shows the effect of deposition rate for constant time. It can be seen that increasing R raises the number and size of the islands. In the lattice based model the island sizes remained quite steady for certain range of deposition; however, in the off-lattice model the steady size regime is short. The behaviour observed by changing the deposition rate at constant coverage is shown in Fig. 6.8. With low deposition rate for longer deposition time, larger islands are produced, and at higher deposition rate and shorter time the size becomes smaller which is consistent with results obtained with the lattice based model.

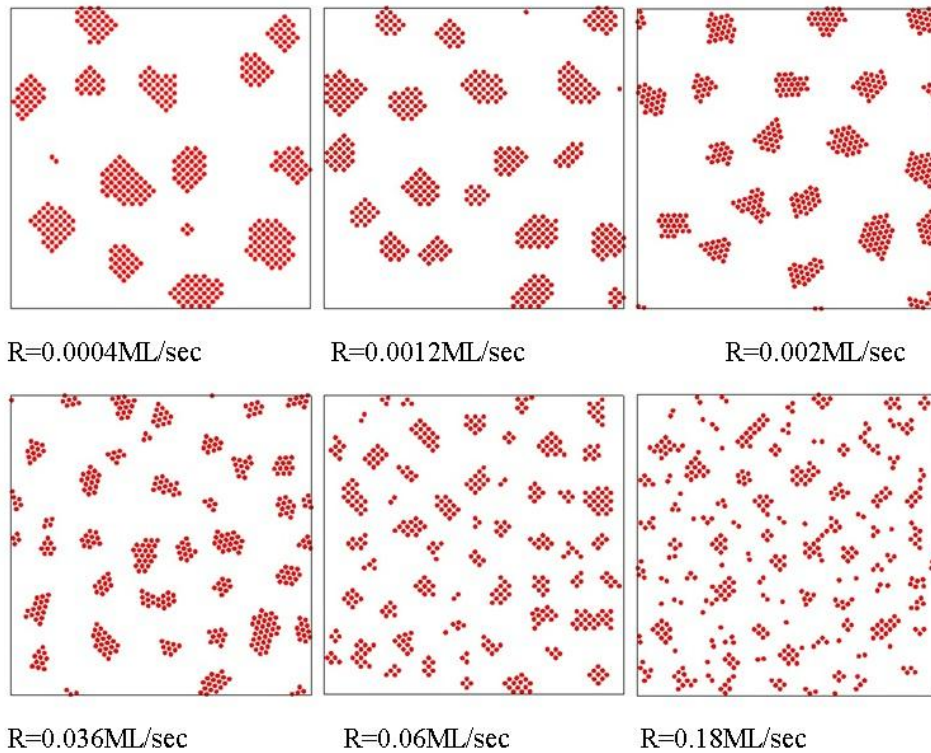


Figure 6.8. Simulation for constant coverage $\theta=0.375$ ML at various deposition rates $R=0.0025\text{ML/sec}$ to $R=0.375\text{ML/sec}$, at $T=300$ K

6.3.3 Effect of Temperature

The effect of temperature in the 2D off-lattice model is shown in Fig. 6.9. I applied a periodic substrate potential with the amplitude of 0.06 eV as a substrate binding energy for adatoms. Similar to the lattice based model, the results of the off-lattice simulation show the trends of island size increase with increase of temperature. Diffusion steps for the simulation are shown as a function of temperature in Fig. 6.10. As with the lattice-based model, this follows an Arrhenius-like behaviour.

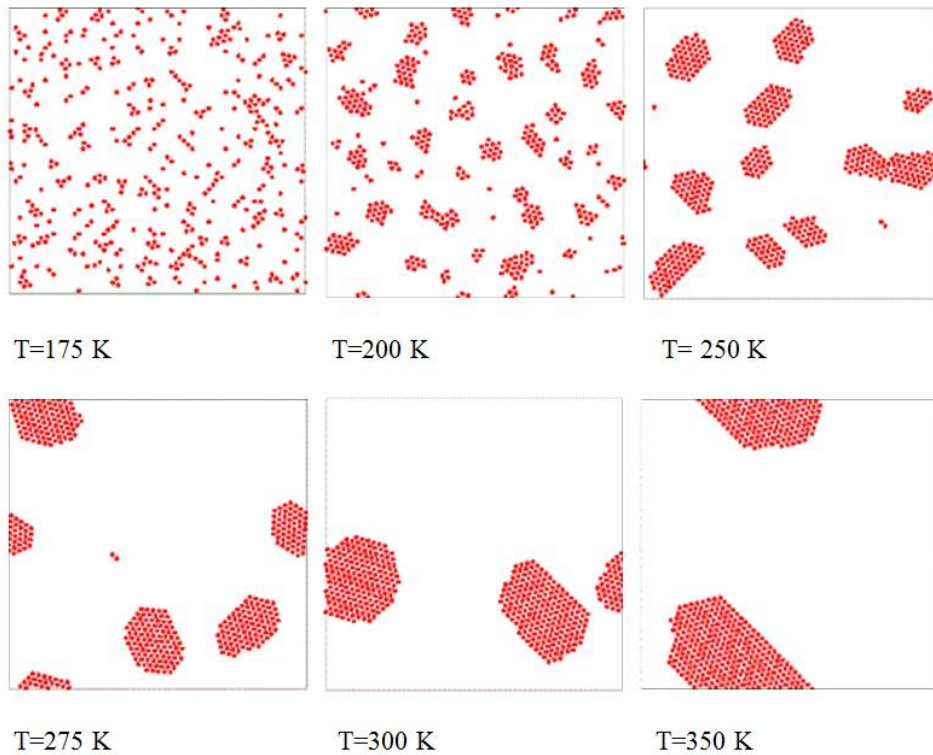


Figure 6.9. Effect of temperature on the 2D off-lattice model for $R=0.006\text{ML}/\text{sec}$ for $t=30$ sec.

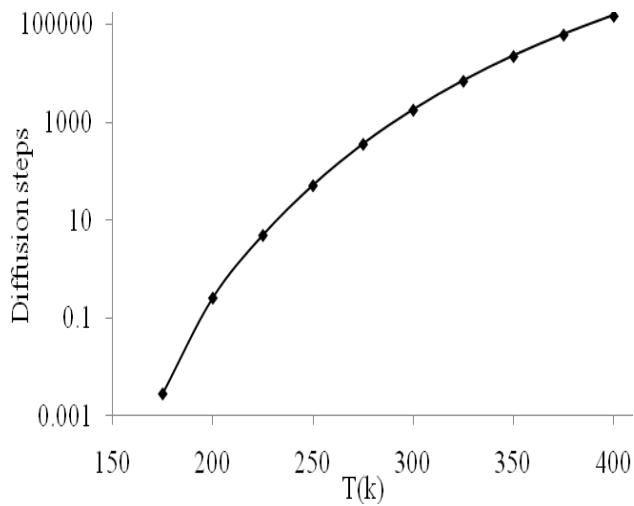


Figure 6.10. Diffusion steps as a function of temperature with $R=0.006\text{ML}/\text{sec}$.

6.4 Multilayer Off-lattice Model (3D Mode)

I have discussed in Chapter 4 that the lattice 2D model possesses certain limitations for simulating the later stage of deposition when multilayer growth plays a dominant role. The 2D off-lattice model would face similar limitations to simulate the later stage of deposition. For these reasons, the off-lattice model has been extended to a 3D mode to make it capable of simulating multilayer deposition.

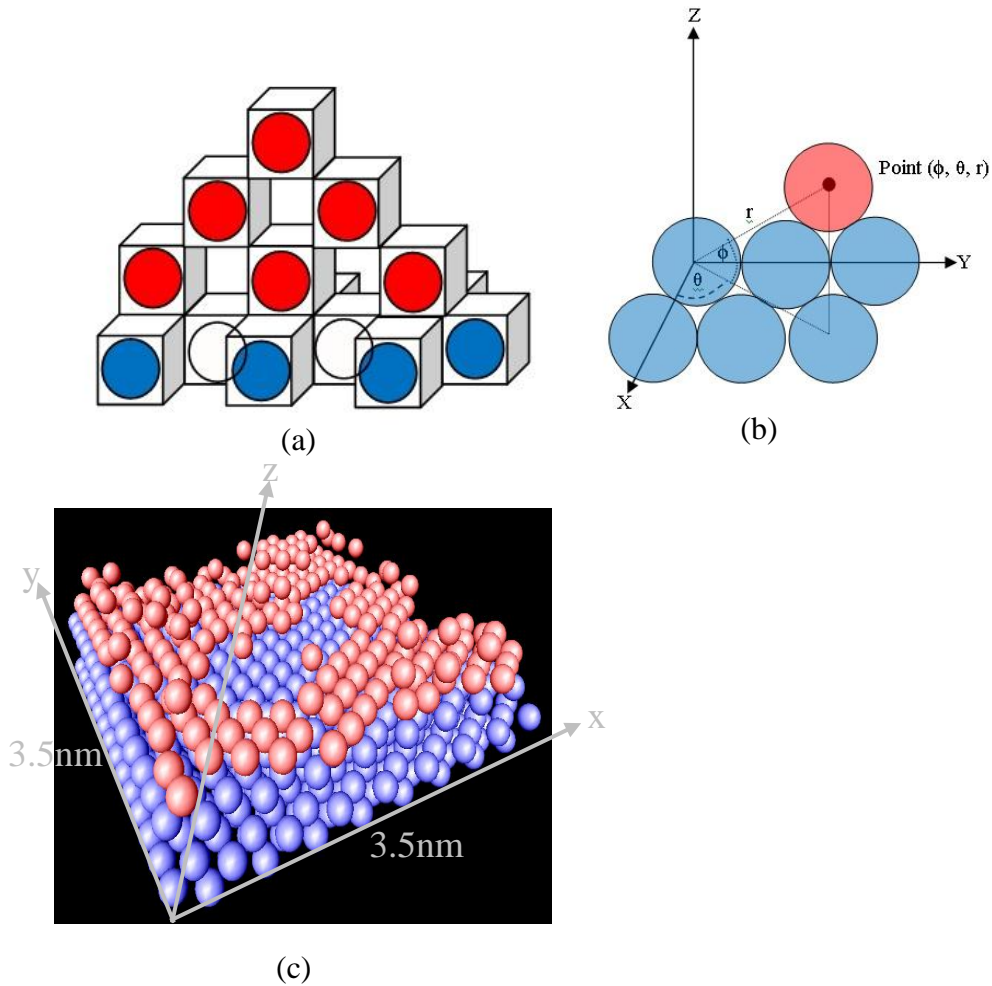


Figure 6.11. (a) Lattice based 3D model; (b) 3D off-lattice model; (c) simulated area of $3.5\text{nm} \times 3.5\text{nm}$. The substrate atoms are blue and the deposited atoms are red.

The 3D off-lattice model uses the same principles and most of the same routines as the 2D mode, but allows atoms to occupy positions in full three dimensions. The lattice based 3D model allowed growth in the vertical direction but with the specified positions only where the lattice structure permitted atoms to occupy.

Fig. 6.11 compares the 3D lattice and off-lattice structures and shows an example of multilayer off-lattice structure.

6.4.1 3D off-lattice model results

I carried out the deposition process with constant deposition rate and observed the evolution of the morphology. Simulation starts with creating the substrate (blue atoms). Then the deposition starts (red atoms) on top of the substrate. Tiny islands form on the substrate and their size keeps growing both laterally and vertically as the deposition continues.

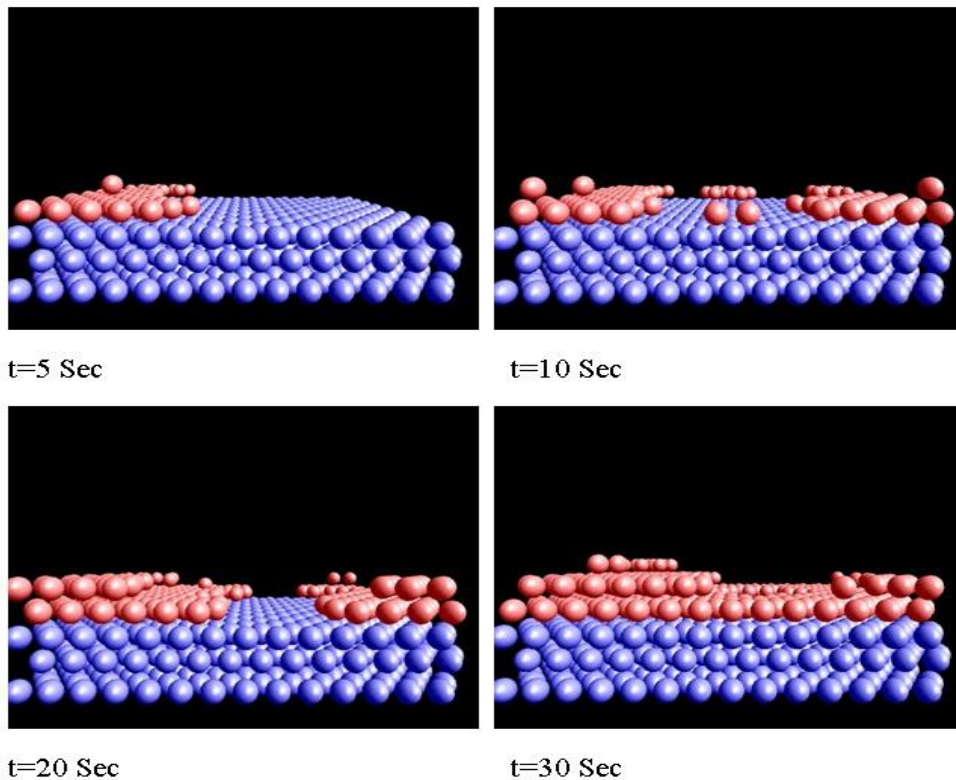


Figure 6.12. Change in surface morphology at $R=0.051$ ML/sec and $T=300$ K.

The growing 3D clusters eventually merge over the time and a thin film is formed. Similar to the case of the lattice model, multilayer islands emerge even before completing a single monolayer. Fig. 6.12 shows the change in morphologies during constant deposition.

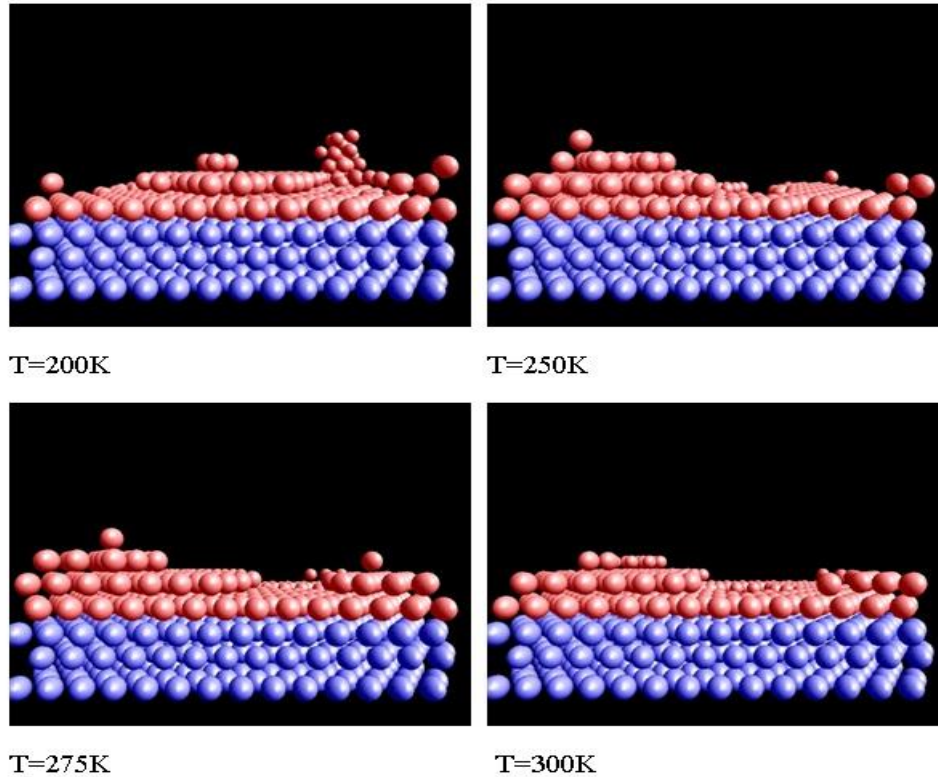


Figure 6.13. Effect of temperature on the morphology in the 3D off-lattice model with $R=0.051$ ML/sec, $t=30$ sec.

The effect of temperature on the 3D off-lattice model is shown in Fig. 6.13. It is evident that the rise in temperature causes the islands to rearrange in a more uniform layer. Similar to the 2D off-lattice mode, in temperature regimes between 250-275K more organized multilayer depositions is observed. However, beyond

300K a more efficient annealing caused flattening of the top layers resulting in a height decrease. Thus, different modes of crystal growth are clearly evident from the 3D off-lattice model results which cannot be observed in the 2D simulation.

6.5 Comparison between On-Lattice and Off-Lattice Models

I have demonstrated two different modeling methods for NC synthesis, the lattice based model and the off-lattice model. Each approach has its advantages and disadvantages. Simulations were performed for Cu deposition for similar deposition rates and times so that surface coverage remains the same for both models at the same temperature irrespective of sample size. I compare selected properties of the models in the Table 6.1.

Table 6-1. Comparison between lattice based model and off-lattice model size and time of operation with similar R , T and θ . Execution using INRF computing facility system of AMD six core Opteron 2.6GHz processor and the 64GB RAM.

Comparison		Lattice model	Off-lattice model
1	Atomic energy	Each bond 0.32eV	Min potential well 0.3eV
2	Simulation area (2D Mode): Operation time: time $t=30s$, $T=300$, $R=0.006ML/sec$, $\theta=0.20$	100nm x 100nm 1min 37 sec.	12.5nm x 12.5nm 10hr 18min 43 sec
3	Simulation area (3D Mode): Simulation time: time $t=30s$, $T=300$, $R=0.07ML/sec$, $\theta=2.14$	25nm x 25nm 1hr 53 min 39 sec	3.5nm x 3.5nm 228hr 57 min 19 sec
4	Software used	Dev C/C++, Matlab	MS Visual C++, Open GL

6.6 Summary

The off-lattice model provides more flexibility in terms of physical behaviour of atoms during NC synthesis by PVD methods. Limitations are the time and size of simulation. Lattice based models can perform with larger areas of simulation in comparatively less time. The question is not which model is right or which is wrong, but which one fits the application best. If simulation requires covering a larger area with more deposition in less time, then the lattice based model provides good simulation results. However, if more accurate morphology simulation with smaller region of operation is required, then the off-lattice based model suits best.

CHAPTER: SEVEN

7 SUMMARY AND CONCLUSIONS

In this chapter, I summarize the thesis contributions and the possible future directions of the research. As device size is decreasing and applications of nanotechnology are becoming increasingly ready for industrial implementation, focus on the understanding of nanoscale phenomena is escalating rapidly. The presented models can help both research and applications of NC synthesis by providing information about mechanisms and optimum process conditions. The lattice simulation approach presented here is flexible enough to cover both 2D and 3D models, and is complemented by the off-lattice model. Different materials and different substrates types can be considered employing the models described.

7.1 Thesis Contribution

In chapter 3, I described the 2D lattice based model, which allows the simulation of plan-view morphologies for deposited arrays of NCs. The objective was to investigate submonolayer deposition phenomena. I have considered two model structures, FCC crystalline and primitive lattice types. Major outcomes from 2D modeling are as follows:

- The impact of the variable process conditions such as the deposition rate, duration, and temperature, on the 2D morphologies of growing NCs has been studied for two different model materials: Cu and Ag. It has been

demonstrated that the impact of deposition rate on the surface morphology depends dramatically on the other process conditions, e.g. whether the duration of deposition or the amount of deposited material is kept constant. The analysis clarifies the origin of this difference, as well as provides an insight into the capabilities to control the surface morphology by varying the deposition rate and temperature for various deposition processes.

- Analysis of the numeric results in the light of the corresponding analytical scaling laws shows a reasonable agreement in the few cases when the scaling laws are applicable. These include the dependence of the average island density of deposition rate with a constant surface coverage, and the dependence of the average density of islands on the number of diffusion jumps with unchanged conditions of adatom attachment-detachment. However, many regimes relevant to practical PVD conditions require a higher flexibility. The classical scaling laws, although very useful for understanding the basic physical trends, are not always flexible enough to capture efficiently all the regimes of deposition. This emphasizes the importance of efficient direct simulations of the deposition process. Furthermore, KMC simulations also provide important information on the detailed surface morphology, which is a mandatory component required for a detailed understanding of the outcomes of deposition of NCs.

- As discussed throughout the chapter, the simulated dependencies of the surface morphologies match benchmark experimental observations from the literature. This includes the overall shape of the islands observed, the dependencies of the morphological trends on the deposition rate, and the realistic temperature of cross-over in the temperature dependence obtained numerically. These examples demonstrate that the model is a viable approach that adequately represents major trends of 2D surface morphologies during deposition. It is expected that numerical models like this can be employed to efficiently predict the outcomes of NC deposition, and rationally direct selection of optimal process conditions for nanofabrication.

As a next step, I developed a 3D lattice based model described in chapter 4, and explored the morphologies for multilayer deposition. The main contributions from this modeling technique are as follows:

- Employing the 3D model, I have investigated the capabilities to control the self-assembling surface morphology by varying the major PVD process conditions in the regimes that are directly applicable to realistic deposition experiments. Distinct from scaling laws and 2D simulations, which are efficient mostly for early deposition stages, the 3D KMC simulations have allowed handling advanced deposition processes when most of the film consists of a mounded three-dimensional landscape. This allowed, for example, a better understanding of the various ways to control surface morphology by varying the deposition rate, without constraining the analysis

by low surface coverage. The reported trends of the temperature dependence of the three-dimensional morphologies in the practically relevant temperature regimes of 225K-375K would also be useful for researchers to efficiently optimize PVD processes.

- The possibility to vary the wetting conditions in the 3D model allows predicting changes in the morphology when the binding to the substrate is varied. In this model, columnar growth of round-shaped islands is facilitated by poor wetting conditions, whereas a stronger affinity to the substrate promotes more regular pyramidal shapes. Surprisingly, the strength of binding to the substrate also seems to have an influence on the high-temperature coarsening, which is facilitated under poor wetting conditions.

In chapter 5, I applied both 2D and 3D KMC models to investigate the influence of hypothetical vacancy type defects on the observed morphologies. The summary from the defect analysis chapter is:

- I simulated three major defects types, point defects, line defects and area defects. Presence of defects affects the size and shape of the NCs simulated. Defects in 2D model showed a stronger effect on the morphology. The reason might be that my 2D model addresses submonolayer deposition which is strongly related to the substrate properties. Among the various types of the defects, point defects caused

more impact on the average size of NC produced. Presence of defects in the substrate also hinders the coarsening of crystals at higher temperature.

- Defect analysis in the 3D model showed different behavior than in the 2D one. The effect of point defects was not significant. Line defects [010] resulted in a growth of well aligned elongated islands. Change of orientation of line defects to [001] resulted in the island alignment along the direction of the defects. Conclusion can be made that textured morphologies can be generated by introducing desired defects on the substrate. However, the [011] direction line defects did not show much impact on the morphology. Presence of cluster defects affected both the crystal size and shape of NCs. Presence of defects affects the NC size more significantly in the 2D model than in the 3D model.

Besides the lattice based model, I also explored a new off-lattice type model. This model promises more flexibility than the lattice based model, as atoms are allowed to occupy any location based on energy minimum approach rather than a predefined lattice.

- Off-lattice based model validation has been carried out by exploring the effect of NC fabrication parameters on the model behavior. Modeling of the time evolution showed that surface coverage increases over the time and the islands' size also increases due to constant deposition. By controlling the deposition rate, NC size and number can

also be controlled. Temperature also plays a role in determining size, shape and number of islands.

- I also extended the off-lattice modeling to 3D structures. The time evolution of the morphology at constant deposition rate and temperature effect has been simulated. Full validation of the 3D off-lattice model was not performed in this thesis. I expect that in future, the 3D off-lattice model can be validated similarly to how the lattice models have been.

7.2 Outlook for Future Work

The modeling and simulation methods employed in this thesis have demonstrated a capability to capture a complex interplay of the multitude of various factors on which the fabrication of NCs may depend. I expect that the model and its results reported here will facilitate the PVD process design by partially replacing trial and error experiments with the numerical prediction. However, the KMC simulation method adopted is suitable for a certain range of conditions. If the simulated system size has to be much bigger, the time for simulation would increase. An integration of a continuum kinetic model with the present KMC models would increase the capability to explore larger system dimensions. Also, a multiscale parameterization of the KMC model employing MD simulations would be possible. A hybrid approach integrating multiple modeling techniques, including KMC models, is sketched in Fig. 7.1.

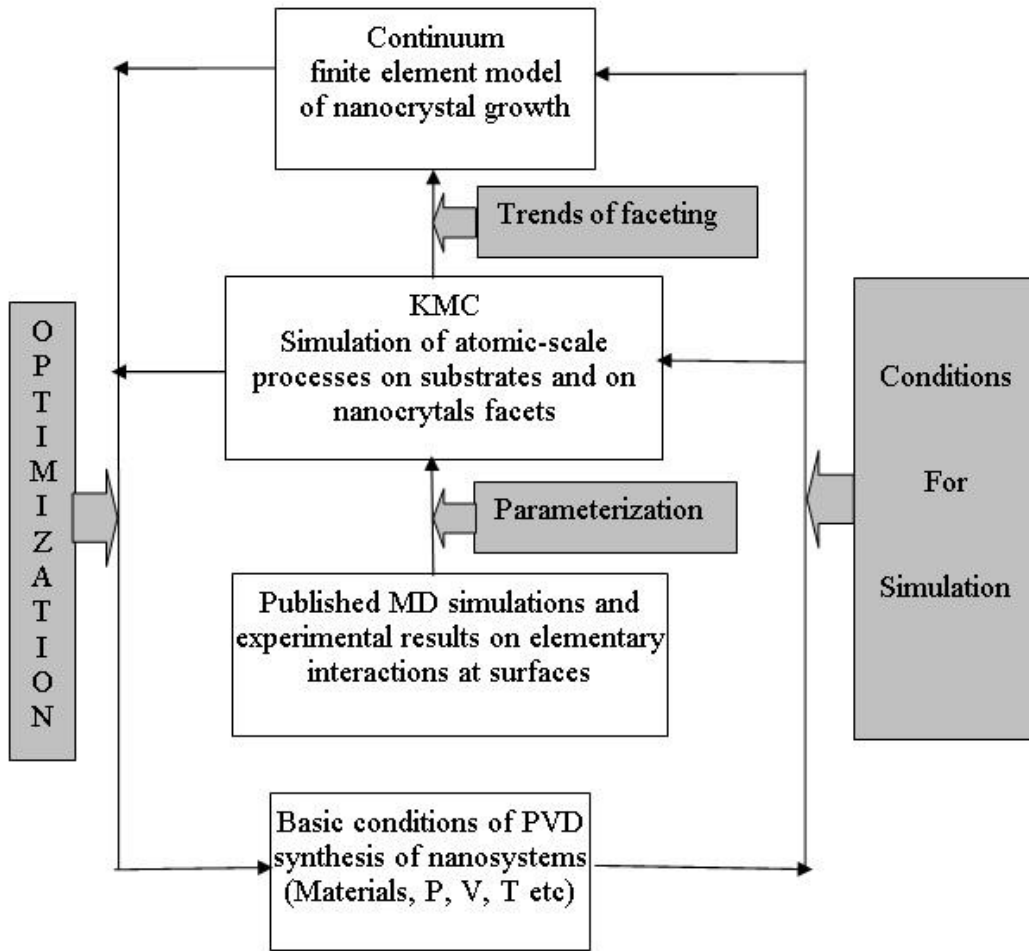


Figure 7.1. A prospective integrated multiscale simulation approach including the developed KMC models.

The ultimate goal of the modeling is to help engineers to develop useful products. Practical modeling tools can be viewed as enabling components of the fabrication process development. My model can play a significant role as a part of a bigger knowledge base for nanofabrication processes as outlined in Fig. 7.2.

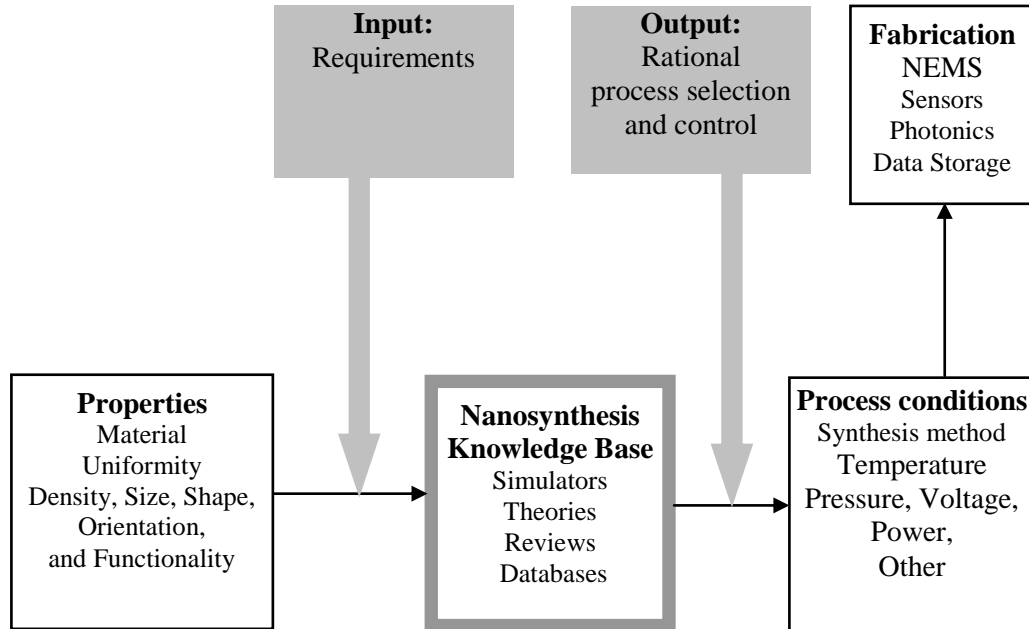


Figure 7.2. Proposed integrated system for accelerating the self-assembled nanosynthesis process development.

In conclusion, nanotechnology is seen as an important emerging technology of the present century because it promises to offer controlled fabrication with a wide range of applications. Consequently, emphasis on nanotechnology research is increasing in North America, Europe, Asia and elsewhere. Continuation of Moore's law, doubling component density in integrated circuits (ICs) in every year or two brought us to transistor size of $32nm$ in 2011, and $22nm$ technology is on the way. However, fabrication cost also doubled in every generation of process technology [134] and the latest IC fabrication facility can cost more than 5 billion dollars. The enormous rise in cost for developing product by trial and error methods compelled engineers and scientists use more and more simulation tools.

With the increase of computational power, software tools for design and understanding of nanosystems are in high demand. The modeling techniques developed here open novel opportunities to visualize and analyze the kinetic process of NC growth in atomic level detail. This will facilitate the rational optimization of the processes of PVD synthesis of NCs. Furthermore, a comprehensive multiscale software tool can be developed in future including, as a part, the KMC models described here. In conclusion, the developed simulator will contribute to the creation of a knowledge base on the self-assembled synthesis of nanostructures, which will become an important research and training resource for the industry as well as for academia.

REFERENCES

- [1] H. Iwai, "Roadmap for 22 nm and beyond," *Microelectronic Engineering*, vol. 86, pp. 1520-1528, 2009.
- [2] S. C. Tjong, *Nanocrystalline Materials: Their Synthesis-Structure-Property Relationships and Applications*. Elsevier Science Ltd, 2006.
- [3] J. R. Reimers, *Computational Methods for Large Systems: Electronic Structure Approaches for Biotechnology and Nanotechnology*. Wiley, 2011.
- [4] M. Ohring, *The Materials Science of Thin Films: Deposition and Structure*. Academic Pr, 2002.
- [5] P. Heino, H. Häkkinen and K. Kaski, "Molecular-dynamics study of copper with defects under strain," *Physical Review B*, vol. 58, pp. 641-652, 1998.
- [6] Ş. Erkoç, "Stability of gold clusters: molecular-dynamics simulations," *Physica E: Low-Dimensional Systems and Nanostructures*, vol. 8, pp. 210-218, 2000.
- [7] D. Wolf, V. Yamakov, S. R. Phillpot, A. Mukherjee and H. Gleiter, "Deformation of nanocrystalline materials by molecular-dynamics simulation: relationship to experiments?" *Acta Materialia*, vol. 53, pp. 1-40, 1/3, 2005.
- [8] C. Ratsch and J. A. Venables, "Nucleation theory and the early stages of thin film growth," *Journal of Vacuum Science & Technology A: Vacuum, Surfaces, and Films*, vol. 21, pp. S96, 2003.
- [9] P. Bruschi, P. Cagnoni and A. Nannini, "Temperature-dependent monte carlo simulations of thin metal film growth and percolation," *Physical Review B*, vol. 55, pp. 7955-7963, 1997.
- [10] L. Wang and P. Clancy, "Kinetic monte carlo simulation of the growth of polycrystalline Cu films," *Surf Sci*, vol. 473, pp. 25-38, 2001.
- [11] F. F. Abraham and G. M. White, "Computer simulation of vapor deposition on two dimensional lattices," *Journal of Applied Physics*, vol. 41, pp. 1841-1849, 1970.
- [12] H. Wei, Z. Liu and K. Yao, "Influence of microstructure of substrate surface on early stage of thin film growth," *Vacuum*, vol. 56, pp. 185-190, 2000.

- [13] L. Nurminen, A. Kuronen and K. Kaski, "Kinetic monte carlo simulation of nucleation on patterned substrates," *Physical Review B*, vol. 63, pp. 35407, 2000.
- [14] D. P. Landau, S. Pal and Y. Shim, "Monte carlo simulations of film growth," *Comput. Phys. Commun.*, vol. 121, pp. 341-346, 1999.
- [15] H. Shirakawa and H. Komiyama, "Migration-coalescence of nanoparticles during deposition of Au, Ag, Cu, and GaAs on amorphous SiO₂," *Journal of Nanoparticle Research*, vol. 1, pp. 17-30, 1999.
- [16] S. Frank, H. Wedler, R. Behm, J. Rottler, P. Maass, K. Caspersen, C. Stoldt, P. Thiel and J. Evans, "Approaching the low-temperature limit in nucleation and two-dimensional growth of fcc (100) metal films Ag/Ag (100)," *Physical Review B*, vol. 66, pp. 155435, 2002.
- [17] R. P. Feynman, "There's plenty of room at the bottom," *Eng. Sci.*, vol. 23, pp. 22-36, 1960.
- [18] K. Reichelt, "Nucleation and growth of thin films," *Vacuum*, vol. 38, pp. 1083-1099, 1988.
- [19] J. G. Amar and F. Family, "Critical cluster size: Island morphology and size distribution in submonolayer epitaxial growth," *Phys. Rev. Lett.*, vol. 74, pp. 2066-2069, 1995.
- [20] J. M. Pomeroy and J. D. Brock, "Critical nucleus phase diagram for the Cu (100) surface," *Physical Review B. Condensed Matter and Materials Physics*, vol. 73, pp. 245405.1-245405.7, 2006.
- [21] J. A. Venables, G. D. T. Spiller and M. Hanbucken, "Nucleation and growth of thin films," *Rep. Prog. Phys.*, vol. 47, pp. 399, 1984.
- [22] E. Makino, M. Uenoyama and T. Shibata, "Flash evaporation of TiNi shape memory thin film for microactuators," *Sensors and Actuators A: Physical*, vol. 71, pp. 187-192, 1998.
- [23] J. M. Merino, M. Leon, F. Rueda and R. Diaz, "Flash evaporation of chalcogenide thin films," *Thin Solid Films*, vol. 361, pp. 22-27, 2000.
- [24] M. Law, J. M. Luther, Q. Song, B. K. Hughes, C. L. Perkins and A. J. Nozik, "Structural, optical, and electrical properties of PbSe nanocrystal solids treated thermally or with simple amines," *J. Am. Chem. Soc.*, vol. 130, pp. 5974-5985, 2008.

- [25] C. E. Cross, J. C. Hemminger and R. M. Penner, "Physical vapor deposition of one-dimensional nanoparticle arrays on graphite: seeding the electrodeposition of gold nanowires," *Langmuir*, vol. 23, pp. 10372-10379, 2007.
- [26] V. G. Dubrovskii, I. P. Soshnikov, N. V. Sibirev, G. E. Cirlin and V. M. Ustinov, "Growth of GaAs nanoscale whiskers by magnetron sputtering deposition," *J. Cryst. Growth*, vol. 289, pp. 31-36, 2006.
- [27] H. Ham, G. Shen, J. H. Cho, T. J. Lee, S. H. Seo and C. J. Lee, "Vertically aligned ZnO nanowires produced by a catalyst-free thermal evaporation method and their field emission properties," *Chemical Physics Letters*, vol. 404, pp. 69-73, 2005.
- [28] J. J. Lee and D. L. Kwong, "Metal nanocrystal memory with high- κ tunneling barrier for improved data retention," *Electron Devices, IEEE Transactions on*, vol. 52, pp. 507-511, 2005.
- [29] J. H. Chen, Y. Q. Wang, W. J. Yoo, Y. C. Yeo, G. Samudra, D. S. Chan, A. Y. Du and D. L. Kwong, "Nonvolatile flash memory device using Ge nanocrystals embedded in HfAlO high- κ -tunneling and control oxides: Device fabrication and electrical performance," *Electron Devices, IEEE Transactions on*, vol. 51, pp. 1840-1848, 2004.
- [30] U. Lüders, F. Sánchez and J. Fontcuberta, "Self-organized structures in CoCr₂O₄ (001) thin films: Tunable growth from pyramidal clusters to a {111} fully faceted surface," *Physical Review B*, vol. 70, pp. 45403, 2004.
- [31] C. M. Zhang, M. C. Bartelt, J. -. Wen, C. J. Jenks, J. W. Evans and P. A. Thiel, "Submonolayer island formation and the onset of multilayer growth during Ag/Ag(100) homoepitaxy," *Surf Sci*, vol. 406, pp. 178-193, 5/31, 1998.
- [32] J. A. Stroscio, D. T. Pierce and R. A. Dragoset, "Homoepitaxial growth of iron and a real space view of reflection-high-energy-electron diffraction," *Phys. Rev. Lett.*, vol. 70, pp. 3615-3618, 1993.
- [33] O. Biham, I. Furman, H. Mehl and J. Wendelken, "Diffusion, nucleation and growth on metal surfaces," *Quantum Dots: Fundamentals, Applications, and Frontiers*, pp. 55-70, 2005.
- [34] J. K. Zuo and J. F. Wendelken, "Evolution of mound morphology in reversible homoepitaxy on Cu (100)," *Phys. Rev. Lett.*, vol. 78, pp. 2791-2794, 1997.
- [35] Y. Du, M. S. Zhang, J. Hong, Y. Shen, Q. Chen and Z. Yin, "Structural and optical properties of nanophase zinc oxide," *Appl. Phys. A*, vol. 76, pp. 171-176, 2003.

- [36] Z. L. Wang, "Zinc oxide nanostructures: growth, properties and applications," *Journal of Physics Condensed Matter*, vol. 16, pp. 829-858, 2004.
- [37] T. W. Kim, D. U. Lee and Y. S. Yoon, "Microstructural, electrical, and optical properties of SnO nanocrystalline thin films grown on InP (100) substrates for applications as gas sensor devices," *J. Appl. Phys.*, vol. 88, pp. 3759, 2000.
- [38] R. D. Schaller and V. I. Klimov, "High efficiency carrier multiplication in PbSe nanocrystals: implications for solar energy conversion," *Phys. Rev. Lett.*, vol. 92, pp. 186601, 2004.
- [39] J. M. Luther, M. Law, M. C. Beard, Q. Song, M. O. Reese, R. J. Ellingson and A. J. Nozik, "Schottky solar cells based on colloidal nanocrystal films," *Nano Letters*, vol. 8, pp. 3488-3492, 2008.
- [40] B. D. Terris and T. Thomson, "Nanofabricated and self-assembled magnetic structures as data storage media," *J. Phys. D*, vol. 38, pp. R199, 2005.
- [41] I. L. Medintz, H. T. Uyeda, E. R. Goldman and H. Mattoussi, "Quantum dot bioconjugates for imaging, labelling and sensing," *Nature Materials*, vol. 4, pp. 435-446, 2005.
- [42] C. Nützenadel, A. Züttel, D. Chartouni, G. Schmid and L. Schlapbach, "Critical size and surface effect of the hydrogen interaction of palladium clusters," *The European Physical Journal D*, vol. 8, pp. 245-250, 2000.
- [43] G. Gilmer, H. Huang and C. Roland, "Thin film deposition: fundamentals and modeling," *Computational Materials Science*, vol. 12, pp. 354, 1998.
- [44] J. A. Thornton, "Influence of apparatus geometry and deposition conditions on the structure and topography of thick sputtered coatings," *Journal of Vacuum Science and Technology*, vol. 11, pp. 666-670, 1974.
- [45] I. Kabadshow, "Available atomic scale simulation software packages," *Technische Universität Chemnitz, Studienarbeit*, pp. 1-35, 2005.
- [46] P. Roura and J. Fort, "Local thermodynamic derivation of Young's equation," *J. Colloid Interface Sci.*, vol. 272, pp. 420-429, 2004.
- [47] J. W. Matthews, D. C. Jackson and A. Chambers, "Effect of coherency strain and misfit dislocations on the mode of growth of thin films," *Thin Solid Films*, vol. 26, pp. 129-134, 1975.
- [48] D. Walton, "Nucleation of vapor deposits," *J. Chem. Phys.*, vol. 37, pp. 2182, 1962.

- [49] J. L. Robins and T. N. Rhodin, "Nucleation of metal crystals on ionic surfaces," *Surf Sci*, vol. 2, pp. 346-355, 1964.
- [50] J. A. Venables, "Nucleation and growth processes in thin film formation," *Journal of Vacuum Science & Technology B: Microelectronics and Nanometer Structures*, vol. 4, pp. 870, 1986.
- [51] J. A. Venables, "Atomic processes in crystal growth," *Surf Sci*, vol. 299-300, pp. 798-817, 1/1, 1994.
- [52] C. Ratsch, A. Zangwill, P. Šmilauer and D. D. Vvedensky, "Saturation and scaling of epitaxial island densities," *Phys. Rev. Lett.*, vol. 72, pp. 3194-3197, 1994.
- [53] H. Brune, G. S. Bales, J. Jacobsen, C. Boragno and K. Kern, "Measuring surface diffusion from nucleation island densities," *Physical Review B*, vol. 60, pp. 5991-6006, 1999.
- [54] J. E. Van Nostrand, S. J. Chey, M. A. Hasan, D. G. Cahill and J. Greene, "Surface morphology during multilayer epitaxial growth of Ge (001)," *Phys. Rev. Lett.*, vol. 74, pp. 1127-1130, 1995.
- [55] J. A. Stroschio, D. T. Pierce, M. D. Stiles, A. Zangwill and L. M. Sander, "Coarsening of unstable surface features during Fe (001) homoepitaxy," *Phys. Rev. Lett.*, vol. 75, pp. 4246-4249, 1995.
- [56] K. Thürmer, R. Koch, M. Weber and K. H. Rieder, "Dynamic evolution of pyramid structures during growth of epitaxial Fe (001) films," *Phys. Rev. Lett.*, vol. 75, pp. 1767-1770, 1995.
- [57] F. Tsui, J. Wellman, C. Uher and R. Clarke, "Morphology transition and layer-by-layer growth of Rh (111)," *Phys. Rev. Lett.*, vol. 76, pp. 3164-3167, 1996.
- [58] M. Siegert, "Coarsening dynamics of crystalline thin films," *Phys. Rev. Lett.*, vol. 81, pp. 5481-5484, 1998.
- [59] A. W. Hunt, C. Orme, D. R. M. Williams, B. G. Orr and L. M. Sander, "Instabilities in MBE growth," *EPL (Europhysics Letters)*, vol. 27, pp. 611, 1994.
- [60] W. W. Mullins and J. Appl, "Phys. 28, 333 (1957)," *J. Appl. Phys.*, vol. 30, pp. 77, 1959.
- [61] O. Biham, I. Furman, M. Karimi, G. Vidali, R. Kennett and H. Zeng, "Models for diffusion and island growth in metal monolayers," *Arxiv Preprint Cond-mat/9611095*, 1996.

- [62] S. Günther, E. Kopatzki, M. C. Bartelt, J. W. Evans and R. J. Behm, "Anisotropy in nucleation and growth of two-dimensional islands during homoepitaxy on "hex" reconstructed Au (100)," *Phys. Rev. Lett.*, vol. 73, pp. 553-556, 1994.
- [63] H. J. Ernst, F. Fabre and J. Lapujoulade, "Nucleation and diffusion of Cu adatoms on Cu (100): A helium-atom-beam scattering study," *Physical Review B*, vol. 46, pp. 1929-1932, 1992.
- [64] W. C. Elliott, P. F. Miceli, T. Tse and P. W. Stephens, "Temperature and orientation dependence of kinetic roughening during homoepitaxy: A quantitative x-ray-scattering study of Ag," *Physical Review B*, vol. 54, pp. 17938-17942, 1996.
- [65] E. Kopatzki, S. Günther, W. Nichtl-Pecher and R. Behm, "Homoepitaxial growth on Ni (100) and its modification by a preadsorbed oxygen adlayer," *Surf Sci*, vol. 284, pp. 154-166, 1993.
- [66] Y. W. Mo, J. Kleiner, M. B. Webb and M. G. Lagally, "Activation energy for surface diffusion of Si on Si (001): A scanning-tunneling-microscopy study," *Phys. Rev. Lett.*, vol. 66, pp. 1998-2001, 1991.
- [67] L. Bardotti, C. R. Stoldt, C. J. Jenks, M. C. Bartelt, J. W. Evans and P. A. Thiel, "High-resolution LEED profile analysis and diffusion barrier estimation for submonolayer homoepitaxy of Ag/Ag (100)," *Physical Review B*, vol. 57, pp. 12544-12549, 1998.
- [68] G. Costantini, F. Buatier de Mongeot, C. Boragno and U. Valbusa, "Temperature dependent reentrant smooth growth in Ag (001) homoepitaxy," *Surf Sci*, vol. 459, pp. L487-L492, 2000.
- [69] H. Huang, G. H. Gilmer and Rubia, D. De La, T., "An atomistic simulator for thin film deposition in three dimensions," *J. Appl. Phys.*, vol. 84, pp. 3636-3649, 1998.
- [70] S. Frank and P. A. Rikvold, "Kinetic monte carlo simulations of electrodeposition: Crossover from continuous to instantaneous homogeneous nucleation within Avrami's law," *Surf Sci*, vol. 600, pp. 2470-2487, 6/15, 2006.
- [71] M. Hildebrand and A. S. Mikhailov, "Mesoscopic modeling in the kinetic theory of adsorbates," *J. Phys. Chem.*, vol. 100, pp. 19089-19101, 1996.
- [72] L. J. Friedrich, S. K. Dew, M. Brett and T. Smy, "Thin film microstructure modelling through line-segment simulation," *Thin Solid Films*, vol. 266, pp. 83-88, 9/15, 1995.

- [73] H. Jeong and E. D. Williams, "Steps on surfaces: experiment and theory," *Surface Science Reports*, vol. 34, pp. 171-294, 9, 1999.
- [74] H. N. G. Wadley, X. Zhou, R. A. Johnson and M. Neurock, "Mechanisms, models and methods of vapor deposition," *Progress in Materials Science*, vol. 46, pp. 329-377, 2001.
- [75] R. E. Rudd and J. Q. Broughton, "Coarse-grained molecular dynamics: Nonlinear finite elements and finite temperature," *Physical Review B*, vol. 72, pp. 144104, 2005.
- [76] G. H. Gilmer, H. Huang, T. D. de la Rubia, J. Dalla Torre and F. Baumann, "Lattice monte carlo models of thin film deposition," *Thin Solid Films*, vol. 365, pp. 189-200, 4/17, 2000.
- [77] S. K. Dew, T. Smy and M. J. Brett, "Simulation of elevated temperature aluminum metallization using SIMBAD," *Electron Devices, IEEE Transactions on*, vol. 39, pp. 1599-1606, 1992.
- [78] D. Vick, L. J. Friedrich, S. K. Dew, M. J. Brett, K. Robbie, M. Seto and T. Smy, "Self-shadowing and surface diffusion effects in obliquely deposited thin films," *Thin Solid Films*, vol. 339, pp. 88-94, 1999.
- [79] A. L. Barabási and H. E. Stanley, *Fractal Concepts in Surface Growth*. Cambridge Univ Pr, 1995.
- [80] M. Hildebrand, A. S. Mikhailov and G. Ertl, "Nonequilibrium stationary microstructures in surface chemical reactions," *Physical Review E*, vol. 58, pp. 5483, 1998.
- [81] M. Xiling and Y. Wei, "MD simulation for nanocrystals," *Acta Mechanica Sinica*, vol. 19, pp. 485-507, 2003.
- [82] C. Oleksy, "Solid-on-solid model of overlayer-induced faceting," *Surf Sci*, vol. 549, pp. 246-254, 2/1, 2004.
- [83] R. E. Rudd and J. Q. Broughton, "Concurrent coupling of length scales in solid state systems," *Physica Status Solidi B Basic Research*, vol. 217, pp. 251-291, 2000.
- [84] T. P. Schulze and P. Smereka, "Coupling kinetic monte-carlo and continuum models with application to epitaxial growth," *Journal of Computational Physics*, vol. 189, pp. 197-211, 2003.
- [85] T. P. Schulze, "A hybrid scheme for simulating epitaxial growth," *J. Cryst. Growth*, vol. 263, pp. 605-615, 2004.

- [86] A. A. Knizhnik, A. A. Bagaturyants, I. V. Belov, B. V. Potapkin and A. A. Korokin, "An integrated kinetic monte carlo molecular dynamics approach for film growth modeling and simulation: ZrO₂ deposition on Si (1 0 0) surface," *Computational Materials Science*, vol. 24, pp. 128-132, 2002.
- [87] W. K. Liu, E. G. Karpov, S. Zhang and H. S. Park, "An introduction to computational nanomechanics and materials," *Comput. Methods Appl. Mech. Eng.*, vol. 193, pp. 1529-1578, 2004.
- [88] P. Cizek, M. R. Barnett, M. D. Nave, E. F. Rauch and R. Balasubramaniam, "Microscale and mesoscale crystallographic textures of nanocrystalline Ni-Based electrodeposits," *Metallurgical and Materials Transactions A*, pp. 1-13, 2010.
- [89] C. W. Hong and W. H. Chen, "Computational quantum chemistry on the photoelectric characteristics of semiconductor quantum dots and biological pigments," *CMES: Computer Modeling in Engineering & Sciences*, vol. 72, pp. 211-228, 2011.
- [90] H. Lim, M. G. Lee, J. H. Kim, B. L. Adams and R. H. Wagoner, "Simulation of polycrystal deformation with grain and grain boundary effects," *Int. J. Plast.*, 2011.
- [91] Y. Mishin, M. Asta and J. Li, "Atomistic modeling of interfaces and their impact on microstructure and properties," *Acta Materialia*, vol. 58, pp. 1117-1151, 2010.
- [92] J. W. Evans, P. A. Thiel and M. C. Bartelt, "Morphological evolution during epitaxial thin film growth: Formation of 2D islands and 3D mounds," *Surface Science Reports*, vol. 61, pp. 1-128, 4, 2006.
- [93] K. Kambe, "Cohesive energy of noble metals," *Physical Review*, vol. 99, pp. 419-422, 1955.
- [94] J. Uppenbrink and D. J. Wales, "Structure and energetics of model metal clusters," *J. Chem. Phys.*, vol. 96, pp. 8520, 1992.
- [95] W. Eckstein, *Computer Simulation of Ion-Solid Interactions*. Berlin: Springer-Verlag, 1991.
- [96] "The description of the SRIM code can be found at <http://www.srim.org/>," .
- [97] M. Bott, M. Hohage, M. Morgenstern, T. Michely and G. Comsa, "New approach for determination of diffusion parameters of adatoms," *Phys. Rev. Lett.*, vol. 76, pp. 1304-1307, 1996.

- [98] P. Zhang, X. Zheng, S. Wu, J. Liu and D. He, "Kinetic monte carlo simulation of Cu thin film growth," *Vacuum*, vol. 72, pp. 405-410, 2004.
- [99] M. Mixa, V. Holý, G. Springholz and G. Bauer, "Kinetic monte carlo simulation of self-organized growth of PbSe/PbEuTe quantum dot multilayers," *Physical Review B*, vol. 80, pp. 45325, 2009.
- [100] E. Pan, M. Sun, P. W. Chung and R. Zhu, "Three-dimensional kinetic monte carlo simulation of prepatterned quantum-dot island growth," *Appl. Phys. Lett.*, vol. 91, pp. 193110-193110, 2007.
- [101] S. Ryu, C. R. Weinberger, M. I. Baskes and W. Cai, "Improved modified embedded-atom method potentials for gold and silicon," *Modell Simul Mater Sci Eng*, vol. 17, pp. 075008, 2009.
- [102] M. Asta, D. Morgan, J. Hoyt, B. Sadigh, J. Althoff, D. De Fontaine and S. Foiles, "Embedded-atom-method study of structural, thermodynamic, and atomic-transport properties of liquid Ni-Al alloys," *Physical Review B*, vol. 59, pp. 14271, 1999.
- [103] H. Mehl, O. Biham, I. Furman and M. Karimi, "Models for adatom diffusion on fcc (001) metal surfaces," *Physical Review B*, vol. 60, pp. 2106, 1999.
- [104] G. M. Bhuiyan, M. Silbert and M. J. Stott, "Structure and thermodynamic properties of liquid transition metals: An embedded-atom-method approach," *Physical Review B*, vol. 53, pp. 636, 1996.
- [105] L. Wang, X. F. Han, Y. N. Zhang and X. F. Liu, "Application of modified Lennard-Jones potentials to structural and dynamical studies for liquid Al," *J. Non Cryst. Solids*, vol. 354, pp. 4970-4974, 2008.
- [106] Y. N. Zhang, L. Wang, S. Morioka and W. M. Wang, "Modified Lennard-Jones potentials for Cu and Ag based on the dense gaslike model of viscosity for liquid metals," *Physical Review B*, vol. 75, pp. 014106, 2007.
- [107] P. M. Agrawal, B. M. Rice and D. L. Thompson, "Predicting trends in rate parameters for self-diffusion on FCC metal surfaces," *Surf Sci*, vol. 515, pp. 21-35, 2002.
- [108] H. A. Van der Vegt, W. J. Huisman, P. B. Howes and E. Vlieg, "The effect of Sb on the nucleation and growth of Ag on Ag (100)," *Surf Sci*, vol. 330, pp. 101-112, 1995.

- [109] S. J. Liu, E. G. Wang, C. H. Woo and H. Huang, "Three-dimensional Schwoebel–Ehrlich barrier," *Journal of Computer-Aided Materials Design*, vol. 7, pp. 195-201, 2000.
- [110] P. C. Searson, R. Li and K. Sieradzki, "Surface diffusion in the solid-on-solid model," *Phys. Rev. Lett.*, vol. 74, pp. 1395-1398, 1995.
- [111] A. K. Bhuiyan, M. Stepanova and S. K. Dew, "Trends of nanoclusters' growth by physical vapor deposition studied by atomistic simulation." *MRS*, vol. 1177, pp. 05, 2009.
- [112] A. K. Bhuiyan, S. K. Dew and M. Stepanova, "Kinetic monte carlo simulation of metallic nanoislands grown by physical vapor deposition," *CiCP*, vol. 9, pp. 49, 2011.
- [113] A. K. Swan, Z. P. Shi, J. F. Wendelken and Z. Zhang, "Flux-dependent scaling behavior in Cu (100) submonolayer homoepitaxy," *Surf Sci*, vol. 391, pp. L1205-L1211, 1997.
- [114] T. R. Linderoth, J. J. Mortensen, K. W. Jacobsen, E. Lægsgaard, I. Stensgaard and F. Besenbacher, "Homoepitaxial growth of Pt on Pt (100)-hex: effects of strongly anisotropic diffusion and finite island sizes," *Phys. Rev. Lett.*, vol. 77, pp. 87-90, 1996.
- [115] K. Abe, Y. Harada and H. Onoda, "Study of crystal orientation in Cu film on TiN layered structures," *Journal of Vacuum Science & Technology B: Microelectronics and Nanometer Structures*, vol. 17, pp. 1464, 1999.
- [116] J. G. Allpress and J. V. Sanders, "The structure and orientation of crystals in deposits of metals on mica," *Surf Sci*, vol. 7, pp. 1-25, 1967.
- [117] Q. Liu, J. Wert and N. Hansen, "Location-dependent lattice rotation and shear strain in rolled aluminium single crystals of cube and Goss orientations," *Acta Materialia*, vol. 48, pp. 4267-4279, 2000.
- [118] J. A. Wert, "Macroscopic crystal rotation patterns in rolled aluminium single crystals," *Acta Materialia*, vol. 50, pp. 3127-3141, 2002.
- [119] L. N. Dinh, L. L. Chase, M. Balooch, W. J. Siekhaus and F. Wooten, "Optical properties of passivated Si nanocrystals and SiO_x nanostructures," *Physical Review B*, vol. 54, pp. 5029-5037, 1996.
- [120] E. Hao, R. C. Bailey, G. C. Schatz, J. T. Hupp and S. Li, "Synthesis and optical properties of "branched" gold nanocrystals," *Nano Letters*, vol. 4, pp. 327-330, 2004.

- [121] T. K. Sau and C. J. Murphy, "Room temperature, high-yield synthesis of multiple shapes of gold nanoparticles in aqueous solution," *J. Am. Chem. Soc.*, vol. 126, pp. 8648-8649, 2004.
- [122] J. J. Cole, X. Wang, R. J. Knuesel and H. O. Jacobs, "Patterned growth and transfer of ZnO micro and nanocrystals with size and location control," *Adv Mater*, vol. 20, pp. 1474-1478, 2008.
- [123] C. W. Chiu, T. W. Liao, K. Y. Tsai, F. M. Wang, Y. W. Suen and C. H. Kuan, "Fabrication method of high-quality Ge nanocrystals on patterned Si substrates by local melting point control," *Nanotechnology*, vol. 22, pp. 275604, 2011.
- [124] A. E. Henkes and R. E. Schaak, "Template-assisted synthesis of shape-controlled Rh₂P nanocrystals," *Inorg. Chem.*, vol. 47, pp. 671-677, 2008.
- [125] Y. Vasquez, A. E. Henkes, J. Chris Bauer and R. E. Schaak, "Nanocrystal conversion chemistry: A unified and materials-general strategy for the template-based synthesis of nanocrystalline solids," *Journal of Solid State Chemistry*, vol. 181, pp. 1509-1523, 2008.
- [126] J. M. Stoker and R. L. Rowley, "Molecular dynamics simulation of real fluid mutual diffusion coefficients with the Lennard Jones potential model," *J. Chem. Phys.*, vol. 91, pp. 3670, 1989.
- [127] Y. Hiwatari, H. Miyagawa and T. Odagaki, "Dynamical singularities near the liquid-glass transition: Theory and molecular dynamics study," *Solid State Ionics*, vol. 47, pp. 179-222, 1991.
- [128] S. Morioka and M. H. Sun, "Evaluation of the activation energy of viscous flow in the dense gas-like model," *J. Non Cryst. Solids*, vol. 355, pp. 287-294, 2009.
- [129] J. R. Shewchuk, *An Introduction to the Conjugate Gradient Method without the Agonizing Pain*, 1994.
- [130] J. L. Nazareth, "Conjugate gradient method," *Wiley Interdisciplinary Reviews: Computational Statistics*, vol. 1, pp. 348-353, 2009.
- [131] I. Štich, R. Car, M. Parrinello and S. Baroni, "Conjugate gradient minimization of the energy functional: A new method for electronic structure calculation," *Physical Review B*, vol. 39, pp. 4997, 1989.
- [132] H. B. Schlegel, *Geometry Optimization on Potential Energy Surfaces*. World Scientific Publishing: Singapore, 1994.

[133] V. Weber and J. Hutter, "A smooth ℓ -norm sparseness function for orbital based linear scaling total energy minimization," *J. Chem. Phys.*, vol. 128, pp. 064107, 2008.

[134] C. Brown and G. Linden, *Chips and Change: How Crisis Reshapes the Semiconductor Industry*. The MIT Press, 2009.